Forced Torsional Vibration of a Monopile for Its Extraction

A linear elastodynamics and steady-state perspective

Muhammad Abrar Aulia

Forced Torsional Vibration of a Monopile for Its Extraction

A linear elastodynamics and steady-state perspective

by

Muhammad Abrar Aulia

to obtain the degree of Master of Science
at the Delft University of Technology,
to be defended publicly on April, 2023.

Student number:	4902211	
Project duration:	April, 2022 – April, 2023	
Thesis committee:	Prof. Dr. A.V. Metrikine,	TU Delft, Chairman
	Dr. S.S. Gómez,	TU Delft, Supervisor
	Dr. S.N. Verichev,	TU Delft, Committee
	Ir. C. Kasbergen,	TU Delft, Committee
	A. Tsetas, MSc,	TU Delft, Committee
	S.C.H. van der Burg, MSc,	IQIP, Committee

TU Delft

Read, in the Name of your Lord Who created-
created humans from a clinging clot.
Read! And your Lord is the Most Generous,
Who taught by the pen-
taught humanity what they knew not.

The Qur'an, 96:1-5

Preface

This thesis is my final assignment to obtain a master's degree in Offshore and Dredging Engineering program at TU Delft. I want to thank Allah, the Creator[1], the Most Merciful[2], the Guide[3], who made this happen. The degree will tell me that little had I mastered and learning must go on. After all, I hope this text is useful for the development of the GDP shaker for whatever small contribution. It is my pleasure and pride if that is the case.

Special thanks to those who helped me to realize this work. To professor Andrei Metrikine, who opened the door for me to work on the topic that is supported by ZonMw and NWO. I wish this door would never be closed. His in-person structural dynamics class stimulated me to find the turning point of my college life, let alone his direction during graduation. To Sergio Sánchez Gómez, who shared his time, insight, and patience in discussing this work. To Stas Verichev, who shared his idea to understand the physical meaning of the problem. To Cor Kasbergen for the leverage on the finite element modelling. To Athanasios Tsetas, who pointed out a better path for tackling the finite element modelling. To Sander van der Burg, who gave perception into the practice of monopile clamping.

My endless gratitude goes to my mother and father, Badiah and professor Rofiq, who trusted me to reinvent myself in Delft. Forever grateful to my sisters, Farah and Lyla, who let me take the opportunity to study abroad. Many thanks to my love, Asmita, who is always there with the right words when I am facing difficulties. This thesis is dedicated to them.

I also appreciate the support from my friends and colleagues, who shared their time, motivation, prints, and feedback during my study including at the covid-time when everything became more difficult than ever before. Finally, I acknowledge the hand of everyone who shared their know-how about physics, mathematics, and scripting on the internet.

Muhammad Abrar Aulia
Delft, April 2023

[1] Surah An-Najm - 1-62. (n.d.). Quran.com. https://quran.com/53?startingVerse=45
[2] Surah Al-Furqan - 1-77. (n.d.). Quran.com. https://quran.com/25?startingVerse=6
[3] Surah Ad-Duhaa - 1-11. (n.d.). Quran.com. https://quran.com/ad-duhaa

Abstract

The offshore monopile decommissioning demand will become definite in the coming years. Our responsibility is to ensure the rights and duties of other legitimate uses by completely removing the ageing monopile from the seabed to continuously redeveloping offshore wind farms within the same location. The growing number of past, present, and future monopile installations opens up the challenges and opportunities to be responsible and lead the decommissioning market. With the goal of complete removal, a novel GDP technique can be the win-win solution for offshore wind operators and contractors to extract the monopiles completely from the seabed using torsional and axial vibration.

This thesis seeks to understand the torque and normal force to safely clamp a monopile during a torsional vibration so that the monopile continuously slips over the soil. Gradual soil failure along the pile-soil interface's full depth due to the monopile's torsional motion is a possible theory to explain the failure mechanism. When an upper part of the pile successfully moves relative to the soil, kinetic friction occurs until the soil resistance is larger than the shearing at one point. If more shearing is added by adding more torque, more layers below will be broken while the upper part keeps sliding due to lower friction than static friction. While the linear elastic theory of solid and thin shell bodies is used within a 3D FE modelling in Ansys to couple the soil and pile, the clamping force due to the GDP shaker is decoupled from the analysis. Failure criterion is defined outside the simulation so that the gradual soil failure is done through several simulations assuming discrete soil layers.

The FE model is constructed and verified by analytical calculation through the semi-infinite cavity-pile-soil, wave reflection, and finite cavity-pile-soil-spring-dashpot problems. Several cases of gradual soil failure are simulated and show that the torque amplitudes form a distribution. Firstly, a probabilistic sense is proposed to interpret the torque amplitude and search for the optimum depth of the soil failure. Secondly, a convergence check is made with the help of an analytical shell-spring by considering more soil elements by virtue of good correlation of the shear stress between the analytical and FE model. It eventually suggests that a convergence of the torque amplitude can be achieved, which reinforces the theory of gradual soil failure. The interpretation suggests that the current GDP shaker is one step closer for a monopile extraction test with typical monopile dimensions that correspond to $D_o = 1\,m$. A first approximation of the required torque and clamping force is then proposed to benefit the analytical model for larger diameters up to $D_o = 6\,m$.

Contents

List of Figures

List of Tables

Nomenclature

2D	Two dimensional
3D	Three dimensional
α_s	Soil adhesion coefficient $(-)$
$\bar{\epsilon}_r$	Mean of relative error $(-)$
$\bar{r}_c$	Mean of correlation coefficient $(-)$
β	Soil wavenumber $(\frac{rad}{m})$
β_d	Damped soil wavenumber $(\frac{rad}{m})$
Δl	Element size (m)
Δl_{soil}	Soil element size around the pile-soil interface (m)
$\delta()$	Dirac delta function $(-)$
δ	Angle of external friction $(°)$
γ	Soil shear strain (m/m)
$\gamma_{s,wet}$	Wet unit weight of soil $(\frac{N}{m^3})$
$\gamma_s^{'}$	Effective unit weight of soil $(\frac{N}{m^3})$
γ_w	Wet unit weight of water $(\frac{N}{m^3})$
$_o$	Ratio of soil horizontal over vertical stress $(-)$
λ	Wavelength (m)
μ	Poisson's ratio of soil $(-)$
$\mu_{ex,ss}$	External friction coefficient of steel-steel contact $(-)$
μ_{ex}	External friction coefficient $(-)$
μ_{in}	Internal friction coefficient $(-)$
ω	Angular frequency $(\frac{rad}{s})$
Φ	Phase angle (rad)
ρ	Mass density of soil $(\frac{kg}{m^3})$
ρ_p	Mass density of pile $(\frac{kg}{m^3})$
ρ_w	Mass density of water $(\frac{kg}{m^3})$
$\sigma_{\bar{\epsilon}_r}$	Standard deviation of relative error $(-)$
$\sigma_{av}^{'}$	Soil average normal effective stress $(\frac{N}{m^2})$

$\sigma_h^{'}$ Soil effective horizontal stress ($\frac{N}{m^2}$)

σ_n Normal stress ($\frac{N}{m^2}$)

σ_{r_c} Standard deviation of correlation coefficient ($-$)

σ_v Soil vertical stress ($\frac{N}{m^2}$)

$\sigma_v^{'}$ Soil effective vertical stress ($\frac{N}{m^2}$)

$\sigma_x^{'}$ Effective normal stress in x-direction ($\frac{N}{m^2}$)

σ_{zz} Normal stress in z-direction on a plane normal to z-direction ($\frac{N}{m^2}$)

$\sigma_z^{'}$ Effective normal stress in z-direction ($\frac{N}{m^2}$)

τ_{ex} Coulomb external shear stress at failure ($\frac{N}{m^2}$)

τ_{ex}^{*} Mohr-Coulomb external shear stress at failure ($\frac{N}{m^2}$)

τ_{in} Coulomb internal shear stress at failure ($\frac{N}{m^2}$)

τ_{in}^{*} Mohr-Coulomb internal shear stress at failure ($\frac{N}{m^2}$)

τ_o Amplitude of uniformly distributed fictitious force per unit longitudinal and circumferential length ($\frac{N}{m^2}$)

$\tau_{r\theta}$ Shear stress in the θ-direction on the plane normal to r ($\frac{N}{m^2}$)

τ_{xz} Shear stress in z-direction on a plane normal to x-direction ($\frac{N}{m^2}$)

θ Cylindrical coordinate in the circumferential direction (m)

$\tilde{u}_{\theta,p,1,z}$ First derivative with respect to z of pile circumferential displacement of segment 1 in the ξ domain ($\frac{Pa}{N/m}$)

$\tilde{u}_{\theta,p,1}$ Pile circumferential displacement of segment 1 in the ξ domain ($\frac{Pa}{N/m}$)

ε_{ns}^{*} Relative error in an arbitraty number of simulation ($-$)

φ Angle of internal friction ($^\circ$)

ξ Fourier domain ($2\pi f$)

ζ Damping ratio ($-$)

ζ_p Damping ratio of pile ($-$)

a Coordinate of pile-soil interface (m)

a_s Soil adhesion ($\frac{N}{m^2}$)

Ai Airy function Ai ($-$)

b Coordinate of Soil outer boundary (m)

Bi Airy function Bi ($-$)

c Soil cohesion ($\frac{N}{m^2}$)

c_2 Shear wave speed in soil ($\frac{m}{s}$)

$c_{2,p}$ Shear wave speed in pile ($\frac{m}{s}$)

C_{dp} Complex-valued coefficient of dashpot elements ($\frac{Ns}{m^3}$)

c_{dp} Coefficient of dashpot elements ($\frac{Ns}{m^3}$)

c_{dp} Coefficient of distributed dashpot ($\frac{Ns}{m^3}$)

D_o Outer diameter of pile (m)

D_p Bending stiffness of pile (Nm)

D_r Relative density ($\%$)

d_w Water depth (m)

E Soil elasticity modulus ($\frac{N}{m^2}$)

E_p Pile elasticity modulus ($\frac{N}{m^2}$)

F Force (N)

f Frequency (Hz)

f_r Body force in the radial direction (N)

F_θ Time harmonic force in the circumferential direction (N)

f_θ Body force in the circumferential direction (N)

f_o Amplitude of force in the circumferential direction (N)

f_z Body force in the longitudinal direction (N)

G Soil shear modulus ($\frac{N}{m^2}$)

g Constant gravity acceleration ($\approx\ 9.81\ \frac{m}{s^2}$)

G_p Pile shear modulus ($\frac{N}{m^2}$)

$H()$ Heaviside step function ($-$)

$H_1^{(1)}()$ First $(1)^{st}$ order Hankel function of the first $_1$ kind ($-$)

$H_{1,\tau}$ Transfer function of the shear stress ($\frac{Pa}{N/m}$)

$J_1()$ Bessel function of the first kind ($-$)

K_p Membrane stiffness of pile ($\frac{N}{m}$)

k_θ Coefficient of distributed spring ($\frac{N}{m}$)

K_{dp} Non-reflective coefficient of spring elements ($\frac{N}{m^3}$)

k_{dp} Coefficient of spring elements ($\frac{N}{m^3}$)

kPa Kilo Pascal ($10^3 \times \frac{N}{m^2}$)

kW Kilo Watts ($10^3 \times W$)

L_p Total length of pile (m)

LK_{dp} Coefficient of the non-reflective LK boundary elemets $(\frac{Ns}{m^3})$

M_p Total mass of pile (kg)

m_p Mass of pile per unit longitudinal and circumferential length $(\frac{kg}{m^2})$

n_d Damping factor $(-)$

ns Number of simulation $(number)$

P Instantaneous power (W)

P_p Embedded/penetration/driving length of pile (m)

p_p Perimeter of pile $m)$

P_θ Time harmonic uniformly distributed fictitious force per unit longitudinal and circumferential length $(\frac{N}{m^2})$

P_{ave} Average power (W)

P_x Time harmonic uniformly distributed pressure $(\frac{N}{m^2})$

r Cylindrical coordinate in the radial direction (m)

r_M Radius of Mohr circle (m)

R_p Radius of the pile mid-surface (m)

s_u Undrained shear strength of clay $(\frac{N}{m^2})$

s_{uD} Dynamic undrained shear strength of clay $(\frac{N}{m^2})$

t Time (s)

T_o Amplitude of torque with respect to the longitudinal direction (Nm)

u_o Amplitude of displacement (m)

u_r Displacement in the radial direction (m)

U_θ Amplitude of displacement in the θ-direction in the frequency domain (m)

u_θ Displacement in the circumferential direction (m)

u_z Displacement in the longitudinal direction (m)

v Velocity $(\frac{m}{s})$

$Y_1()$ Bessel function of the second kind $(-)$

z Cylindrical coordinate in the longitudinal direction (m)

z_* Cylindrical coordinate in the opposite of z (m)

A-FRF Amplitude-Frequency response function

API American Petroleum Institute

ASTM American Society for Testing and Material Standards

AVH Axial vibratory hammer

BS British Standard

CDF	Cumulative distribution function
CPT	Cone Penetration Test
EN	European Norm
FE	Finite element
FEM	Finite element method
GDP	Gentle Driving of Piles
ISO	International Standard Organization
LK	Lysmer-Kuhlemeyer
OCR	Overconsolidation ratio
ODE	Ordinary differential equation
OWF	Offshore wind farm
OWT	Offshore wind turbine
PDE	Partial differential equation
PDF	Probability distribution function
PGA	peak ground acceleration
PPV	peak particle velocity
PVE	Name of Dieseko's vibrator
RAO	Response amplitude operator
ROV	Remotely operated vehicle
SDOF	Single degree of freedom system
SPT	Response amplitude operator
T	Loading time or period
T_F	Loading rate
TC	Test case
TF	Transfer function
TRL	Technology readiness level
VLT	Vibro-lifting-tool
WFS	Wind Farm Site

1 Introduction

1.1. Challenges

Offshore wind farms (OWF) must be decommissioned and removed at the end of their operational life. International[1] and regional[2] regulations (Gourvenec, 2018; Vugts, 2016) require unused offshore installations or structures on any continental shelf or in any exclusive economic zone to be removed, with the main idea of complete removal, to ensure the safety of navigation, protection of the marine environment, and other legitimate rights and duties of the sea. In the Netherlands, wind farm owners must decommission their OWF after 40 years (Wind & water works, 2022). For this reason, the complete removal concept has to be borne in mind by whoever deals with the decommissioning of OWF.

A first generation[3] offshore wind turbine (OWT) support structure, thus the first generation OWF, is typically planned for a design lifetime of 20 to 30 years (DNVGL, 2016). Neglecting the possibility of repowering, an extended, or underachieved lifetime, thousands of OWT have to be removed between 2020 and 2050, ranging between 20 MW and 3700 MW annual capacity in the southern North Sea (Meulen et al., 2020). Along with that, the installation of OWF is growing rapidly in Europe as part of the European Union's objective of 300 GW of power from wind to achieve climate targets in 2050 (European Comission, 2021). The demands of OWT decommissioning are thus inevitable and becoming a critical issue in the region in the coming years.

In addition to the large volumes of the current and coming OWT decommissioning activities, the industry experiences are still very limited to a relatively small size of OWT, according to a few precedences. The experiences from the offshore oil and gas industry or onshore wind farms may not necessarily be adopted fully. Generally speaking, similar to an offshore installation, offshore decommissioning is site-specific and demands proper planning, not to mention the complexity of safety, environmental, technical, societal, and economic assessment. However, unlike an offshore installation, which is one of the governing factors, offshore decommissioning is often not addressed in the early engineering due to the lack of alternative options (Gourvenec, 2018). Therefore, the offshore wind industry is urged to concentrate on the OWT decommissioning agenda.

1.2. Significance of monopiles

About 80% of the total installed OWT in the North Sea is supported by monopiles, mostly in less than 40 m water depth with diameters between 2.1 m and 7 m (Negro et al., 2017). Despite the growing development of the other type of support structures, monopiles are seemingly the favourite ones for larger water depth, proved by the trends showing that the installed monopile diameters are increasing with the wind turbine size and water depth in recent years (Meijer, 2022). Besides, when discussing

[1] Geneva Convention 1958, London Dumping Convention (LDC) 1972, United Nations Convention on the Law of the Sea (UNCLOS) 1982, International Maritime Organization (IMO) Resolution A.672 1989, and London Convention Protocol (1996 Protocol)

[2] OSPAR: Convention for the Protection of the Marine Environments of the North-East Atlantic

[3] First generation wind turbines are those installed before 2016. After 2016, they are called second generation wind turbines, which is typically designed for 40 to 50 years lifetime (Meijer, 2022).

monopile decommissioning, among the preparation and post-removal, the operation stage is the main contributor to the total decommissioning cost of an OWT founded on a monopile (Milne et al., 2021; Topham et al., 2016). Therefore, the operation stage of the monopile decommissioning is of great importance to be discussed.

The operation is dictated by removing the monopile from the seabed, which is governed by the soil resistance. The soil resistance has been predicted to be as low as $15\,MN$ and as high as $210\,MN$ using standard computation of shaft resistance (Meijer, 2022; Nielsen, 2022). Large soil resistance has been the leading cause of difficulties in complete removal of a monopile. The weight and geometry of the monopile also add the complexity to the overall operation, considering their relation to the lifting process and the available transport vessel (Shafiee & Adedipe, 2022). Compared with the other OWT's components such as transition piece and tower, monopile removal is the majority of a decommissioning operation, which accounts for 77% of the total materials (Meulen et al., 2020). These bring out the significance of monopile in the decommissioning operation. Hence one should naturally prioritise how the monopile will be removed.

1.3. Today's mindset on the monopile extraction

In contrast to the base case of complete removal of monopiles, today's practices show partial removal has been preferred, such as in Thanet and Lincs OWF, by cutting the monopile a few meters below the seabed, thus leaving the remaining monopile in the seabed (Topham et al., 2016). One concluded that the required force to pull out the entire monopile is too large and time-consuming (Meulen et al., 2020). Others concluded that the penetration depth and its weight create complexity, thus being extremely risky to the offshore personnel and disturbing to the environment when deeper excavation is done for a complete removal (Topham et al., 2016). Partial removal is allowed by international regulation if the risk of the potential harmful effects on the safety of navigation, marine environment, and personnel are so high and if the technicality and the costs are not practicable (IMO, 1989). Nevertheless, the existing cutting methods carry several disadvantages relating to safety, environmental impact, and costs.

Cutting takes a relatively long time because multiple tools are used, such as dredging or jetting tools for preparation (Hinzmann et al., 2018). A diamond wire cutting, one of the common cutting tools, may be problematic due to wire breakage. The breakage is caused by loose wire or displaced grinding segments, which can be deadly for the surroundings and stop the operation (Denkena et al., 2021), leaving the monopile with an unfinished cut. The unfinished cut may also occur due to inaccurate jet cutting from the inner side of the monopile (Hinzmann et al., 2018). Therefore, extra safety measures are necessary to assure a safe tool recovery to the sea surface and back underwater to continue the operation and keep the unfinished cut pile at the position, which will consume more offshore time.

If not with the help of divers, the method typically requires a remotely operated vehicle (ROV) for monitoring (Topham et al., 2016), meaning only a special class of support vessels with diving chambers or ROV and dredgers on board can do the operation (Metrikine et al., 2021). Also, regardless of the cutting methods, due to its abrasive nature, the cutting discharges debris which will pollute the water column. The pollution is just intensified because of the discharge from the dredging equipment. Furthermore, the remaining monopile can be exposed to the seabed environment, which endangers fishers during bottom sea trawling and may become obstacles to future offshore activities (Hinzmann et al., 2018). Therefore, the cutting operation are not environmentally friendly if no mitigations are taken.

In addition to eliminating the practical problem of cutting, the complete removal can also be seen as promoting a circular economy through recycling, as one can reclaim as much as possible the steel value, which, in the long run, promotes a more sustainable development (Maio & Rem, 2015). If one would scrap the steel metal, although there is a challenge with the price volatility, recycling the monopile has been estimated to be significant. It could pay nearly 20% of the total costs of OWF decommissioning together with other recoverable components (Topham et al., 2019). Besides, one may consider exploring the possibilities for reuse of the recovered monopile for new structural elements combined with the newly-built one (Pongiglione & Calderini, 2014). Therefore, the entire monopile extraction offers both environmental and economical value-added through omitting cutting problems, recycling, and reuse, which eventually relieves the decommissioning costs.

1.4. Complete monopile extraction using vibration

The most advanced method for complete removal of monopile foundation today is the so-called vibro-lifting-tool (VLT) which combines axial vibratory extraction and upending[4]. A method with a separate stage between vibratory extraction and upending is also available on the market. Other than that, most of the methods are not commercial yet, i.e. under development. Among them are: bottom founded removal tool and axial vibratory hammer (Stapel, 2021), overpressure and vibratory pile (Hinzmann et al., 2021), hydraulic presses and floating panels (Lehn et al., 2020), hydraulic and pneumatic overpressure (Hinzmann et al., 2020), hydraulic extraction (Coronel, 2020), and vessel motion (Meijer, 2022). The mentioned techniques will not be discussed here. Instead, a new method borrowing the technology from the so-called GDP shaker[5] will be the focus of the study. The method stands on the same ground as a conventional vertical vibratory hammer. However, the GDP shaker uses torsional vibration in addition to vertical vibration.

1.4.1. Conventional vibratory hammer: axial vibratory extraction

The axial vibratory pile[6] extraction comes naturally together with its ability for installation. Hypothetically, during pile installation, the pile vibration reduces the soil friction due to repetitive relative motion between the soil particles and the pile. Due to the reduced soil friction, the pile moves downward because of gravity. During pile extraction, the pile selfweight and the reduced soil friction is opposed by a static pull from a crane. (ISO, 2002; Jonker, 1987; Warrington, 1989). The offshore wind industry has set up a swift growth of the technology since CAPE Holland (CAPE-H) installed the monopiles for the Riffgat OWF offshore Germany in 2012. The monopile was driven to a stable depth before eventually hammered with impact to the final depth with additional noise mitigation. The fast development was due to rigid restrictions on noise emission (Vugts, 2016).

In 2015, CAPE-H invented a VLT that can clamp a monopile through all stages of pile installation, including upending, lifting, and driving to the final depth in one go without the aid of a guide frame. Using a separate tool for lifting and upending will lead to a longer offshore time. In 2018, a monopile with a 6.5 m diameter and 40.5 m length weighing 330 mt was installed using a tandem of CV-320 VLT-U 640 kgm – 210 Mt from a crane barge within 15 minutes net driving time to the final depth of 24 m in sandy soil at Maasvlakte (CAPE Holland, 2020). In 2016, Dieseko Group's vibro-hammer is used to aid the extraction of four piles of 27 m length with 3.7 m diameter weighing 84 tonne within 45 minutes each using PVE 500M 500 kgm – 10.748 kN with additional lifting and upending equipment as part of the Lely OWF decommissioning program (Dieseko, 2016).

Three basic components of vibro-hammers are eccentric masses to generate vibration, suppressors with dampers to isolate energy transfer to a crane, and clamps to fix the hammer to the pile. The hammer is operated close to the natural frequency of the pile-hammer system, which is typically at 20 to 30 Hz[7] (Jonker, 1987). Given the modern hydraulic impact hammer, the basic advantages of the vibro-hammers, excluding lifting and upending capability, are: the driving is usually fast with a low level of noise, the driving mechanism can be extended for pile extraction, the cyclic stress accumulation is small which is favourable for structural fatigue, rigid connection between pile and hammer makes it simple for handling and minimise the risk of pile run, flexible for a range of diameters and applicable for tandem combination, and there is no need for guide frame during driving (CAPE Holland, 2022; Jonker, 1987).

[4] Upending is often used when discussing installation. The term upending here is actually the reverse of upending during the decommissioning, which means the monopile is upended from the vertical position, after being removed from the seabed, to its horizontal position on the decommissioning vessel.

[5] The term *shaker* will be used interchangeably with *vibratory hammer*, *vibro-hammer*, and *hammer*.

[6] The term *pile* will be used interchangeably with *monopile*. The pile is more general than the monopile, which is a single steel pipe pile system.

[7] The standard and high frequency vary from 20 to 30 Hz and 30 to 40 Hz, respectively (Holeyman et al., 2002).

1.4.2. Gentle Driving of Piles: torsional and vibratory extraction

Gentle Driving of Piles (GDP)[8] uses a high frequency[9] and small amplitude torsional vibration about the longitudinal axis of a monopile as the primary mechanism to ensure soil friction reduction together with a low frequency and low intensity axial vibration (Metrikine et al., 2021). In the case of a conventional vibrator, the vibration provides shearing at the pile-soil interface along the longitudinal direction, reducing the soil friction at the pile-soil interface. The same consequence is assumed on the torsional vibration. However, the shearing is along the pile circumference. For this reason, it is expected that by using torsional and axial vibration, the monopile penetration will be faster than the axial vibratory hammer (AVH) due to more shearing and more frequent loading, which subsequently reduce the soil friction faster.

GDP technique is intended to emit less noise and seabed disturbance than the axial vibrator because the radial expansion of the pile during the driving is small, which leads to negligible energy transmission to the surrounding water and soil. On the contrary, a significant energy transmission from the compression wave, due to Poisson's effect, induced by an AVH, propagates to the water column and ocean floor, which create noise and seabed disturbance (Metrikine et al., 2021; Tsouvalas, 2015). So, it is favourable to limit the use of vertical vibration. Only a low intensity is expected within the GDP framework when the axial vibration is employed. Less noise and seabed disturbance mean the GDP is safe for the underwater species and neighbouring structures[10].

Apart from continuous tests in the laboratory using a small shaker (Segeren, 2019), large-scale tests was accomplished in 2019 to test the performance of the GDP shaker against other techniques such as axial vibration. Different overall dynamic responses have been observed during the installation, which indicates different dynamic responses of the pile-soil system after the installation (Segeren, 2019; Tsetas et al., 2020). The performance is compared, among other things, concerning the efficiency of the driving process. A novel procedure called energy flux approach defines the efficiency according to the cumulative energy flux normalized by the energy input. The larger the ratio between the cumulative energy flux over the energy input, the more efficient is a vibrator. The approach indicates that the GDP shaker excels the AVH's efficiency. This is due to a minor impedance contrast at the pile-soil interface predominantly at the pile tip during the vibration (Gómez et al., 2022).

The GDP shaker appears to become a future win-win solution amidst other techniques to solve the problem of the OWT decommissioning attributed to the partial removal of monopile: technically feasible, safe for the environment, and acceptable costs. Therefore, extending the potency of the GDP shaker from installation to extraction of monopiles is of interest. This study stands on the ground of utilizing the GDP shaker for monopile extraction. However, the Technology Readiness Level (TRL) of the GDP shaker is still between five and six (Metrikine et al., 2021).

1.5. Problem statement

To further advance the TRL, thus the commercialization, of the GDP shaker a modification of shaker-pile connection or clamping system is needed so that the shaker can grip the monopile in an efficient manner. The clamp is fundamental to the GDP shaker so that the monopile is safely held during the vibration and extraction without slip. It can hold the monopile if the connection is rigid, which means that the displacement continuity is ensured at all time moment during the operation. On the other hand, it needs to be cost effective such that it requires a small preparation time to clamp the monopile. In fact, during the experimental campaign in 2019, the shaker used bolted connection, which requires a flange at the top of the monopile. Bolting demands more time and increases the safety risk of personnel working overboard, consequently increasing the decommissioning costs.

[8] GDP was the first GROW project supported by Dutch RVO (Netherlands Enterprise Agency) and TKI Wind op Zee. TU Delft leads the project consortium with GROW partners: Boskalis, Deltares, DOT, Eneco, Sif, TNO, ECN, Shell, IHC, SHL, and Van Oord, aiming for a win-win solution for reducing the required impact load and the noise emission during pile driving without trading-off the pile driving time and the resistance capacity, especially in welcoming the use of large diameter monopile for OWT, for which the use of impact hammer is expected to be inefficient and dangerous for aquatic life.

[9] High frequency here is justified by the fact that the GDP shaker is designed to operate above the typical operating frequency of conventional vibrators.

[10] It can be brought into a broader context than a remote offshore environment and a wind turbine foundation. Neighbouring structures can be of coastal structures such as dykes near Irene Vorrink wind farm (Adnan Durakovic, 2022)

The application of the VLT for monopile extraction, as described in the previous section, manifests the leading position of the VLT in the market. Recalling that the GDP shaker shares a similar concept with the VLT, the clamping capabilities of the VLT may naturally be set as the benchmark. These capabilities are clamping for vibratory extraction and upending. This thesis will focus to answer the former. During the vibratory extraction, two stages are distinguished, which are the motion during the vibration and the extraction. It is the motion during the vibration that will be discussed here. Moreover, only the torsional motion that will be considered. Then, a research question is formulated **How much is the required clamping force to slip a monopile from the soil using a GDP shaker?** In order to answer the question, the second research question is brought up. **How much is the required torque to slip the monopile from the soil?** To start answering the question, preliminary assumptions are introduced to bound the context.

1.6. Scope of work and approach

Various terms are used in the literature to speak of decommissioning of offshore structures, such as *removal*, *retirement*, *abandonment*, *dismantling*, *withdrawal from service*, *to make inoperative*, *planned shut-down or removal of a structure or facility from operation or usage*, *to remove or retire from active service*, *cessation of production*, *making the platform safe* (Gourvenec, 2018; Vugts, 2016), and so forth. The restriction is on the decommissioning process of a monopile of an OWT, which is defined here as the extraction of a monopile from the seabed. The other part of OWT structures, such as the rotor nacelle assembly, blades, and tower (Negro et al., 2017), are not discussed and assumed to have been removed. Boat landing, platform, and J-tubes[11] are also assumed to have been removed. These effectively leave the monopile and the transition piece[12]. The effect of the transition piece will be neglected as a first approximation. In sandy soils, scour protection is often installed near the monopile to prevent the formation of scour at the seabed surface. The effect of scour protection will also be neglected[13] due to its small thickness compared to the soil around the embedded pile.

To answer the research questions, two ways can be chosen (Tsouvalas, 2015). The first is to pull out a monopile in a set of physical experiments immediately so that primary data are obtained by measuring the response of the monopile, shaker, and soil. Immediate measurements tend to be expensive and time-consuming. They are aggravated by the nature of the parametrization of experiments. Parameterization is vital to get a general idea of the physical phenomena of the system. The second is to create reasonable three-dimensional models in a computer so that computer experiments are simulated to mimic real-world scenarios. Simulation measurements tend to ease parametric study and are less time-consuming, thus leads to cost-effectiveness. The simulation approach, to model a monopile extraction is thus chosen in this thesis. Three-dimensional finite element method (3D FEM) in ANSYS Mechanical 2022 R2, using two main toolboxes: Harmonic Response and Static Structural, will be used in this case.

When using 3D FEM simulation to model soil, one will face a problem of defining its geometry. Also, one needs to verify and validate the result to be confident of the simulation results (Oñate, 2009; Wellens, 2021). To address the problem of soil geometrical modeling and verification, an analytical model will be developed. This is because a relevant[14] and validated 3D analytical solution for torsional problem is not yet available (Dong Guo & Randolph, 1996; Georgiadis & Saflekou, 1990; Karasudhi et al., 1984; Li et al., 2021; Luco, 1976; Nghiem & Chang, 2019; Novak & Sachs, 1973; Reissner & Sagoci, 1944; Veletsos & Dotson, 1987; Wang et al., 2008; Wu et al., 2016). Therefore, this study will assume a simplified 2D semi-infinite torsional problem where analytical solution can be obtained.

[11] Boat landing enables access of maintenance crew from a vessel to the platform (Male, 2021; Schachner, 2004).

[12] Transition piece has been one of the fundamental parts of OWT, which ensures the connectivity between the support structure and the tower. Several types of transition piece connections exist, such as grout, bolted, slip-joint, integrated, and wedge connections (Meijer, 2022). The type of connection adds the geometrical complexity, affecting the local stiffness and the mass around the connection.

[13] A scour protection can increase the lateral capacity of a pile in loose and dense sands, which is associated with the densification of sand and the increase of effective stress around the pile (Askarinejad et al., 2022). The increase of effective stress should also contribute to the shearing resistance in the axial and circumferential direction.

[14] Relevant here is defined as the one that considers vibrator-pile-soil system, that corresponds to offshore monopile dimensions, as a shell-solid that considers the soil as an infinite domain (*e.g.* both in the r and z-direction by assuming a cylindrical coordinate system) within dynamic analysis.

This analytical solution is thus assumed as the exact solution. A 2D FE model with a close proximity will stand on the exact solution, so that the 2D FE solution is verified. From this point onward, the 2D FE model is constructed progressively, on the ground of the exact solution, until eventually finding the solution to the 3D FE model on which the best way to evaluate its correctness is by validation through laboratory or field experiments.

Three admissible motions, in the axial direction, during vibratory pile installation have been suggested, which can be the pile motion as a rigid body at the time of penetration due to gravity at a frequency lower than the vibrator frequency, the pile motion as a continuous or flexible body at the vibrator frequency, and the pile motion as both rigid and flexible body at the frequency higher than the vibrator frequency (Tsetas et al., 2022). In the case of extraction, a static pull-out is the one that makes the pile moves as a rigid body. Despite the same three motions may not appear in the torsional direction, a similar notion can be referred to one of those. It is the pile motion as a flexible body at the frequency of the vibrator frequency that is considered in this study. The static pull-out force is not considered.

Finally, a frequency of $80\,Hz$ will be the main focus of this study by considering the GDP shaker's frequency during the experimental campaign in 2019, which is around three times higher than its axial counterpart that is operated at $23\,Hz$ (Gómez et al., 2022). The choice of high frequency is associated with its short wavelengths in the soil so that the soil shearing resistance is mobilized locally around the pile shaft and small impact to the post-installation lateral response (Tsetas et al., 2023). For the study of monopile extraction, other frequencies can be more favorable, for example due to less required power or to avoid resonance. When the model is proven to be reliable, other frequency input should not be a problem. Secondly, using the same frequency and other similar system parameters with the experimental campaign may give an insight into whether the same GDP shaker can be directly extended for a monopile extraction test.

1.7. Outline

This thesis comprises eight chapters in which Chapter 1 to 4 are essentially literature research. Chapter 1 covers the problem background, definition, and the choice of approach. The fundamental assumptions on the material, geometrical, and overall pile-soil system are introduced in Chapter 2 and 3. While Chapter 4 investigates how to read the results in Ansys, Chapter 5 presents the analytical model to build the geometrical model of soil and verify the FE model. Chapter 6 evaluates the plane strain model as the starting point to model the complete system. Chapter 7 explains the 3D FE modeling and discuss the results. It concludes the answer to the research question and followed by an initiation of finding the optimum depth of soil failure. If the chapter is not clear immediately, the conclusions in Chapter 8 should be sufficient to back up. Conclusions are then wrapped up by recommendations for further research.

2

Idealized monopile

2.1. Environment during a monopile decommissioning

Offshore environment is often referred to the atmosphere, ocean, and seabed condition. They embody multiple physical phenomena such as winds, water depth, tides, waves, currents, air and sea temperature, snow and ice, and seabed condition (Vugts, 2013). In what follows, only the water depth and the seabed is considered. Usually, during installation, thus the decommissioning, engineers look for the time window where the metocean condition[1] is reasonably calm[2], which allow for a safe offshore operation using a specific vessel and its equipments. Hence, it can be assumed that during a monopile extraction, the effect of the metocean condition on the monopile is negligible.

An example of an OWT decommissioning is shown in Figure 2.1 and Figure 2.2. Figure 2.1 shows a reverse installation for the RNA and the tower part and Figure 2.2 captures a moment when a vibratory hammer is being used to aid a monopile extraction. The latter is the focus of this study while the former is not. The dashed rectangle in Figure 2.2.b is the battery limit of this study. As Section 1.6 defines to what extent the monopile will be considered, Figure 2.2 clarifies the assumption that it is sufficient to examine only the monopile up to a certain height above the sea surface. To start working out a specific decommissioning problem, a general definition of relevant material and geometrical properties of the monopile as well as the soil need to be established.

[1] An abbreviation of meteorological and oceanographic.

[2] The weather must be favourable for the foreseeable future before sailing to the offshore site is made. During this period, a specific vessel must work within the limit of its motion response due to excitation from winds, waves, and currents (Schreier, 2021; Vugts, 2016).

(a) Dismantling of an OWT's RNA (b) Dismantling of an OWT's tower

Figure 2.1: Dismantling of OWT's RNA and tower in Lely OWF (Bonsink, 2018)

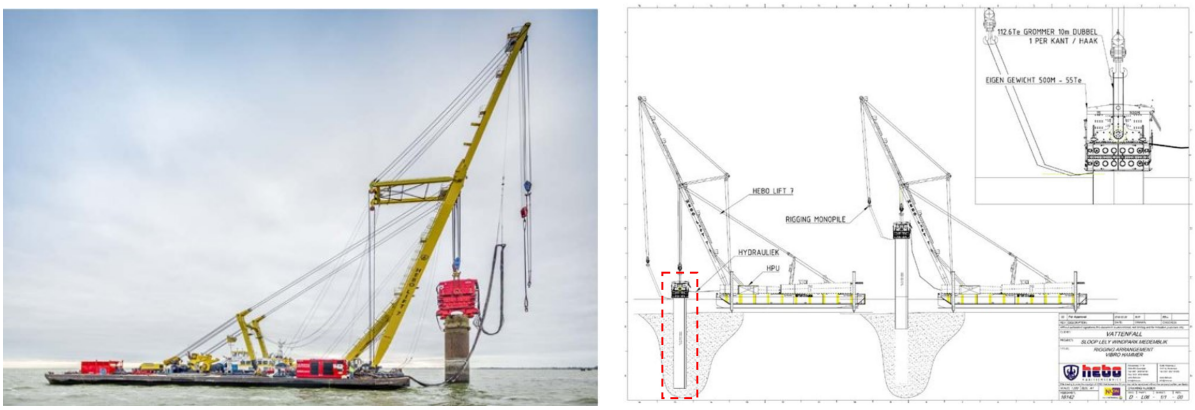

(a) Dismantling of a monopile (b) Engineering drawing of a monopile dismantling

Figure 2.2: Dismantling of a monopile in Lely OWF (Bonsink, 2018)

2.2. Material and geometrical properties of the monopile

Hereafter, it will be assumed that the monopile in this study is made of structural steel S355, as per EN10025-1, which has a minimum yield strength of $355\,MPa$ and an ultimate tensile strength between $470\,MPa$ and $630\,MPa$ (CEN, 2004b; Igwemezie et al., 2018). European structural steels, thus the monopiles, are typically standardized through Eurocode 1, which have mass density $\rho_p = 7850\,kg/m^3$ and through Eurocode 3, which have modulus elasticity $E_p = 210\,GPa$, Poisson's ratio $\nu_p = 0.3$. The corresponding shear modulus is approximately $G_p = E_p/\left(2(1+\nu_p)\right) = 81\,GPa$ (CEN, 2002, 2004c).

Next to the the material properties is the geometries. Recent studies have gathered data of the installed monopiles in Europe (Meijer, 2022; Negro et al., 2017). This data are adopted and analyzed in a simplified manner in terms of dimensionless ratios with respect to the monopile's diameter. This step will be advantageous for preliminary design when smaller diameter are desired, but still having its relevance with the existing data. The outer diameter $D_{o,n}$, water depth $d_{w,n}$, total length $L_{p,n}$[3], embedded/penetration/driving length $P_{p,n}$, and total mass $M_{p,n}$, are assumed as the primary input, where $n = 1, 2$. Table 2.1 summarizes the average of the ratio of the water depth over the outer diameter $d_{w,n}/D_{o,n}$, the total length over the outer diameter $L_{p,n}/D_{o,n}$, the penetration depth over the outer diameter $P_{p,n}/D_{o,n}$, and the outer diameter over the wall thickness $D_{o,n}/wt_n$.

All ratios, except $D_{o,n}/wt_n$, are first computed from the collected data and then averaged, without a weighing due to the number of foundations. The wall thickness, thus $D_{o,n}/wt_n$, is obtained by

$$\begin{aligned} M_{p,n} &= \frac{\pi}{4}\left(D_{o,n}^2 - \left(D_{o,n} - 2wt_n\right)^2\right) L_{p,n}\,\rho_p \\ wt_n &= \frac{1}{2}\left(D_{o,n} - \sqrt{D_{o,n}^2 - M_{p,n}\frac{4}{\pi\,L_{p,n}\,\rho_p}}\right) \end{aligned} \tag{2.1}$$

where $M_{p,1} = 213.28\,D_{o,1} - 629.7$, and $M_{p,2} = 200.72\,D_{o,2} - 548.73$ following the linear regressions shown in Figure 2.3.a.

Data	$d_{w,n}/D_{o,n}$	$L_{p,n}/D_{o,n}$	$P_{p,n}/D_{o,n}$	$D_{o,n}/wt_n$
$Data1$ (Meijer, 2022)	4.5	10.5	6.0	100
$Data2$ (Negro et al., 2017)	4.0	10.5	7.0	99

Table 2.1: The assumed parameters for establishing the monopile's geometries

It is observed from Table 2.1 that each data agrees to each other in terms of average ratios. A $D_{o,n}$ versus $M_{p,n}$ plot in Figure 2.3.a also shows an agreement in terms of their linear regression. For these

[3]The total length will be assumed to include the height of the air gap above the elevation of the sea surface z_w (see Figure 7.18).

two reasons and since $Data1$ refers to more OWF than $Data2$, $Data1$ is chosen. Having known the relevant geometrical ratios from $Data1$, a synthetic D_o, thus d_w, L_p, and P_p are generated using the known ratios.

An additional step is shown, to reason the use of linear regression, by plotting D_o versus D_o/wt_n and D_o/wt_{API} in Figure 2.3.b, where wt_{API} is the wall thickness based on the API's formula that is commonly used in studies related to monopiles. Figure 2.3.b shows that D_o/wt seems to level off around 90 when using wt_{API}[4]. Instead, according to $Data1$ and $Data2$, D_o/wt climbs with the diameter[5]. Larger D_o/wt means the monopile's cross-section becomes more slender, which in the next section becomes one of the rationale on deciding its structural idealization. Large diameter and slenderness of a monopile introduce the significance of shell model rather than classical rod model (Tsetas et al., 2021).

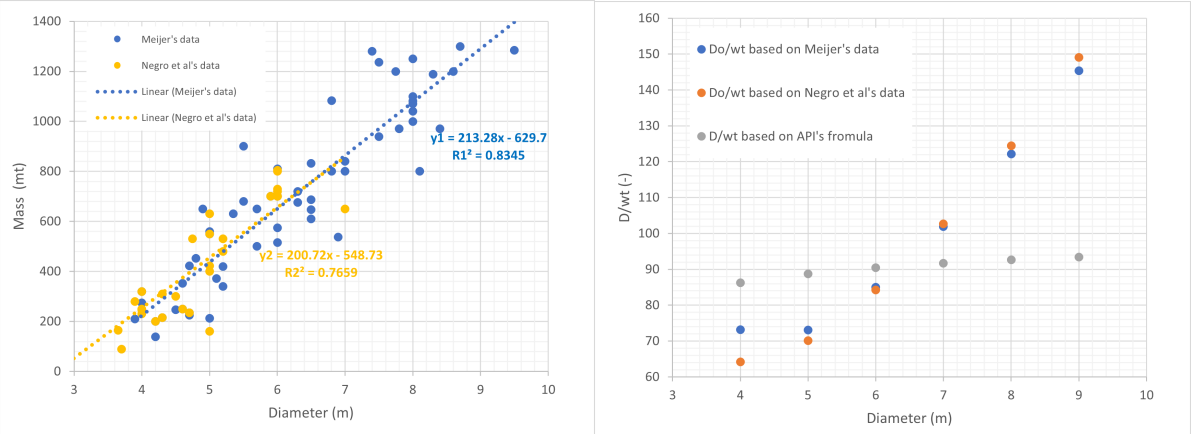

(a) Diameter-weight relationship

(b) Diameter-diameter over wall thickness relationship

Figure 2.3: Analyzed data of installed monopiles in Europe

2.3. Monopile as a homogeneous, isotropic, linear elastic shell

Due to the second nature of steel production, monopile can be assumed as a homogeneous and isotropic material as far as micro-structure is not concerned. It is justified by the fact that the steel for producing the monopiles are standardized as described in Section 2.2. It will be assumed that the resultant stresses in the monopile, during the soil failure, will be much lower than its yield strength. It will also be assumed that the monopile will be stable during the torsional vibration such that no local buckling occurs due to large D/wt. These two statements are subject for further research, since it is possible that yielding around an inflection point emerges when the embedded length of the monopile is deep enough to allow a fixation, from which the shear stress near the fixation will be maximum and only increase if the torque is increased until the monopile yields. The emergence of an inflection point can be deducted from the existing knowledge regarding bending moment in the pile subjected to lateral loading (Vugts, 2016).

According to Love-Timoshenko's thin shell theory, the force equilibrium in a thin shell happens at the middle surface so that the two-dimensional model represents a three-dimensional structure. Love assumes for small displacements of thin shells (Leissa, 1973), which in the case of circular cylindrical shell that is used in this study: 1. the ratio of shell thickness over the radius the pile and over the length of the pile is small, 2. only the first order quantities of the strain and displacement is considered due to its significance compared with their higher order ones, 3. the transverse normal stress is neglected because it is dominated by the normal stresses in the circumferential and longitudinal direction, and 4. A straight line normal to the mid-surface remains straight, normal, and not elongated after deformation due to Kirchhoff's hypothesis.

[4]The API's formula for minimum wall thickness $wt_{API} = 6.35 + D_o/100$, where wt_{API} and D_o are in mm, are designated for a range of pile diameter between $610\,mm$ and $3048\,mm$.

[5]It has been studied that D_o/wt for offshore wind monopiles can be as high as 160 (Liu, 2021).

Membrane and bending stiffness are the main restoring force of a thin shell, which under the Love-Timoshenko's thin shell theory (Timoshenko & Woinowsky-Krieger, 1959), for an axisymmetric circular cylindrical shell (Tsetas et al., 2021) reads

$$\begin{aligned} K_p \frac{\partial^2 u_z}{\partial z^2} - K_p \frac{\nu_p}{R_p} \frac{\partial u_r}{\partial z} &= \rho_p \, wt \frac{\partial^2 u_z}{\partial t^2} \\ K_p \frac{(1-\nu_p)}{2} \frac{\partial^2 u_\theta}{\partial z^2} &= \rho_p \, wt \frac{\partial^2 u_\theta}{\partial t^2} \\ -K_p \frac{\nu_p}{R_p} \frac{\partial u_z}{\partial z} - K_p \frac{1}{R_p^2} u_r - D_p \frac{\partial^4 u_r}{\partial z^4} &= \rho_p \, wt \frac{\partial^2 u_r}{\partial t^2} \end{aligned} \tag{2.2}$$

where R_p is the radius of the pile mid-surface, $K_p = E_p \, wt / \left(1 - \nu_p^2\right)$ is the membrane stiffness, and $D_p = E_p \, wt^3 / \left(12 \left(1 - \nu_p^2\right)\right)$ is the bending stiffness (Soedel, 2004). For a purely torsional vibration, only the second of (2.2) is of importance. To the contrary, the first and third of (2.2) will govern the equilibrium due to gravity to determine the initial state of stress. Note that the latter assumes no inertia effect from the pile (*i.e.* $\partial^2 u_z / \partial t^2 = 0$ and $\partial^2 u_r / \partial t^2 = 0$) and the first of (2.2) must include $-\rho_p wtg$ to account for the constant gravitational acceleration g. (2.2) is written to show the significance of the membrane and bending stiffness to avoid incorrect modeling for the FE analysis later on.

3

Soil mechanics framework: idealization and failure criterion

3.1. Soil material properties

3.1.1. Class, saturated soil, unit weight, density, and effective stress

The classification of soil differs from one and the other standards such as in ISO[1], BS[2], and ASTM[3]. Similarly to the Unified Classification System, they classify soil based on particle-size distribution and plasticity. A major difference between the standards is the grain-size bounds and the extent to which plasticity is considered. According to the grain size, they are classified into coarse-grained and fine-grained soil. Coarse-grained soils are commonly grouped into gravels and sands. The soil plasticity groups fine-grained soils into silts and clays based on the Atterberg limit test (Fugro et al., 2016). However, often they are grouped into non-cohesive soils and cohesive soils due to their practicality in civil and mechanical engineering, especially when describing their failure mechanism (Miedema, 2014; Vugts, 2016). Non-cohesive soils range from gravels to silts, which will be further defined as sands. Therefore, it leaves clays as cohesive soils.

Soil is a porous material that either water or air fills the pores between the soil grains. As far as offshore soil is considered, it is reasonable to assume that it is filled only with seawater. Therefore, it is fully saturated. Consequently, due to Archimedes' law, the soil submerged unit weight $\gamma_s^{'}$, also called the soil effective unit weight, is relevant here and defined as (Vugts, 2016)

$$\gamma_s^{'} = \gamma_{s,wet} - \gamma_w \tag{3.1}$$

where $\gamma_{s,wet}$ is the wet unit weight of soil, γ_w is the unit weight of water, and the unit weight is, in general, the density of soil ρ or water ρ_w multiplied by the gravitational constant g. Because of the presence of pore water, the total weight of the soil is distributed in both the soil grains and pores. Only the stress in the soil, or the effective stress, influences the soil shearing resistance. Soil vertical effective stress at one point below the seafloor due to its self-weight can be computed as (Terzaghi, 1943)

$$\sigma_v^{'} = \gamma_{s,wet}\, z - \gamma_w\, z \tag{3.2}$$

where z is the height of the soil layer above a particular point.

3.1.2. Ground types

A primary interest in discussing soil properties for monopile extraction is its failure parameters. The failure parameters are the shear modulus, Poisson's ratio, angle of friction for sands, and cohesion for

[1] International Standard Organization 14688-1:2002 (Geotechnical Investigation and Testing - Identification and Classification of Soil: Identification and Description) and International Standard Organization 14688-2:2004 (Principles for a Classification)
[2] British Standard 5930:1999 on Description of soils
[3] American Society for Testing and Materials Standards D 2487-11 and D 2488-09a

clays (Bowles, 1997)[4]. The measure of relative density defines whether cohesionless soil is very loose, loose, medium dense, dense, or very dense, which eventually defines its friction angle. In cohesive soils, they are classified as whether the profile is very soft, soft, firm, stiff, very stiff, hard, or very hard clays according to its undrained cohesive shear strength (Fugro et al., 2016). A concise soil profiling can be of ground types in Eurocode 8[5] (CEN, 2004a), which will be referred to hereafter.

Ground type	Description of stratigraphic profile	$c_{2,30}(m/s)$	$s_u(kPa)$
A	*Rock or other rock-like* geological formation, including at most 5 m of weaker material at the surface	> 800	$-$
B	Deposits of *very dense sand*, *gravel*, or *very stiff clay*, at least several tens of metres in thickness, characterised by a gradual increase of mechanical properties with depth	$360 - 800$	> 250
C	Deep deposits of *dense* or *medium-dense sand*, *gravel* or *stiff clay* with thickness from several tens to many hundreds of metres	$180 - 360$	$70 - 250$
D	Deposits of *loose* to *medium cohesionless soil* (with or without some soft cohesive layers), or of predominantly *soft-to-firm cohesive soil*	< 180	< 70
S1	Deposits consisting, or containing a layer at least $10\,m$ thick of *soft clays/silts* with a high plasticity index ($PI > 40$) and high water content	< 100 (indicative)	$10 - 20$

Table 3.1: Ground type

where $c_{2,30}$ is the average shear wave velocity of the top $30\,m$ soil layer and s_u is the undrained shear strength of soil. The link between the description of non-cohesive soil and its internal friction angle is shown in Table 3.2 (Fugro et al., 2016; Vugts, 2016)

Description of non-cohesive soil	Relative density D_r (%)	Angle of internal friction φ (°)
Very dense	$85 - 100$	> 45
Dense	$65 - 85$	$40 - 45$
Medium dense	$35 - 65$	$35 - 40$
Loose	$15 - 35$	$30 - 35$
Very loose	< 15	< 30

Table 3.2: Compactness of sands in terms of D_r and φ

3.1.3. Soil drainage and consolidation

When soil is loaded, the load is first resisted by the pore water and then transferred to the soil grains. The pressure gradient created by the load makes the pore water flows to the point with the lower pressure. If the soil is permeable enough, the pore water flows quickly, quicker or at about the same time as the loading rate. This loading situation is called a drained condition. On the contrary, in low permeable soil, the pore water can not escape as quickly as the rate of loading, and the pore water pressure will increase. This situation is called an undrained condition. The undrained condition is unstable and temporary. The excess pore water will eventually drain away, and the soil will stabilize. This capability of the soil to adapt is called consolidation (Vugts, 2016). Due to its low permeability, clay is often assumed to behave in an undrained manner.

The consolidation process can take years or even age for low-permeable soil such as clays. Due to this duration, soil can be normally-, over-, and under-consolidated. It is over-consolidated when the pre-consolidation pressure exceeds the current overburden pressure. In other words, the over-consolidation ratio is larger than unity $OCR > 1$. It is normally consolidated when they are equal $OCR = 1$. Else, it is under-consolidated $OCR < 1$. Due to its prominent effect in clays, the state of

[4]Bowles originally used term strength parameters. Failure here is used to avoid getting lost in discussing the shear strength and friction.

[5]Eurocode 8 must be consulted for complete list of ground types.

consolidation is often associated with clays only. Most offshore foundations are installed on normally- and over-consolidated. In the North Sea, over-consolidation is due to historical melting ice. In what follows, only overconsolidated clays will be considered for this type of soil, which is justified by its larger influence on the shear strength (Vugts, 2016). The appearance of overconsolidated clays in the North Sea is also justified by other works (Bond et al., 1997; Gourvenec & Randolph, 2011).

3.1.4. Horizontal stress

The effective vertical stress induces effective horizontal stress $\sigma_h^{'}$, which is usually not the same. It can be attributed to the nature of the soil mass and its geological history (Terzaghi, 1943). The in situ effective vertical stress $\sigma_v^{'}$ may be calculated with some accuracy, but the in situ effective horizontal stress $\sigma_h^{'}$ is generally unknown. The ratio between the vertical and horizontal (effective) stress is a function of internal friction angle φ and called the coefficient of earth pressure at rest $K_o = \sigma_h^{'}/\sigma_v^{'}$ (Fugro et al., 2016). Different formulations have been proposed due to the effect of the state of stress and consolidation.

Due to its reliability against experiments in normally-consolidated soils, the K_o formulation by Jaky (Bowles, 1997; Mesri & Hayat, 1993; Vugts, 2016) is often referred

$$K_o = 1 - \sin(\varphi) \tag{3.3}$$

For over-consolidated clays, a higher K_o is expected through Mayne and Kulhawy's suggestion

$$K_o = (1 - \sin(\varphi))OCR^{\sin(\varphi)} \tag{3.4}$$

In sands,

$$K_o = 0.4\sqrt{OCR} \tag{3.5}$$

In fact, laboratory studies cannot fully capture in situ behavior such as K_o, especially if ageing and cyclic loading are taking place. In situ K_o is limited between $K_o = 0.5$ and $K_o = 1.5$. At large depth, $K_o < 1$ is assumed in many situations. In practice, $K_o = 1$ should be the limit for large depth as suggested by Jamiolkowski and his colleagues (Fugro et al., 2016). Standards such as API and ISO recommend $K_o = 0.8$ for designing open-ended piles in sands and no K_o in clays. (Vugts, 2016).

3.2. Soil failure

3.2.1. Shear strength, friction, and Coulomb criterion

Shear strength is a property of cohesive soil independent of the normal stress σ_n. In clays, it is due to the sticky effect or bonding forces between the particles. Cohesion c keeps two clay particles intact, and adhesion a_s keeps clay and another material in contact. Friction, or Coulomb friction, is a property of non-cohesive soil[6] dependent on σ_n. Internal friction depends on the normal stress between two sand grains, and external friction on the normal stress between the sand grains and another material. The internal and external friction is denoted by the angle of internal friction φ and the angle of external friction δ, where the latter is often taken as $\delta = \varphi - 5°$. Sometimes friction-related properties are expressed as the internal friction coefficient $\mu_{in} = \tan(\varphi)$ and external friction coefficient $\mu_{ex}\tan(\delta)$.

When the cohesive and non-cohesive soils are mixed in the earth layer, both shear strength and friction contribute to their shear resistance. If the shear resistance is surpassed, the soil fails or starts to slide against each other or another material. Therefore, it is possible to define shear resistance as a failure criterion. This failure criterion is often called Coulomb criterion[7]. Following the Coulomb criterion, the shear stress at failure of a soil-soil τ_{in} and soil-other material interface τ_{ex} can be written as (Miedema, 2014; Terzaghi, 1943; Vugts, 2016).

$$\begin{aligned} \tau_{in} &= c + \sigma_n \tan(\varphi) \\ \tau_{in} &= c + \sigma_n \mu_{in} \end{aligned} \tag{3.6}$$

[6] It is valid as long as it is dry because wet sands have some cohesion.
[7] σ_n is assumed as the magnitude of the compressive stress in this case.

$$\tau_{ex} = a_s + \sigma_n \tan(\delta)$$
$$\tau_{ex} = a_s + \sigma_n \mu_{ex} \tag{3.7}$$

For saturated soils in this study, according to Section 3.1.3, the corresponding shear strength due to cohesion c is the undrained shear strength s_u. Thus the Coulomb criterion, can be written as

$$\tau_{in} = s_u + \sigma_n \tan(\varphi) \tag{3.8}$$

$$\tau_{ex} = \alpha_s s_u + \sigma_n \tan(\delta) \tag{3.9}$$

where α_s is a coefficient to relate the cohesion and adhesion in the undrained condition.

3.2.2. Mohr-Coulomb failure criterion

According to Mohr, a material failure is due to the resultant of all the stress components, be it normal stress or shear stress. The resultant stresses, where the shear stresses are zero at a special angle, are called the principal stresses. They can be derived to produce a circle with the centre point as the average normal stress σ_{av} and the radius r_M. For soil, this is the average effective normal stress σ'_{av}. (Miedema, 2014; Vugts, 2016)

$$\sigma'_{av} = \frac{\sigma'_x + \sigma'_z}{2} \tag{3.10}$$

$$r_M = \sqrt{\left(\frac{\sigma'_x - \sigma'_z}{2}\right)^2 + \tau_{xz}^2} \tag{3.11}$$

where σ'_x and σ'_z equal σ'_h and σ'_v, respectively, and τ_{xz} are the shear stress defined in Cartesian coordinates and in a two-dimensional stress state. Mohr circle shows that soil failure takes place when the circle touches the line of the Coulomb criterion. This failure is often defined as the Mohr-Coulomb failure criterion. The shear stress at failure τ^*_{in}, thus τ^*_{ex}, following Mohr-Coulomb criterion can be computed as (Brinkgreve, 2019; Miedema, 2014)

$$\tau^*_{in} = s_u \cos\varphi + \sigma'_{av} \sin\varphi \tag{3.12}$$

$$\tau^*_{ex} = \alpha\, s_u \cos\varphi + \sigma'_{av} \sin\delta \tag{3.13}$$

3.3. Soil behavior under dynamic loading

In this section, a literature survey on soil behavior under dynamic loading is discussed qualitatively by first introducing the idea of dynamic loads. Dynamic problems are distinguished from static ones by the inclusion of the inertia force effect. The inertia force becomes prominent as the frequency increases. For harmonic motion, the inertia force is proportional to the square of the frequency. Studies on soil dynamics are usually rooted in the study of the force exerted by nature, such as earthquakes, traffic loads, and wave-induced loads in the ocean. Earthquake impulses exert load at a frequency around 0.3 to $10\,Hz$ (Ishihara, 1996), wind-generated surface gravity waves in the ocean at a frequency around 0.03 to $4\,Hz$ (Holthuijsen, 2007), and traffic loads at a frequency around 30 Hz[8]. Besides, studies on man-made vibration, other than the vibratory pile installation, also exist, such as on the foundations for machines, which may deal with an operating frequency in the order of $160\,Hz$ (Arya et al., 1979).[9]

Significance of strain rate, number of cycles, and type of dynamic loads

Three main discussions regarding soil behavior under dynamic loading consist of the effect of rapid loading or strain rate, the effect of the number of cycles, and the effect of the forcing amplitude. First of all, the strain rate may actually be referred to the effect of frequency since the strain rate is the first derivative of the strain in time. Before further discussing the strain rate, it is best to make a reference

[8] According to EN 12697-24, fatigue test of asphalt pavement is conducted at this frequency.

[9] These range of frequency loads may assist the literature review in addition to the literature about the vibratory pile installation since the GDP shaker is aiming for optimizing the operating frequency.

frame regarding the loading rate. The loading rate or loading time will be approximated here as a quarter of the loading period $T_F = 0.25T$ (Ishihara, 1996), that is roughly the required time of a harmonic load in a sine form to reach its amplitude from zero forcing.

Based on rate process theory, it is hypothesized that the soil cohesion c and the internal friction angle $\tan(\varphi)$, and thus their external counterpart, increases linearly with the logarithm of the strain rate (Sathialingam & Kutter, 1989). Studies clarified that the strength of clays is greater in rapid loading than in slow loading. One of the earliest investigations of the strain rate effect is due to Casagrande. It is qualitatively due to the viscous nature of the soil, by assuming the Kelvin model, which gives smaller strain with the increasing loading speed (Ishihara, 1996). A more recent study shows that the resistance factor of a very soft clay increased by 9% for each $10 - fold$ increase in T-bar the penetration rate (Nanda et al., 2017). On the contrary, other studies suggested that only a slight increase of effective stress, and negligible effect on friction angle, may occur in saturated sands. It is because with increasing strain rate, saturated sands are forced to increase in volume, but at the same time, want to maintain the constant volume, which results in the increase of effective stress (Sathialingam & Kutter, 1989).

Unlike the effect of strain rate, clay's strength decreases as the loading cycles increase. In sand, the relationship between the shear stress at failure and the number of cycles at increasing cycles are essentially the same in clay. These cases of decreasing strength with the increase of cycles may be attributed to pore pressure build-up (Ishihara, 1996). Other authors in vibratory installation suggest fatigue and liquefaction to describe the effect of the number of cycles in clays and sands, respectively (Holeyman et al., 2002; Jonker, 1987; Vugts, 2016). As the pore pressure builds up, the effective stress tends to decrease as the total stress tends to stay the same, at one point, from one cycle to another cycle. Why does the pressure build up affect the strength of clay, which, on the basis of the Coulomb criterion, is independent of the effective stress? The answer will be that the undrained shear strength is, in fact, dependent on effective stress as documented by Ladd and Foot (Pisanò, 2021a).

Finally, different types of dynamic loads impart different effects on the soil strength (Ishihara, 1996). It is sometimes referred to as the effect of the average and cyclic shear stresses (Andersen, 2009; Pisanò, 2021b). They are the combined effect of a non-oscillating forcing function and the oscillating one, respectively, in time. While the non-oscillating amplitude can be monotonically increasing or constant in time, the oscillating one can be regular or irregular. Usually, only the regular harmonic load is discussed when describing laboratory test results. Two basics combination can be categorized as either a two-way cyclic or one-way cyclic loading. Two-way cyclic load means that the soil is loaded in a constant amplitude oscillating load, such as the same magnitude of compression and extension. When a non-oscillating amplitude is added such that the soil is loaded only in either compression or extension, it becomes a one-way loading. Conditions in between the two basic conditions can be a biased two-way, biased one-way, monotonic-cyclic, cyclic-monotonic, monotonically increasing cyclic loading, and so forth (Ishihara, 1996; Pisanò, 2021b).

In sands, the final effect seems to be the decrease of the shear stress at failure. However, in clays, the combination effect of strain rate and the number of cycles somewhat counteract each other. One study suggested that the concluding effect is the product of each effect (Lefebvre & LeBoeuf, 1987). The higher strength due to the loading rate tends to disappear as the number of cycles increases because the repetition effect becomes more prominent (Ishihara, 1996). Notably, these arguments are based on the laboratory test results, which were conducted at a frequency range lower than 15 Hz, meaning that it is lower than the standard vibrator frequency range. Therefore, they are only indicative for the study of the GDP shaker.

3.4. Ideal soil

3.4.1. Soil as a homogeneous, isotropic, linear elastic solid

As discussed in the preceding sections, the behavior of sands and clays is so complex that a rigorous mathematical analysis seems too complicated. Furthermore, it is exaggerated by the fact that the knowledge of the physical properties and boundaries between soil layers is always inadequate. This work then proceeds to replace sands and clays as described above with hypothetical materials referred to as ideal sands and ideal clays, which to some extent, can be characterized by their elastic properties,

shear strength, and friction(Terzaghi, 1943).

As for the case of modeling the monopile, a soil material model must be established to describe the mechanical behavior of the soil. The linear elastic theory will be used in this study because of its engineering practicality and ample references regarding linear elasticity theory. Therefore, error checking and improvement will be straightforward in the future. Furthermore, using the linear elasticity theory will minimize the complication of problem-solving. Also, as only a little research has been performed for the purpose of monopile extraction, it may serve as an insight into more advanced constitutive models.

For soil to be homogeneous, isotropic, and linear elastic material, the Navier equations govern the soil behavior, which in the r, θ, and z coordinates read (Howell, 2017)

$$\begin{aligned}
\rho\frac{\partial^2 u_r}{\partial t^2} &= f_r + (\lambda * + G)\frac{\partial}{\partial r}(\nabla\cdot\mathbf{u}) + G\left(\nabla^2 u_r - \frac{u_r}{r^2} - \frac{2}{r^2}\frac{\partial u_\theta}{\partial\theta}\right)\\
\rho\frac{\partial^2 u_\theta}{\partial t^2} &= f_\theta + \frac{1}{r}(\lambda * + G)\frac{\partial}{\partial\theta}(\nabla\cdot\mathbf{u}) + G\left(\nabla^2 u_\theta - \frac{u_\theta}{r^2} - \frac{2}{r^2}\frac{\partial u_r}{\partial\theta}\right)\\
\rho\frac{\partial^2 u_z}{\partial t^2} &= f_z + (\lambda * + G)\frac{\partial}{\partial z}(\nabla\cdot\mathbf{u}) + G\nabla^2 u_z
\end{aligned} \tag{3.14}$$

where u_r, u_θ, and u_z are the radial, circumferential, and longitudinal displacements, respectively. f_r, f_θ, and f_z are body forces in the radial, circumferential, and longitudinal direction, respectively. $\lambda* = \frac{Ev}{(1+v)(1-2v)}$ and $G = \frac{E}{2(1+v)}$ are the Lamé constants, $\nabla\cdot\mathbf{u} = \frac{1}{r}\frac{\partial}{\partial r}(ru_r) + \frac{1}{r}\frac{\partial u_\theta}{\partial\theta} + \frac{\partial u_z}{\partial z}$, and $\nabla^2 u_k = \frac{1}{r}\frac{\partial}{\partial r}\left(r\frac{\partial u_k}{\partial r}\right) + \frac{1}{r^2}\frac{\partial^2 u_k}{\partial\theta^2} + \frac{\partial^2 u_k}{\partial z^2}, k = r, \theta, z$.

Nevertheless, soil is not an ideal elastic material because stress and strain are not linearly related. Strains are not fully reversible on reduction in stress, and strains are time-dependent (Poulos & Davis, 1980). Except for steel subject to stresses within the elastic range, there is no construction material whose real mechanical properties are simple enough to be accepted as a basis for theoretical analysis. (Terzaghi, 1943). The same reasoning regarding the practicality holds to assume the soil as a homogeneous and isotropic material, which in reality, soil is likely inhomogeneous and anisotropic due to the sedimentation process. Inhomogeneous means the soil structure is not distributed uniformly across soil layers, and anisotropic means the soil mechanical properties are not the same in all directions. An example of these properties is shown in the result of the GDP shaker's experimental campaign, where the shear wave velocity is reported to be non-uniform within the radius of only $16\,m$ and depth of $8\,m$ (Gómez et al., 2022).

3.4.2. Mohr-Coulomb failure criterion for dynamic loading

For the soil to be an elastic material, the soil obeys Hooke's Law, meaning that the soil deformation will be reversible. It implies that there is no limit to the amount of stress that the soil can carry. At this point, the Mohr-Coulomb failure criterion will be employed. It should be pointed out that this criterion will not enter the equation of motion. To account for the effect of dynamic loading, a dynamic undrained shear strength s_{uD} may be introduced in the Mohr-Coulomb criterion to consider its possible increase due to strain rate effect as discussed in Section 3.3. The dynamic undrained shear strength may be defined as $s_{uD} = 2s_u$. The factor 2 is obtained by averaging the ratio of the cohesion under dynamic loading over the cohesion under static loading of clay soils based on research onshore Japan (Ishihara, 1996).

However, taking this factor can be problematic because of the following reasons. Firstly, the tests are performed on only three samples of soft clays and on land. The maximum static cohesion is in the order of $32\,kPa$, which is less than half of $70\,kPa$ being the limit of firm clay in Table 3.1. It is much smaller than the shear strength of the soil, which will be referred to in this work. As will be shown later, soil data from Borssele OWF is adopted, which has a much larger cohesion in the order of $200 - 600\,kPa$. All in all, there is a little reference about the behavior of clay under high frequency load that is accessible publicly, which means future research on this topic is demanded. This section concludes that the same failure criterion is assumed for the dynamic loading as in (3.12) and (3.13).

The pile-soil interface is the critical location to define the failure. Firstly, the shear stress away from

the pile is generally smaller due to the decaying behavior of cylindrical waves. Secondly, it is because $\tau_{ex}^{*} < \tau_{in}^{*}$ due to $\delta < \varphi$ and $a < c$. Therefore, τ_{ex}^{*} will be discussed. This study will first consider the failure criterion for sand. Following API and ISO in Section 3.1.4, $K_o = 0.8$ is used, and the failure criteria of sand becomes

$$\tau_{ex,sand}^{*} = \frac{\gamma_s^{'} z + K_o \gamma_s^{'} z}{2} \sin(\delta) \tag{3.15}$$

where $\delta = 45° - 5°$ and $K_o = 0.8$ as described in Table 3.2 and Section 3.1.4. The former considers very dense sand based on Section 3.5, which also leads to $\gamma_s^{'} = 2022 \times 9.81 \times z$. Hence, the failure criteria of sand can be plotted as in Figure 3.1. To verify Figure 3.1, an example of calculation for the $1\,m$ depth is made and reads

$$\begin{aligned} \sigma_v^{'}(z=1) &= (2022 - 1025) \times 9.81 \times |-1| \approx 9781\,Pa \\ \sigma_h^{'}(z=1) &= 0.8 \times 9781 \approx 7825\,Pa \\ \sigma_{av}^{'}(z=1) &= \frac{9781 + 7825}{2} \times \sin(40°) = 5658\,Pa \end{aligned} \tag{3.16}$$

which shows an error of $2\,Pa$ and deemed negligible. Therefore, the figure matches the formulation.

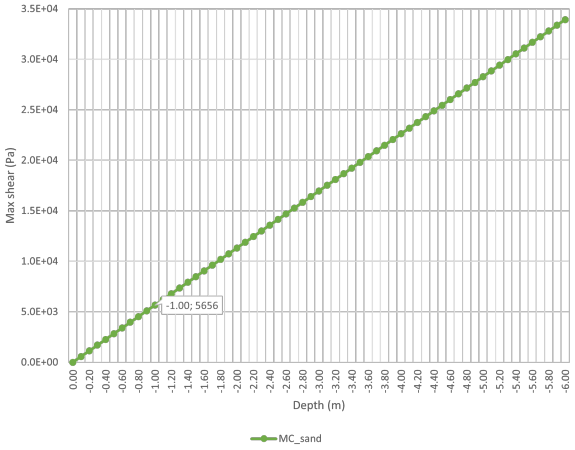

Figure 3.1: The assumed failure criteria for sand

3.4.3. Assumptions on the soil failure for the overall pile-soil system

Recalling Section 1.6 on the use of 3D FEM, Section 2.2 and Section 2.3 on the monopile idealization, and Section 3.4 on the soil idealization, the overall system is shown in Figure 3.2 or 7.18. The following assumptions on pile-soil behavior are described, which are suggested by Metrikine [10] and closely related to previous research regarding torsional pile responses (Dong Guo & Randolph, 1996) (Poulos, 1975) where a discretized soil layer act independently from the adjacent layers. The pile-soil system assumes a homogeneous, isotropic, and linear elastic material for both the pile and soil and perfectly bonded contact between the interfaces. The steady state response to the harmonic excitation due to the vibrator at the pile top is assumed. Two soil layers are distinguished based on the presence of the monopile, which are the upper layer that shares the same depth with the embedded length of the monopile and the lower layer or the additional soil layer where no monopile is embedded across this depth. The top layer assumes discrete layers, which in Figure 3.2 is shown by three soil layers.

The governing equations of the overall 3D pile-soil system will be (2.2) and (3.14) where $f_r = f_\theta = 0$ and $f_z = \rho g$. Assuming perfectly bonded contacts between the pile-soil and soil-soil interfaces,

[10](A. Metrikine, personal communication, 5 September, 2022)

displacement and stress continuity are prescribed. Dashpot (and spring) elements are assigned at the outer boundary both for the solution that propagates in r and z and a harmonic external load F_θ is excited at the pile top. Finally, the governing equations and the boundary condition will be solved by Ansys. The remaining task is to interpret the output, which is elaborated in the next chapter.

The goal is to find the soil failure at the outer part of the pile-soil interface in the vicinity of the monopile. The model assumes that the inner soil or usually called the soil plug, does not govern the soil failure. That is the pile will slide over the soil when the outer soil-pile interface fails. With three distinct top layers, three pile-soil contacts are the consequences. Pile-soil contact assumes a bonded contact, which enforces the continuity of both the displacement and stress. It is hypothesized that the failure takes place starting from the uppermost layer $l = 1$. The force $f_{o,1}$ will be defined as the minimum amplitude that fails the first layer $l = 1$, which is governed by the failure criterion described in Section 3.2.2. Generally, f_o can be determined by means of iteration.

It is hypothesized that every time the maximum shear surpasses the failure criterion, the contact between the pile and the soil fails. At each targeted depth, the simulation is tuned in such a way that the maximum shear stress of the soil outside the monopile exceeds the failure criterion defined in Section 3.4.2. If the pile-soil contact of the first layer fails, only the soil resistance from the remaining lower layers holds. At this point, the stress state from the last simulation is not accounted for as a perturbation to the next simulation. The iteration is done for each layer till all of the force amplitudes are materialized. For example, referring to Figure 3.2, three force amplitudes must be found (*i.e.* $f_{o,1}$, $f_{o,2}$, $f_{o,3}$). If more discrete layers are assumed, combinations due to the number of layers are conceivable, which leads to few hypothetical cases being examined and presented. By observing the results from each simulation, one can analyze the relation between the force amplitude of each simulation. To reduce the uncertainty of the results, a statistical sense will be assumed as a tool to analyze the relation between the discovered force amplitudes.

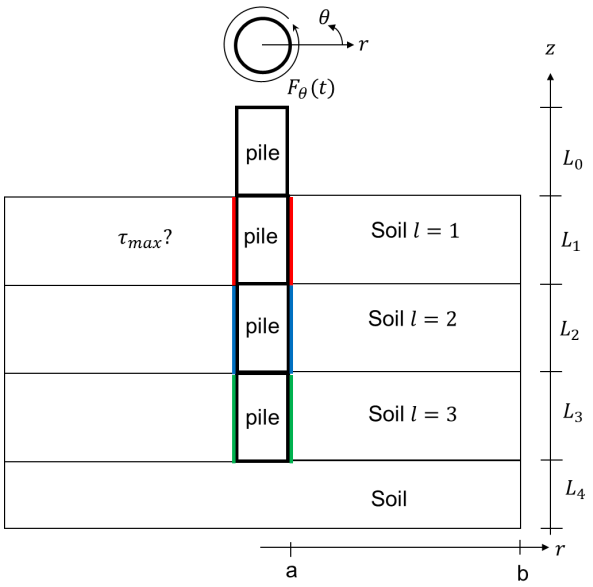

Figure 3.2: Overall pile-soil system

3.5. Input data acquisition

A geotechnical report that is made publicly available by the Netherlands Enterprise Agency is referred to determine the soil properties. The goal is to get an insight into real data, especially that is located in the North Sea, where the concern of monopile decommissioning is concentrated at. The report, produced by Fugro Engineers B.V. and reviewed by DNV GL, describes the in situ soil investigation for the Borssele Wind Farm Site (WFS) IV in the Dutch Sector of the North Sea. The interpreted

Cone Penetration Test (CPT)[11] logs from the seafloor at 24 locations, which are performed to depths ranging between $8.6\,m$ and $49.6\,m$ below the seafloor, will be the subject matter here. From this report, only soil density and soil type are exploited. The density of the soil is quantitatively computed by averaging the data so that $\rho = 2022\,kg/m^3$. Considering the worse condition for extraction, very dense sand and hard clay can be concluded as the composition of the soil layers. As the starting point, the soil layer will assume a very dense sand first. Other parameters are then derived from the qualitative soil descriptions using tables in the previous sections.

[11] Based on $Data1$, the penetration depth at this wind farm is $47\,m$. However, from the geotechnical report, it is impossible to penetrate the soil down to this depth in all locations. This statement is supported by the fact that several locations provide the CPT log data until the depth that is less than $47\,m$ due to the stopping criterion is exceeded. For example, at CPT_WFS4_11, the CPT data below $37\,m$ is not available. Therefore, $Data1$ is an approximation or not exact.

4

Interpreting Ansys Mechanical and the amplitude of the torque and clamping force

4.1. Harmonic analysis: the amplitude and phase of the steady-state response

Ansys Harmonic Response assumes the equation of motion as

$$\mathbf{M}\ddot{\mathbf{u}} + \mathbf{C}\dot{\mathbf{u}} + \mathbf{K}\mathbf{u} = \mathbf{f} \tag{4.1}$$

where $\mathbf{M}$, $\mathbf{C}$, and $\mathbf{K}$ are the mass, damping, and stiffness matrices, respectively. $\ddot{\mathbf{u}}$, $\dot{\mathbf{u}}$, $\mathbf{u}$, and $\mathbf{f}$ are the acceleration, velocity, displacement, and force vectors, respectively. While $\mathbf{M}$, $\mathbf{C}$, and $\mathbf{K}$ are known due to the geometry, material input, and the boundary or interface conditions. $\mathbf{f}$ is known due to the prescribed force. The only unknown is $\mathbf{u}$, from which the first and second derivative in time gives $\dot{\mathbf{u}}$ and $\ddot{\mathbf{u}}$. For a harmonic analysis, the force vector is in the form of

$$\mathbf{f} = (\mathbf{f_o} \exp(i\psi)) \exp(i\omega t) \tag{4.2}$$

where $\mathbf{f_o}$, ψ, ω, and t are the force amplitude, initial phase angle, angular frequency, and time. For a straightforward interpretation during post-processing, $\psi = 0$ is put every time the simulation is run. Therefore,

$$\mathbf{f} = \mathbf{f_o} \exp(i\omega t) \tag{4.3}$$

The steady-state response to the above forcing input will oscillates in the same frequency ω, which Ansys searched for in the form

$$\mathbf{u} = (\mathbf{u_o} \exp(i\phi)) \exp(i\omega t) \tag{4.4}$$

where $\mathbf{u_o}$ and ϕ are the displacement amplitude and its phase angle. Substituting (4.3) and (4.4) to (4.1) leads to

$$\left(\tilde{\mathbf{K}}\tilde{\mathbf{u}} = \mathbf{f_o}\right) \exp(i\omega t) \tag{4.5}$$

where the complex displacement response $\tilde{\mathbf{u}} = \mathbf{u_o} \exp(i\phi)$ and the complex stiffness $\tilde{\mathbf{K}} = \left(-\omega^2\mathbf{M} + i\omega\mathbf{C} + \mathbf{K}\right)$. The latter can also be written as $\tilde{\mathbf{K}} = \mathbf{K_o} \exp(i\Phi)$, where $\mathbf{K_o}$ is the stiffness amplitude and Φ is its phase angle. Therefore,

$$\mathbf{u_o} = \frac{\mathbf{f_o}}{\mathbf{K_o}} \exp\left(-i(\phi + \Phi)\right) \tag{4.6}$$

Substituting (4.6) to (4.4) yields

$$\begin{aligned} \mathbf{u} &= \left(\frac{\mathbf{f_o}}{\mathbf{K_o}} \exp\left(-i(\phi + \Phi)\right) \exp(i\phi)\right) \exp(i\omega t) \\ &= \frac{\mathbf{f_o}}{\mathbf{K_o}} \exp\left(i(\omega t - \Phi)\right) \end{aligned} \tag{4.7}$$

Note that the use of complex exponential form here is an auxiliary thanks to Euler as in (5.4). Physically, the forcing input can be either in a co-sinusoidal or sinusoidal form, which oblige the user to take either the real or imaginary part. So does the displacement response. From (4.3) and (4.7), this work assumes a force in the form $\mathbf{f} = \mathbf{f_o} \cos(\omega t)$ that leads to the response in the form $\mathbf{u} = \mathbf{u_o} \cos(\omega t - \Phi)$. $\mathbf{u_o}$ and Φ are related to $\mathbf{u}$ by

$$\mathbf{u_o} = \sqrt{Re(\mathbf{u})^2 + Im(\mathbf{u})^2} \tag{4.8}$$

and

$$\Phi = \arctan\left(\frac{Im(\mathbf{u})}{Re(\mathbf{u})}\right) \tag{4.9}$$

where Φ is determined in $[-\pi, \pi]$ by the four-quadrant inverse tangent. With these, the interpretation of the real and imaginary part of the displacement from Ansys harmonic analysis is closed.

4.2. Static analysis

In order to take into account the effect of gravity, the Static Structural toolbox in Ansys is utilized. In what follows, Figure 7.18 is referred and a cylindrical coordinate system in the figure is assumed. The effect of gravity will be assumed such that the vertical stress follows the hydrostatic pressure distribution, which reads $\sigma_v = \sigma_{zz} = \gamma_{s,wet} z$, by doing two procedures. The boundary condition at the outer radius is set as $u_r(b, \theta, z, t) = 0$, that is to prescribe zero displacements in the r-direction. Next to that, the boundary condition at the bottom boundary assumes a fixed boundary so that $u_r(r, \theta, z_\Omega, t) = u_\theta(r, \theta, z_\Omega, t) = u_z(r, \theta, z_\Omega, t) = 0$.

4.3. Pre-stressed harmonic analysis

The so-called pre-stressed harmonic analysis is used to consider the effect of the initial stress due to the self-weight. In the Ansys Workbench, the Static Structural toolbox is first dragged and dropped on the *Project schematic*. Secondly, the Harmonic Response toolbox is also dragged and dropped on the *Model* of the Static Structural that is already in the project schematic. The first verification on this task is to open the Harmonic Response toolbox and make sure that the word *Pre-stress* appears above the *Analysis settings*. Afterwards, the Harmonic Response toolbox simulation is understood by the comprehension in Section 4.1. One way to verify the pre-stressed simulation result is to compare it with a simplified analytical solution, which will be shown in the test cases.

4.4. The amplitude of the torque and clamping force

For a given force amplitude f_o at the pile top that fails the soil layer as introduced in Section 3.4.3, the required torque T_o reads

$$T_o = f_o R_p \tag{4.10}$$

where the radius of the monopile R_p is approximated as the half of the monopile diameter $R_p \approx D_o/2$. The force amplitude f_o is also directly related to the clamping force N_o following the Coulomb criterion as in Section 3.2.1 and illustrated in Figure , which must be provided normal to θ-direction (*i.e.* in the r-direction) and reads

$$N_o = \frac{f_o}{\mu_{ex,ss}} \tag{4.11}$$

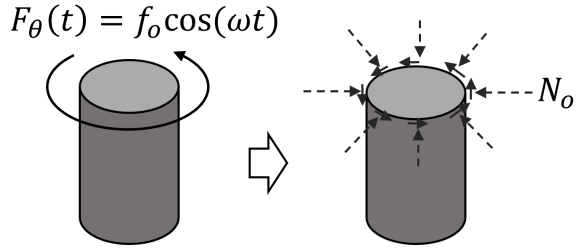

Figure 4.1: f_o-N_o relation

where $\mu_{ex,ss}$ is the static external friction coefficient of a steel-steel contact. The use of $\mu_{ex,ss}$ stands on the ground of the following assumptions[1]. The clamping tools are made of a hardened steel much like the monopile's steel. A static friction coefficient holds due to no slip criteria and constant during the vibration. Since the ocean environment is concerned and the distance between the pile top and the sea surface is close, the pile-clamp connection will tend to slide due to wet condition if one assumes flat surfaces between the two. A mechanical connection between the clamp and monopile is assumed to reduce the chance of slip, which can be done by configuring teeth on the clamp's surface so that the clamp can penetrate the monopile. Therefore, a relatively high friction coefficient can be obtained between $\mu_{ex,ss} = 0.7$ and $\mu_{ex,ss} = 0.8$ to grip the monopile due to the mechanical connection. Finally, N_o is the minimum normal force for the mechanical connection and not necessarily the force to penetrate the monopile.

4.5. Computing the required power

At the end of this study, the required power is calculated to indicate whether the current GDP shaker operating power, which is around $200\,kW$, meets the demand or not. The instantaneous power P is defined as the rate d/dt of the work done W, which in this study reads[2] (Grote & Hefazi, 2021)

$$P(t) = \frac{d\,W}{dt} = \sum F(t)v(t) \tag{4.12}$$

where $\sum F(t)$ and $v(t)$ must be defined as the total applied force and the resulting velocity at the pile top in the θ-direction. For a co-sinusoidal load, from Section 4.1, the instantaneous power reads

$$\begin{aligned} P(t) &= Re\left(f_o \exp(i\omega t)\right)\, Re\left(i\omega u_o \exp(i\Phi)\exp(i\omega t)\right) \\ &= f_o \cos(\omega t)\,(-\omega) u_o \sin(\omega t - \Phi) \\ &= \frac{1}{2} f_o \omega u_o \big(-\sin(2\omega t - \Phi) + \sin(\Phi)\big) \end{aligned} \tag{4.13}$$

[1](S.C.H. van der Burg, personal communication, 14 February, 2023)
[2](A. Tsetas, personal communication, 6 February, 2023)

where f_o and u_o are the force and displacement amplitude at the pile top. It is useful to address the power in terms of average power over one period[3] $T = 2\pi/\omega$ (Wolf, 1985), which can be computed as

$$\begin{aligned} P_{ave} &= \frac{1}{T}\int_0^T P(t)dt \\ &= \frac{\omega}{2\pi}\int_0^{\frac{2\pi}{\omega}} f_o \cos(\omega t)\,(-\omega) u_o \sin(\omega t - \Phi)\; dt \\ &= \frac{1}{2} f_o \omega u_o \sin(\Phi) \end{aligned} \tag{4.14}$$

(4.14) shows that the average power has no t anymore due to integration and it is maximum when the phase of the output velocity is $\pi/2$ with respect to the phase of the input force. With these, for a given output of both the real and imaginary part of the displacement at the pile top due to an applied harmonic load, the power can be determined.

[3](S.S. Gómez, personal communication, 13 February, 2023) (A.V. Metrikine, personal communication, 20 February, 2023)

5

Analytical model

5.1. Modeling framework

Geometrical model of soil and minimizing error

A general method through which an infinite system may be approximated by an FE model is with the use of viscous elements at the outer boundary. The viscous boundary is a damping force that is assumed to be proportional with the velocity at the boundary. Theoretically, in the one-dimensional analysis of wave propagation, when a disturbance encounters this element, it is possible to adjust the damping force in such a way that no reflection occur. When such adjustment is made, the viscous boundary is called a non-reflective or absorbing element/boundary (Deeks & Randolph, 1994; Lysmer & Kuhlemeyer, 1969; Metrikine & Vrouwenvelder, 2021). It is to prevent excessive errors of the solution[1] in the interior domain due to reflection. Reflection occurs when other types of boundary are used such as kinematic/essential boundaries[2] or dynamic/natural boundaries[3], which will result in a standing wave field. The standing wave field indicates that the energy is kept in the interior domain. When the material damping is sufficiently low, which is common in engineering systems, this will lead to an erroneous results.

Concerning erroneous results, three sources of error in FE modeling consists of modeling error, discretization error, and numerical error, since FE modeling is by definition an approximation (Oñate, 2009). Modeling error comes from the continuum model and its boundary, because these two are defined separately but together define the displacement solution. In the continuum, defining an ideal soil is seen as the main source of modeling error because this is not complete to model real soils. This error can be minimized, if not overcome, by introducing a more representative constitutive models.

The first of modeling the boundary is about its general geometries such as whether the soil domain is rectangular cubical or circular cylindrical. It is recommended to employ a circular boundary to avoid concentrated solutions (*i.e.* displacement, stress, etc.) at the corners of rectangular domain due to wave reflection at the boundary [4]. The second is about the use of viscous boundary, which is introduced earlier. Therefore, both the use of the circular domain and the viscous boundary are seen as two ways of minimizing modeling error at the boundaries. A proper definition of the viscous elements, thus the magnitude of the damping force, is crucial to minimize the modeling error.

The discretization[5] error is mitigated mainly by using a sufficiently fine element size Δl. In dynamic analysis, it is treated by applying a minimum of 10 elements per wavelength $\Delta l = \lambda/10$ as a rule of thumb and a finer mesh up to $\Delta l = \lambda/20$ is recommended to obtain more accurate results [6]. Other authors recommend $\Delta l = \lambda/8$ to $\Delta l = \lambda/10$ (Vacareanu et al., 2019) and $\Delta l \leq \lambda/12$ (Lysmer & Kuhlemeyer,

[1] In this study, the solution is in terms of displacement and shear stresses will be the main focus.
[2] Fixed or free boundary
[3] Element of mass or spring
[4] (A. Metrikine, personal communication, 5 September, 2022)
[5] Only the spatial discretization is considered due to the steady state assumptions.
[6] (A. Tsetas, personal communication, 7 October, 2022)

1969). Following the subject-matter experts, $\Delta l \leq \lambda/10$ is taken as a moderate choice for the starting point. The numerical error is usually significance when discontinuites of material properties exists (Oñate, 2009), which matters at the pile-soil interface. To minimize this error, mesh conformity [7] is applied at best by contact sizing and contact matching. Since the pile element seems governing in this case, a convergence check must be performed for different element sizes of the pile. Therefore, two mesh criterion should be satisfied, the first one is to minimize the discretization error, and the second one is to minimize the numerical error.

Benchmarking

Before continuing with the application of the viscous boundary, a frame reference is made to Figure 7.18, from now on, to guide the discussion on the overall modeling. Figure 7.18 features the circular cylindrical monopile, soil domain, coordinates, and their corresponding nomenclatures. Two questions arise when discussing the soil geometries for the FE modeling: To what extent the soil domain needs to be modeled? Considering the ability of the absorbing boundary, it is thus favorable to truncate the soil domain as small as possible to ease the computational effort, but what is the limit?

A study offered relationships to define an optimum lateral extent D_Ω of a soil domain based on FE analyses of soil structure interaction due to earthquakes in OpenSEES. The study employed a pressure dependent constitutive model with 2% Rayleigh damping in the continuum and the so-called Lysmer-Kuhlemeyer (LK) viscous dashpot or the standard viscous boundary[8]. The FE model are verified against another numerical study in the literature. These relationships show that D_Ω must increase with the peak ground acceleration (PGA) and width of the structures/foundations D_o. Also, it indicates that the effect of D_Ω becomes small, if a minimum of $D_\Omega = 10D_o$ is applied, based on comparing three cases of D_o including $15\,m$, $27\,m$, and $45\,m$ (Sharma et al., 2020). No information available on the optimum vertical extent H_Ω, but it assumes a bedrock boundary $30\,m$ below the ground surface. It is concluded to hold the suggestion on $D_\Omega = 10D_o$ and to leave behind the suggested PGA relationships because this thesis applies no PGA input.

Another study, on the vibratory pile installation, suggested that the vibration influence at $33.3\,Hz$, in terms of peak particle velocity (PPV), measured from the monopile's outer diameter, extends up to around $L_{\Omega p} = 5.6D_o$ or $D_\Omega = 5.6 \times 2 + 1 = 12.2D_o$, which is not sensitive to different centrifugal force inputs $225\,kN$, $270\,kN$, and $315\,kN$. Unlike the previous reference, the second literature employed an elastic-plastic constitutive model with 10% damping ratio, and the so-called truncation boundary with $D_\Omega = 30\,m$ and $H_\Omega = 20\,m$ in FLAC3D. The FE analysis are validated against field tests, which show that the deviation of the PPV are negligible at $L_{\Omega p} \geq 5D_o$ (Wei et al., 2022). Albeit no clear conclusion is made about the vibration influence below the pile tip, it gives a clue that at around $H_{\Omega p} = 13D_o$, the vibration becomes negligible. It can be perceived that the two studies deduce a roughly similar horizontal far-field location from the monopile at $L_{\Omega p} = 0.5 \times 10D_o - 0.5 \times D_o = 4.5D_o$ and $L_{\Omega p} = 5.6D_o$. The latter study suggests a vertical far-field location at $H_{\Omega p} = 13D_o$. It is then decided to take $L_{\Omega p} = 5.6D_o$ thus $L_{\Omega p} = 6D_o$ by rounding up and $H_{\Omega p} = 13D_o$[9] as the starting point for evaluating the FE analysis later on.

The need for verification and validation

Verification and validation are the primary methods to assess the confidence into the FE analysis results. Validation is often associated with comparison with either laboratory or field experiments, which means creating a relationship between the FE analysis with the real world. On the other hand, verification does not build a direct FE analysis-real world relation. It constitutes the relation between the FE analysis versus the conceptual model, in which the conceptual model stands on the grounds of real world physics. In other words, while verification proves that the FE analysis solves a problem accurately, validation proves that the FE analysis solves the right problem (CEN, 2015; Oñate, 2009). Verification can be done by comparison with an established accurate numerical model or with

[7] (C. Kasbergen, personal communication, 21 December, 2022)

[8] The LK boundary suggests two coefficients of viscous boundary in the form $\sigma_{dp} = a_{dp}\rho c_1 \ddot{u}_{normal}$ and $\tau_{dp} = b_{dp}\rho c_2 \ddot{u}_{tangent}$ where c_1 and c_2 are the speed of P- and S-waves, respectively. $\ddot{u}_{normal}$ and $\ddot{u}_{tangent}$ are the velocities normal- and tangent to the boundary, respectively. Most of the time $a_{dp} = 1$ and $b_{dp} = 1$. So, the coefficient of the dashpot elements are $c_{dp,normal} = a_{dp}\rho c_1$ and $c_{dp,tangent} = b_{dp}\rho c_2$ (Lysmer & Kuhlemeyer, 1969).

[9] This is because little information is obtained from the literature, which performed dynamic analysis with considerably high frequency load and conclude this type of information.

benchmark problems derived from exact analytical solutions (Oñate, 2009; Wellens, 2021). This study focuses only on the verification by comparing with analytical solutions. However, exact analytical solutions are often available only for simplified problems, which is exemplified in the following sections. After all, they can be used as a starting point for guiding the thinking process down to the future validation.

5.2. Developing analytic model

To tackle problems in Section 5.1, an analytical model is developed in Maple and Mathematica. The analytical model illustrates a cylindrical soil cavity that is perfectly bonded with a rigid ring at the inner boundary, under a plane strain and linear elastic assumption [10]. The appearance of cavity is not realistic, because the soil inside the monopile exists in reality. It is intended to avoid mathematical complications when solving the conditions at the origin radius. The effect of the vibrator mass is first neglected because it acts only at the top. To achieve a conservative result, a perfectly bonded assumption at the pile-soil interface is made.

In order to make apples to apples comparison, the FE analysis will be broken down into smaller steps, in which it begins with a model that is as close as possible to the analytic model [11]. It starts with the 2D plane strain model. By applying this technic, a more complicated phenomena may be identified step by step when the FE model is tailored from the 2D model to the 3D model.

A plane strain assumption is made by assuming that $L_p \gg D_o$, which is plausible for monopiles in this study. Whenever there is a load perpendicular to the longitudinal elements and it does not vary along the length[12], it is assumed that all cross sections are in the same condition (Timoshenko & Goodier, 1951). Additionally, as introduced in Section 3.4.1, this study will employ linear elastic theory despite elastic bodies are generally governed by nonlinear equations for their three-dimensional motions. However, an examination of a problem based on linearized equations often leads to considerable insight into the actual physical situation. By linear equations, the system will be easier to understand and the principle of superposition applies (Achenbach, 1975). Therefore, the linearized theory of wave propagation in elastic bodies is used.

Furthermore, the solution is sought in the form of steady state solution to a harmonic load. It is because the GDP shaker or pile vibrator generally employs a harmonic excitation. Provided that the system is stable, the steady state condition is the condition where the transient regime ended due to energy dissipation from the distributed damping, leaving only the response due to the external force. The steady state response is independent of the initial conditions. Therefore, it is sufficient to only consider the particular solution. One may think that the problem should be considered as a transient problem, where, for example, a modal analysis would be more appropriate to capture the short term responses. The answer to this question is unknown, thus, subject for future research.

5.3. Undamped torsional motion

5.3.1. Forced torsional motion in a semi-infinite pile-soil

Consider a semi-infinite media in cylindrical coordinates, as shown in Figure 5.1, that is bounded by a rigid ring at $r = a$. Shaded area, bold circle, and dashed circle depicts the cavity, rigid ring, and the infinite extend of the medium at large r, respectively. While the media represents a soil continuum having mass density ρ and shear modulus G, the ring represents a monopile. The rigid ring assumption is justified because the rigidity of steel is much larger than the soil $G_p \gg G$. This is by limiting the analysis up to the soil characterized by the shear wave velocity of $360\,m/s$, which corresponds to the upper limit of medium dense sand and stiff clay in accordance with Eurocode 8 (CEN, 2004a). Under a plane strain assumption, only coordinate r and θ are referred. The system is subjected to a torsional excitation in the form of harmonic time function with a constant amplitude, that is assumed to be distributed symmetrically along the monopile top. A symmetrically distributed load results in an

[10] (A. Metrikine, personal communication, 26 June, 2022)

[11] (S.S. Gómez, personal communication, 4 October, 2022) (C. Kasbergen, personal communication, 16 December, 2022)

[12] In fact, harmonic variation due to the exerted harmonic torsion at the pile top will be generated. By assuming linearity, the effect of variation may be obtained as a superposition of the same stresses with different phases.

axially symmetric stress distribution along the monopile's cross-section. The change of strains in θ and z direction are thus zero (*i.e.* $\partial/\partial\theta = 0$ and $\partial/\partial z = 0$).

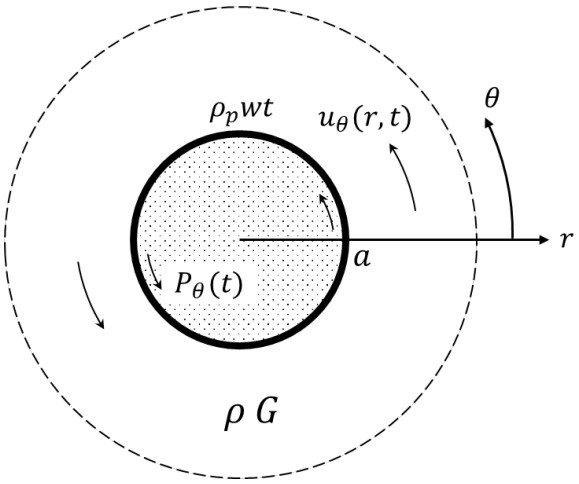

Figure 5.1: Semi-infinite model

The equation of motion for small amplitude displacement $u_\theta(r,t)$, in the absence of body force f_θ, gravitational field, and energy dissipation, as derived in Appendix B, reads

$$u_\theta'' + \frac{1}{r}u_\theta' - \frac{1}{r^2}u_\theta = \frac{1}{c_2^2}\ddot{u}_\theta, \qquad a < r < \infty \tag{5.1}$$

where the displacement in the θ direction is a function of radius and time $u_\theta(r,t)$, the superscript $'$, $''$, and accent $\ddot{}$ denote $\partial/\partial r$, $\partial^2/\partial r^2$, and $\partial^2/\partial t^2$, respectively, and $c_2 = \sqrt{G/\rho}$ is the shear wave propagation speed[13]. Initial conditions are not formulated following the steady state assumption. Two other conditions are required to complete the problem statement of this second order partial differential equation (PDE). Firstly, the boundary condition at $r = a$ reads

$$\{m_p\ddot{u}_\theta = P_\theta + \tau_{r\theta}\}_{r=a} \tag{5.2}$$

where the torsional excitation is defined as $P_\theta(t) = \tau_o\cos(\omega t)$. The pile's mass $m_p = \rho_p\, wt$, where ρ_p is the mass density of the pile and wt is the pile's thickness. By inspection, the boundary condition at $r = a$ has a unit of stress. Secondly, the radiation condition holds for which inward-propagating waves must not exist.

Because the forcing input $P_\theta(t)$ is harmonic with an angular frequency ω, the excited shear wave of the soil will also be harmonic having the same angular frequency ω (Metrikine & Vrouwenvelder, 2021). Also, it is assumed that the spatial and temporal solution is separable. With these assumptions, a straightforward way to solve the problem at hand is by assuming a solution in the form

$$u_\theta(r,t) = Re\big(U_\theta(r)\exp(i\omega t)\big), \qquad i = \sqrt{-1} \tag{5.3}$$

where $U_\theta(r)$ is an unknown function, which depends on r, may depend on ω, is independent of t, and to be determined from the boundary conditions. The $\exp(i\omega t)$ is the complex form of a harmonic wave, which according to Euler

$$\exp(i\omega t) = \cos(\omega t) + i\sin(\omega t) \tag{5.4}$$

where i is the imaginary unit as in (5.3). The Euler's formula in (5.4) stores both the cosine and sine function, with angular frequency ω, in time t, in one formula. This capability helps the analysis when the external load is either in cosine or sine form. Re means taking the real part of the complex solution inside the bracket $()$ in (5.3) because the excitation is defined in the form $P_\theta(t) = \tau_o\cos(\omega t)$. If the

[13]The subscript follows Graff's notation for c_1 is the compression wave speed and c_2 is the shear wave speed

external load is in the form $P_\theta(t) = \tau_o \sin(\omega t)$, then Im should be used to take the imaginary part of the complex solution (Metrikine & Vrouwenvelder, 2021).

Substituting (5.3) into the governing equations (5.1) and (5.2) reads

$$\left(U_\theta'' + \frac{1}{r}U_\theta' - \frac{1}{r^2}U_\theta = -\frac{\omega^2}{c_2^2}U_\theta\right)\exp(i\omega t) \tag{5.5}$$

$$\left\{-\omega^2 m_p U_\theta - G\left(\frac{dU_\theta}{dr} - \frac{U_\theta}{r}\right) = \tau_o\right\}_{r=a} \exp(i\omega t), \tag{5.6}$$

for non-trivial solutions (*i.e.* the existence of periodic amplitude)

$$U_\theta'' + \frac{1}{r}U_\theta' + \left(\beta^2 - \frac{1}{r^2}\right)U_\theta = 0, \qquad \beta = \frac{\omega}{c_2} \tag{5.7}$$

$$\left\{-\omega^2 m_p U_\theta - G\left(\frac{dU_\theta}{dr} - \frac{U_\theta}{r}\right) = \tau_o\right\}_{r=a} \tag{5.8}$$

the equation of motion (5.7) is in the ω domain and has the form of Bessel equations with the wavenumber β. The general solution to this equation is (Bowman, 1958; Graff, 1975; Maplesoft, 2022)

$$U_\theta(r) = A_1 H_1^{(1)}(\beta r) + A_2 H_1^{(2)}(\beta r) \tag{5.9}$$

where A_1 and A_2 are the two unknown contants to be determined from the two conditions. These constants are sufficiently small but not zero and sufficiently large but not infinity. $H_1^{(1)}(\beta r)$ and $H_1^{(2)}(\beta r)$ are the first order Hankel function of the first kind and the first order Hankel function of the second kind, respectively. They are defined as

$$\begin{aligned} H_1^{(1)}(\beta r) &= J_1(\beta r) + i\,Y_1(\beta r) \\ H_1^{(2)}(\beta r) &= J_1(\beta r) - i\,Y_1(\beta r) \end{aligned} \tag{5.10}$$

where $J_1(\beta r)$ is the Bessel function of the first kind, $Y_1(\beta r)$ is the Bessel function of the second kind. Notice that the first of (5.10) has a similar form with (5.4). The next step is to substitute the general solution into the boundary and radiation condition. Firstly, the radiation condition is investigated. Before solving the radiation condition, the proportionality of the asymptotic expansions of the Hankel functions at large r are first noted (Wolfram Alpha, 2022a, 2022b).

$$\begin{aligned} H_1^{(1)}(\beta r) &\sim \frac{\sqrt{2}}{\sqrt{\pi\beta r}}\exp\left(i\left(\beta r - \frac{3\pi}{4}\right)\right) \\ H_1^{(2)}(\beta r) &\sim -i\frac{\sqrt{2}}{\sqrt{\pi\beta r}}\exp\left(-i\left(\beta r - \frac{3\pi}{4}\right)\right) \end{aligned} \tag{5.11}$$

(5.11) shows that $H_1^{(1)}(\beta r)$ gives inward-propagating waves when multiplied with the time function $\exp(i\omega t)$ as in (5.3)[14]. Therefore, to satisfy the radiation condition, A_1 must be set to zero (Graff, 1975; Metrikine & Vrouwenvelder, 2021). Now (5.9) becomes

$$U_\theta(r) = A_2 H_1^{(2)}(\beta r) \tag{5.12}$$

Secondly, (5.12) is substituted into the boundary condition in (5.8) to give

$$\frac{1}{a}\left(-\beta a G A_2\left(H_0^{(2)}(\beta a) - \frac{H_1^{(2)}(\beta a)}{\beta a}\right) + \left(-a\omega^2 m_p + G\right)A_2 H_1^{(2)}(\beta a) - \tau_o a\right) = 0 \tag{5.13}$$

[14] The outward-propagating waves are formed if the argument of the exponential function of space and time have different sign, such as $\exp(i(-\beta r + \omega t))$. As a wave tends to keep its constant phase, r must increase with t.

Solving for A_2 leads to

$$A_2 = \frac{\tau_o a}{-a\omega^2 m_p H_1^{(2)}(\beta a) - \beta a G H_0^{(2)}(\beta a) + 2G H_1^{(2)}(\beta a)} \tag{5.14}$$

Therefore,

$$u_\theta(r,t) = Re\left(\frac{\tau_o a}{\left(-a\omega^2 m_p + 2G\right) H_1^{(2)}(\beta a) - \beta a G H_0^{(2)}(\beta a)} H_1^{(2)}(\beta r)\ \exp(i\omega t) \right) \tag{5.15}$$

On the basis of the uniqueness theorem, it is the solution if it satisfies the prescribed displacement or stress (Achenbach, 1975). (5.15) implies that the soil response is linearly proportional to the amplitude of the forcing τ_o, which makes sense due to the assumptions on linear PDE. However, the influence of the other parameters coming from the mechanical properties of both the pile, soil, and forcing frequency are not readily explainable because they show up both in the numerator and denominator, after rationalization is made and taking the real part. An important behavior due to $H_1^{(2)}(\beta r)$ is that the soil response decays with the increase of radius. The amplitude decay is naturally attributed to cylindrical waves that propagate outward because the same amount of total energy E_{KV} is distributed across the increasing area due to increasing perimeter. It decays proportionally to $1/\sqrt{r}$ as can be seen in (5.11) [15]. Note that this is not a decay due to damping whatsoever, since energy dissipation in the continuum is not introduced in this particular case.

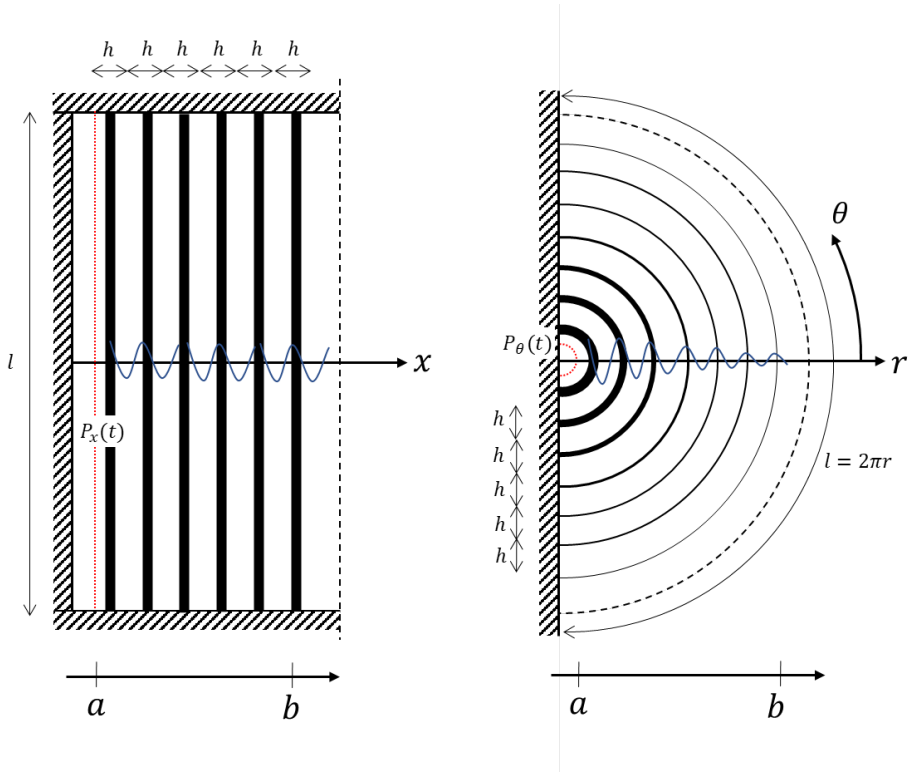

Figure 5.2: Plane waves in Cartesian and cylindrical coordinates

Figure 5.2 illustrates qualitatively the logic behind the decaying amplitude of cyclindrical waves. Let plane waves, in Cartesian coordinates, be generated due to energy from a uniformly distributed harmonic load $P_x(t)$ at $x = a$ along the red dotted line l_a. The total energy given is proportional to the square of the displacement amplitude at the source $E_{KV} \sim A_a^2$ [16] (Graff, 1975). The energy density, the total energy over an area, is thus $\mathrm{E}_{kv} \sim A_a^2/(l_a h_a)$ or $\mathrm{E}_{kv} \sim A_a^2/l_a$, since the thickness h is constant.

[15](A. Metrikine, personal communication, 29 November, 2022)
[16](A. Metrikine, personal communication, 29 November, 2022)

If the energy and area are constants, the amplitude of the energy density will also be constant when it propagates to larger x, that is $\mathrm{E}_{kv} \sim A_a^2/l$. In cylindrical coordinates, the energy density at a is thus $\mathrm{E}_{kv} \sim A_a^2/(2\pi r_a)$. The area increases with l as the wavefront propagates to larger r, where $l = 2\pi r$. For the energy to be constant, at $r > a$, the energy density decreases as $\mathrm{E}_{kv} \sim A_a^2/r$ (Jr. Roger Easton, 2004). Therefore, in the displacement amplitude sense, the wavefront amplitude must decrease as $A(r) = A_a/\sqrt{r}$.

5.3.2. Finding the non-reflective coefficient

Section 5.3.1 has established the steady-state wave motion without distributed damping in the soil medium as a consequence of distributed torsional action at radius $r = a$. Imagine that the corresponding wave field is shown in Figure 5.3, where the waves have propagated away from the perturbation radii at $r = a$, depicted by a dashed circle. If viscous elements c_{dp} are attached to one of the medium end at radius $r = b$, the system becomes finite.

The equation that governs the torsional motion reads

$$u_\theta'' + \frac{1}{r}u_\theta' - \frac{1}{r^2}u_\theta = \frac{1}{c_2^2}\ddot{u}_\theta, \qquad a < r < b \tag{5.16}$$

(5.16) is in general has the same form with (5.1) except that (5.16) physically works only in the range of $a < r < b$. For the system to be finite ended by dashpot elements at $r = b$, the force equilibrium at

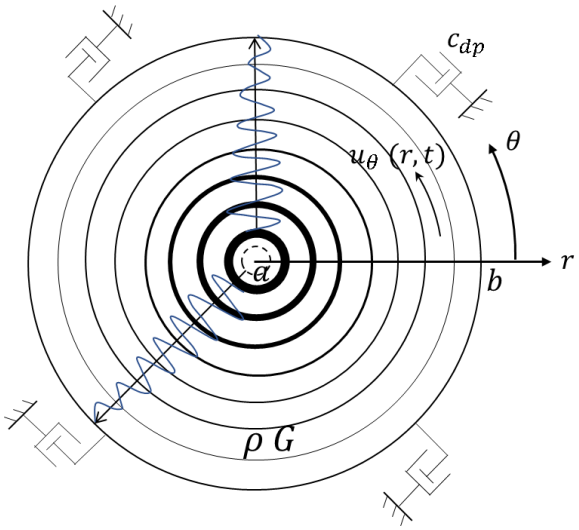

Figure 5.3: Illustration of a steady state wave field due to torsional action with the wavefront approaches dashpot elements

$r = b$ reads

$$\left\{c_{dp}\dot{u}_\theta = -\tau_{r\theta}\right\}_{r=b} \tag{5.17}$$

(5.17) is the boundary condition that supersedes the radiation condition of the semi-infinite problem in Section 5.3. At the other end, at $r = a$, the same boundary condition with (5.2) holds

$$\left\{m_p\ddot{u}_\theta = P_\theta + \tau_{r\theta}\right\}_{r=a}$$

Assuming a solution in the form (5.3), the governing equations, for non-trivial solutions, become

$$\begin{gathered} U_\theta'' + \frac{1}{r}U_\theta' + \left(\beta^2 - \frac{1}{r^2}\right)U_\theta = 0, \qquad \beta = \frac{\omega}{c_2} \\ \left\{-\omega^2 m_p U_\theta - G\left(\frac{dU_\theta}{dr} - \frac{U_\theta}{r}\right) = \tau_o\right\}_{r=a} \end{gathered} \tag{5.18}$$

$$\left\{ i\omega c_{dp} U_\theta + G\left(\frac{dU_\theta}{dr} - \frac{U_\theta}{r}\right) = 0 \right\}_{r=b} \tag{5.19}$$

The general solution to the first of (5.18) is (5.9). To derive the non-reflective coefficient, the the substitution of the known constant A_2 in (5.14) into the general solution (5.9) is not necessary. Instead, to arrive at the least mathematical formulation, (5.9) is noted down once again before substituted to the boundary condition at $r = b$ (5.19).

$$U_\theta(r) = A_1 H_1^{(1)}(\beta r) + A_2 H_1^{(2)}(\beta r)$$

where $A_2 H_1^{(2)}(\beta r)$ and $A_1 H_1^{(1)}(\beta r)$ are the outward- and inward-propagating waves, respectively. Relative to the dashpot, they are the incoming and reflected waves, respectively. The substituted (5.19) gives

$$i\omega c_{dp}\left(A_1 H_1^{(1)}(\beta b) + A_2 H_1^{(2)}(\beta b)\right)$$
$$+G\left(\beta A_1\left(H_0^{(1)}(\beta b) - \frac{H_1^{(1)}(\beta b)}{\beta b}\right) + \beta A_2\left(H_0^{(2)}(\beta b) - \frac{H_1^{(2)}(\beta b)}{\beta b}\right) - \frac{\left(A_1 H_1^{(1)}(\beta b) + A_2 H_1^{(2)}(\beta b)\right)}{b}\right) = 0$$

and can be be rearranged to give the reflected amplitude A_1

$$A_1 = A_2 \frac{-\left(i\omega b c_{dp} H_1^{(2)}(\beta b) - 2G H_1^{(2)}(\beta b) + \beta b G H_0^{(2)}(\beta b)\right)}{i\omega b c_{dp} H_1^{(2)}(\beta b) - 2G H_1^{(2)}(\beta b) + \beta b G H_0^{(2)}(\beta b)} \tag{5.20}$$

The appearance of $i\omega$ only in the first term of the numerator in (5.20) shows that the reflection ratio A_1/A_2 is complex-valued and frequency dependent. To obtain zero amplitude of reflection ($A_1 = 0$), the numerator in (5.20) must be set to zero. This is because the amplitude of the steady state solution is, generally, non-zero ($A_2 \neq 0$), due to non-zero external pressure ($\tau_o \neq 0$) in (5.14) unless it is a trivial solution. Thus the non-reflective condition requires

$$-i\omega b C_{dp} H_1^{(2)}(\beta b) - \beta b G H_0^{(2)}(\beta b) + 2G H_1^{(2)}(\beta b) = 0 \tag{5.21}$$

where the notation with the lower case c_{dp} is replaced by C_{dp*} to emphasize that no reflection is a special case. Therefore, the non-reflective coefficient of dashpot elements C_{dp*} is found as

$$C_{dp*} = \frac{iG\left(\beta b H_0^{(2)}(\beta b) - 2H_1^{(2)}(\beta b)\right)}{\omega b H_1^{(2)}(\beta b)} \tag{5.22}$$

For practical purpose, the Hankel functions in (5.22) may be written in terms of Bessel functions by following (5.10).

$$C_{dp*} = \frac{iG\left((\beta b J_0(\beta b) - iY_0(\beta b)) - 2J_1(\beta b) + 2iY_1(\beta b)\right)}{\omega b\left(J_1(\beta b) - iY_1(\beta b)\right)} \tag{5.23}$$

In the end, the magnitude of the non-reflective elements $|C_{dp}|$ is what matters, so that it can be used both in the case of cosinusoidal and sinusoidal external load. The denominator in (5.23) can be rationalized by multiplying with its complex conjugate. Upon rearranging, the real and imaginary part of (5.10) are found as

$$\begin{aligned} Re\left(C_{dp*}\right) &= \frac{\omega b G J_1(\beta b)\left(\beta b Y_0(\beta b) - 2Y_1(\beta b)\right) - \omega b G Y_1(\beta b)\left(\beta b J_0(\beta b) - 2J_1(\beta b)\right)}{\omega^2 b^2 J_1(\beta b)^2 + \omega^2 b^2 Y_1(\beta b)^2} \\ Im\left(C_{dp*}\right) &= \frac{\omega b G J_1(\beta b)\left(\beta b J_0(\beta b) - 2J_1(\beta b)\right) + \omega b G Y_1(\beta b)\left(\beta b Y_0(\beta b) - 2Y_1(\beta b)\right)}{\omega^2 b^2 J_1(\beta b)^2 + \omega^2 b^2 Y_1(\beta b)^2} \end{aligned} \tag{5.24}$$

Finally, the magnitude of the non-reflective dashpot elements reads

$$|C_{dp}| = \sqrt{Re\left(C_{dp*}\right)^2 + Im\left(C_{dp*}\right)^2} \tag{5.25}$$

Perhaps the most interesting feature of (5.24) is the independence of $|C_{dp}|$ on τ_o, a, and m_p, which seem counter-intuitive at first glance. Note that it is the velocity at the outer boundary that depends on them, hence the total *absorbing force* not its coefficient. Nevertheless, for a given G and ρ, it is dependent on the the radius of the outer boundary $r = b$ and the forcing frequency ω thus the wavenumber β. Two plots in Figure 5.4 are shown, with the controlled variables in Table (5.1), to get insight on the behavior of $|C_{dp}|$. Note that Figure 5.4.a assumes f as an unknown.

c_2	ρ	G	a	f	ω	β
m/s	kg/m^3	N/m^2	m	Hz	rad/s	rad/m
360	2022	262051200	0.5	80	503	1.396

Table 5.1: Material, geometrical, and external load properties for plotting dashpot coeffcient

Figure 5.4.a shows an exponentially decreasing $|C_{dp}|$ with increasing b and an exponentially increasing $|C_{dp}|$ with decreasing ω. For this reason, it is incorrect to use frequency-independent dashpot coefficient in this case. From Figure 5.4.b, which plots $|C_{dp}|$ at $80\,Hz$, it can be concluded that starting from $b = 5\,m$, $|C_{dp}|$ approaches into one value around $7.3 \times 10^5\ Ns/m^3$. Due to this asymptotic behavior, $b = 5\,m$ will be considered as a reference for the Test cases later on.

The dependence on b effectively means that it may be possible to prescribe a damping force to absorb the incoming wave from the monopile at any distance. One may favour the closest distance possible to the monopile when modeling the soil domain in the FE analysis because of the consequence of minimum computation. Theoretically, within one dimensional wave analysis, and the assumptions made in the beginning of the formulation, the viscous elements will work perfectly. This ability breaks down when other cases are considered (Metrikine & Vrouwenvelder, 2021). However, it will lay the foundation for the three-dimensional FE analysis in the later sections.

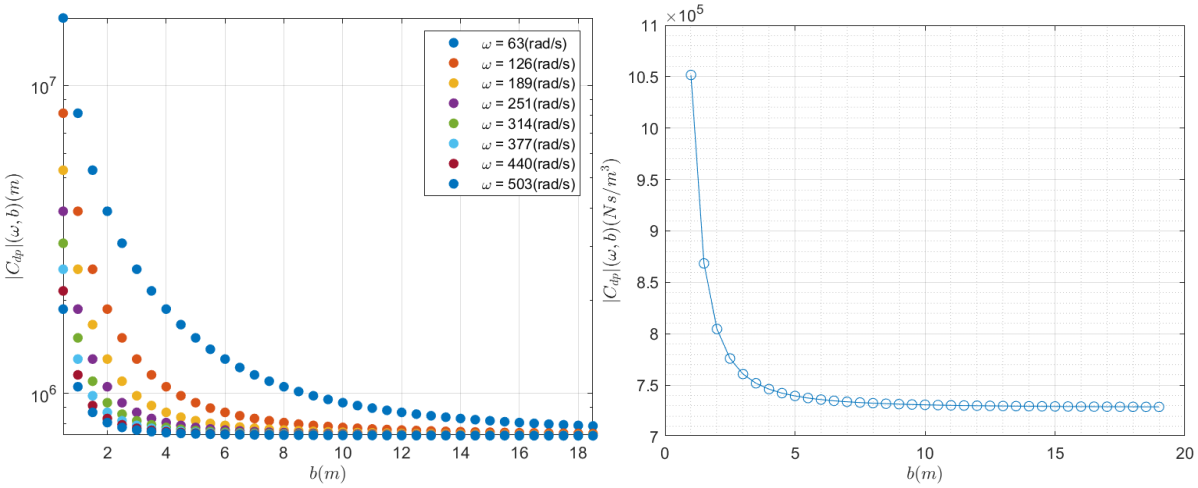

(a) $|C_{dp}|(\omega) - b$ relation for several ω

(b) $|C_{dp}|\left(503\frac{rad}{s}\right) - b$ relation

Figure 5.4: $|C_{dp}|(\omega) - b$ relation

It is observed during the Test cases, which will be discussed in the next sections, that the foregoing non-reflective coefficient is incorrectly formulated [17]. This is shown by comparing the solution to the finite pile-soil-dashpot model with $|C_{dp}|$ versus the solution to the semi-infinite model in one plot. Theoretically, two solutions should be exactly the same, since the nature of the analysis is exact. However, the comparison proves that using $|C_{dp}|$, the finite solution only approximates the semi-infinite solution. The flawed derivation is started when the existence of both the real and imaginary part in (5.21) is overlooked.

[17] (A. Metrikine, personal communication, 20 January, 2023)

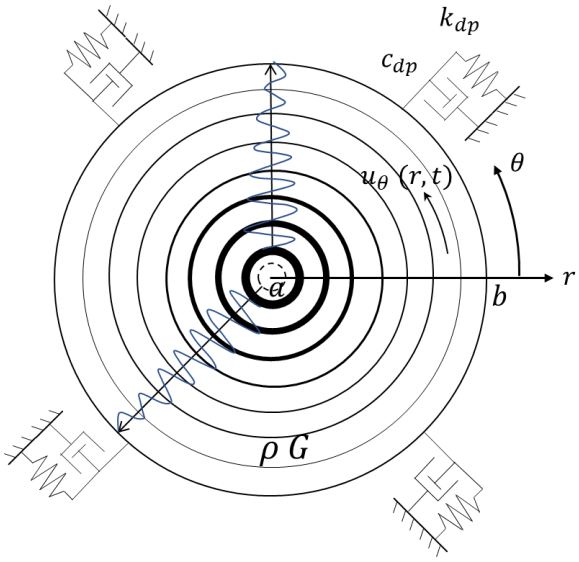

Figure 5.5: Illustration of a steady state torsional wave with the wavefront approaches spring and dashpot elements

The correct approach is to equate each of the real and imaginary part with zero. The real part can be zero if another element such as a spring or mass element is added. Considering an additional spring element k_{dp} at $r = b$, the force equilibrium at $r = b$ (5.17) becomes

$$\left\{k_{dp}u_\theta + c_{dp}\dot{u}_\theta = -\tau_{r\theta}\right\}_{r=b} \tag{5.26}$$

Accordingly, (5.19) should be replaced by

$$\left\{k_{dp}U_\theta + i\omega c_{dp}U_\theta + G\left(\frac{dU_\theta}{dr} - \frac{U_\theta}{r}\right) = 0\right\}_{r=b} \tag{5.27}$$

Thus, the reflected amplitude A_1 (5.20) becomes

$$A_1 = A_2\frac{-\left(bk_{dp}H_1^{(2)}(\beta b) + i\omega bc_{dp}H_1^{(2)}(\beta b) - 2GH_1^{(2)}(\beta b) + \beta bGH_0^{(2)}(\beta b)\right)}{bk_{dp}H_1^{(2)}(\beta b) + i\omega bc_{dp}H_1^{(2)}(\beta b) - 2GH_1^{(2)}(\beta b) + \beta bGH_0^{(2)}(\beta b)} \tag{5.28}$$

Both the real and imaginary part of the numerator in (5.28) must be equal to zero. In terms of Bessel functions

$$\left(-bk_{dp} - i\omega bc_{dp} + 2G\right)\left(J_1(\beta b) - iY_1(\beta b)\right) - \beta bG\left(J_0(\beta b) - iY_0(\beta b)\right) = 0 \tag{5.29}$$

The two unknowns can be solved with the following two equations

$$\left(bk_{dp} - 2G\right)Y_1(\beta b) - \omega bc_{dp}J_1(\beta b) + \beta bGY_0(\beta b) = 0 \tag{5.30}$$

$$\left(-bk_{dp} + 2G\right)J_1(\beta b) - \omega bc_{dp}Y_1(\beta b) - \beta bGJ_0(\beta b) = 0 \tag{5.31}$$

From (5.30) and changing the variables

$$K_{dp} = \frac{bC_{dp}\omega J_1(\beta b) + 2GY_1(\beta b) - \beta bGY_0(\beta b)}{bY_1(\beta b)} \tag{5.32}$$

Substituting (5.32) into (5.31) leads to

$$C_{dp} = -\frac{\beta G\left(J_0(\beta b)Y_1(\beta b) - J_1(\beta b)Y_0(\beta b)\right)}{\omega\left(J_1(\beta b)^2 + Y_1(\beta b)^2\right)} \tag{5.33}$$

Finally, (5.32) becomes

$$K_{dp} = -\frac{G\left(\beta bJ_0(\beta b)J_1(\beta b) + \beta bY_0(\beta b)Y_1(\beta b) - 2J_1(\beta b)^2 - 2Y_1(\beta b)^2\right)}{b\left(J_1(\beta b)^2 + Y_1(\beta b)^2\right)} \tag{5.34}$$

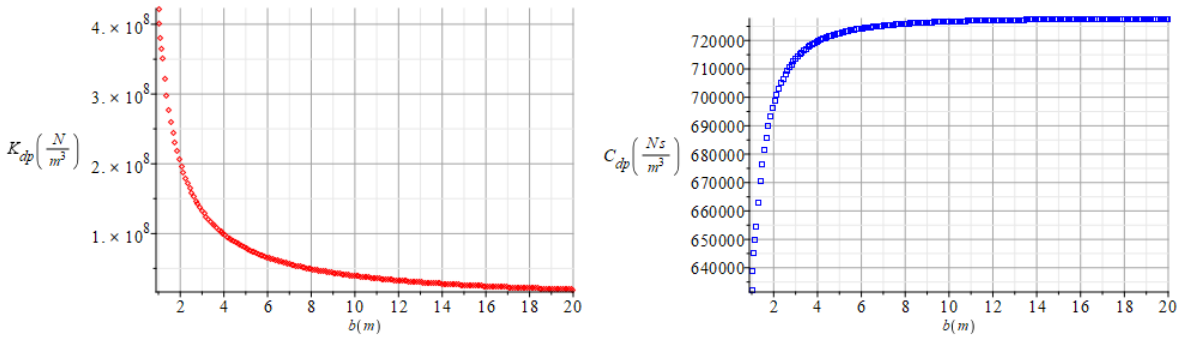

(a) $K_{dp}\left(503\frac{rad}{s}\right) - b$ relation

(b) $C_{dp}\left(503\frac{rad}{s}\right) - b$ relation

Figure 5.6: $K_{dp}(\omega)$ and $C_{dp}(\omega) - b$ relation

As can be seen from Figure 5.6, an exponentially decaying behavior of K_{dp} and a logarithmic behavior of C_{dp} with the increasing b are visible. Figure 5.6.b also demonstrates that the curve approaches a value that is approximately the same order of magnitude compared to $|C_{dp}|$ in Figure 5.4.b. Other than that, the discussion on the derivation of the non-reflective boundary is closed and followed by its usage in the finite domain.

5.3.3. Forced torsional motion in a finite pile-soil-boundary

It is the time to synthesize $|C_{dp}|$ into a finite pile-soil system to see whether its non-reflective behavior works or not. It will be presumed that both A_1 and A_2 are unknowns to examine $|C_{dp}|$ for solving the general case[18] of finite soil bounded by a rigid ring and dashpot elements under the previously established assumptions. To make it brief, the analysis will start from the governing equations in the frequency domain by assuming the same steady state solution in the form $u_\theta(r,t) = Re\big(U_\theta(r)\exp(i\omega t)\big)$. Recall first the equation of motion in the first of (5.18), the boundary condition at $r = a$ in the second of (5.18), and the boundary condition at $r = b$ in (5.19). The general solution to the equation of motion is (5.9).

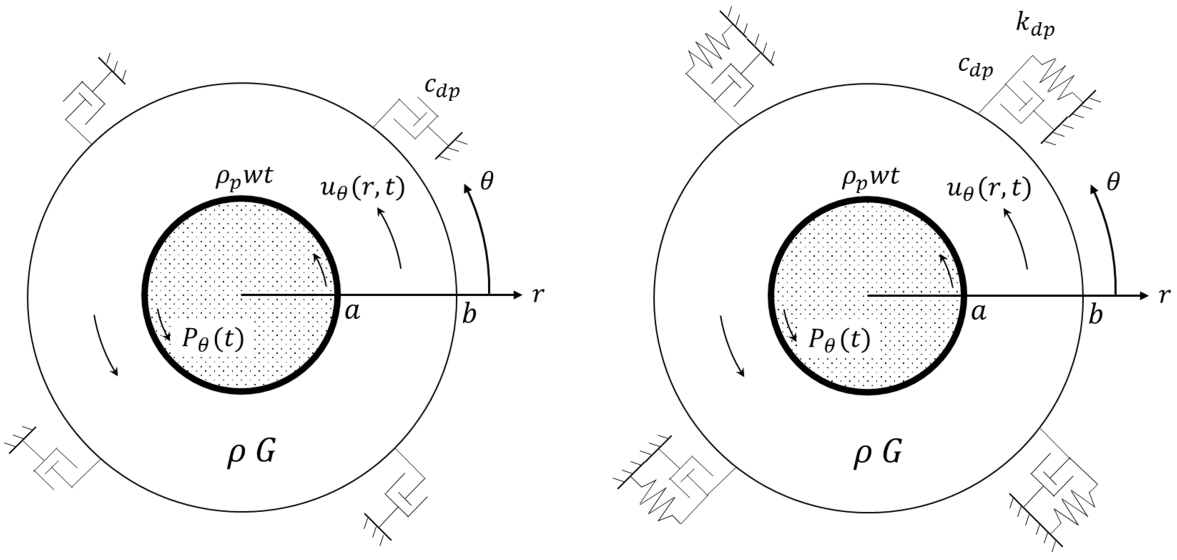

Figure 5.7: Finite model

Having two unknowns and two equation of boundary conditions, the problem is solvable by substi-

[18] General case here means that $|C_{dp}|$ formulation should work for any τ_o, ω, a, b, and material properties defined in Section 5.3.

tuting the general solution into the boundary conditions, which reads

$$\underbrace{\begin{bmatrix} \underbrace{\frac{-\beta aG\left(H_0^{(1)}(\beta a)-\frac{H_1^{(1)}(\beta a)}{\beta a}\right)+\left(-\omega^2 am_p+G\right)H_1^{(1)}(\beta a)}{a}}_{b} & \underbrace{\frac{-\beta aG\left(H_0^{(2)}(\beta a)-\frac{H_1^{(2)}(\beta a)}{\beta a}\right)+\left(-\omega^2 am_p+G\right)H_1^{(2)}(\beta a)}{a}}_{b} \\ \underbrace{\frac{\beta bG\left(H_0^{(1)}(\beta b)-\frac{H_1^{(1)}(\beta b)}{\beta b}\right)+\left(i\omega bc_{dp}-G\right)H_1^{(1)}(\beta b)}{b}}_{} & \underbrace{\frac{\beta bG\left(H_0^{(2)}(\beta b)-\frac{H_1^{(2)}(\beta b)}{\beta b}\right)+\left(i\omega bc_{dp}-G\right)H_1^{(2)}(\beta b)}{b}}_{} \end{bmatrix}}_{\mathbf{M}} \underbrace{\begin{pmatrix} A_1 \\ A_2 \end{pmatrix}}_{\mathbf{u}} = \underbrace{\begin{pmatrix} \tau_o \\ 0 \end{pmatrix}}_{\mathbf{f}} \tag{5.35}$$

For the exact solution where the spring elements are included at the outer boundary, the term $\left(i\omega bc_{dp}-G\right)$ in $\mathbf{M}(2,1)$ and $\mathbf{M}(2,2)$ in (5.35) is replaced by $\left(i\omega bc_{dp}+bk_{dp}-G\right)$.

Additionally, to verify the use of non-reflective boundary, two other problems that use $free$ and $fixed$ outer boundary are formulated. While $free$ boundary means that $\tau_{r\theta}(b,t)=0$, $fixed$ boundary means that $u_\theta(b,t)=0$. For the $free$ boundary, the term $\left(i\omega bc_{dp}-G\right)$ in $\mathbf{M}(2,1)$ and $\mathbf{M}(2,2)$ in (5.35) is replaced by $(-G)$. For the $fixed$ boundary, the whole term in $\mathbf{M}(2,1)$ and $\mathbf{M}(2,2)$ in (5.35) is replaced by $H_1^{(1)}(\beta b)$ and $H_1^{(2)}(\beta b)$, respectively. For each case, the unknown vector $\mathbf{u}$, thus A_1 and A_2, can be found by operating

$$\mathbf{u}=\mathbf{M}^{-1}\mathbf{f} \tag{5.36}$$

Finally, only the real part of $U_\theta(r)\exp(i\omega t)$ is retrieved to obtain the physical displacement quantities.

5.3.4. Test case 0 (TC0): semi-infinite versus finite domain in Maple

Having the solutions for both the semi-infinite pile-soil and pile-soil- non-reflective boundary at hand, three cases of the outer boundary radius b are examined to compare the $u_\theta(r,t)$ against each other in Maple. Note that Test case 1 is run in the time domain with the purpose to check whether the unwanted standing wave field occurs or not. If so, this means that either $|C_{dp}|$ or K_{dp} and C_{dp} or the constants A_1 and A_2 are incorrect. Ideally, the result is checked through an animated plot. On a paper, it will be presented here only at two time moments. For Test case 1, $D_o=1\,m$ is desired to ease the tests. The other geometries are generated from the average ratios based on $Data1$ in Table 2.1.

D_o can be used to measure $L_{\Omega p}$, thus b, which means larger D_o will result in larger radius of the soil domain, thus more computational effort for the FE solver. The measure of $L_{\Omega p}$ may also be associated with the wavelength λ, which can tell how many waves will be captured in the interior domain. The wavelength for $f=80\,Hz$ is approximately $\lambda=c_2/f=4.5\,m$ by assuming a plane shear wave. Suppose $L_{\Omega p}$ is normalized by the wavelength, then it can be of $2\frac{2}{3}\lambda$, λ, and so on. The controlled and independent variables for Test case 1 are tabulated in Table 5.2 and 6.1. The upper limit is chosen as $L_{\Omega p}=12D_o=2\,2/3\lambda$, which is twice the reference discussed in 5.1 to see the effect in a large domain. $b=5\,m$, thus $L_{\Omega p}=4.5D_o=\lambda$, is chosen as the midpoint due to the interest on the asymptotic behavior of $|C_{dp}|$ and C_{dp} shown in Figure 5.4.b. and 5.6.b. The lower limit is taken as half of the midpoint $L_{\Omega p}=2.5D_o=5/9\,\lambda$, to see the effect in a small domain.

c_2	ρ	G	ρ_p	wt	m_p	a	τ_o	f	ω	β
m/s	kg/m^3	N/m^2	kg/m^3	m	kg/m^2	m	Pa	Hz	rad/s	rad/m
360	2022	262051200	7850	0.01	78.5	0.5	40000	80	503	1.396

Table 5.2: Material, geometrical, and external load properties for the Test cases

Notice that the solution to the semi-infinite model is covered by the solution to the finite model that uses K_{dp} and C_{dp}, which explains why only two curves emanate in Figure 5.8. Using $|C_{dp}|$ will slightly overestimate the exact solution, which is shown at $t=0.0035\,s$ in Figure 5.8. In any case, it can be concluded that the coefficient of non-reflective boundary can used to mimic the finite domain as if this was a semi-infinite domain. Also, Figure 5.9 and 5.10 proves that the non-reflective behavior, by using K_{dp} and C_{dp}, is dependent of b. It infers that, in theory, it is not a problem to apply small or large soil domain. Additionally, Figure 5.9.b verifies the occurrence of standing wave field by observing the location of the peak amplitude for both the solution to the $free$ and $fixed$ boundary that are not moving

$L_{\Omega p}$			b	$\lvert C_{dp}\rvert$	K_{dp}	C_{dp}
D_o	λ	m	m	Ns/m^3	N/m^3	Ns/m^3
12	$2\frac{2}{3}$	12	12.5	729719	3.15×10^7	7.27×10^5
4.5	1	4.5	5	734642	7.90×10^7	7.23×10^5
2.5	$\frac{5}{9}$	2.5	3	751691	1.6×10^8	7.08×10^5

Table 5.3: Horizontal extent of the soil domain and the dashpot coefficient

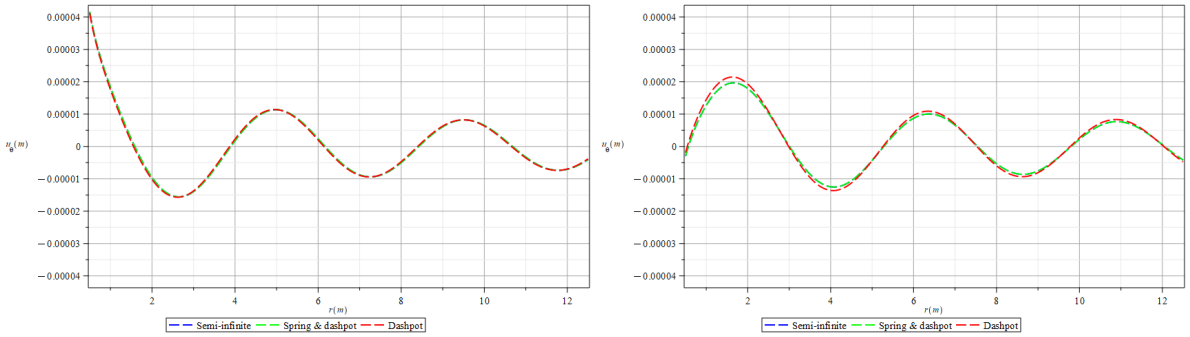

(a) $Re\big(u_\theta(r, 0.0000\,s)\big)\,(m)$ (b) $Re\big(u_\theta(r, 0.0035\,s)\big)\,(m)$

Figure 5.8: Solution to the semi-infinite and finite model for $b = 12.5\,m$

in r at different t. Figure 5.9 and 5.10 proved that at small b, the $free$ boundary approximates the exact solution well but not at large b. The opposite is true for the $fixed$ boundary. On the other hand, the non-reflective boundaries match well with the semi-infinite solution both at small and large b. For these reasons, the non-reflective coefficient will be exploited in the FE model.

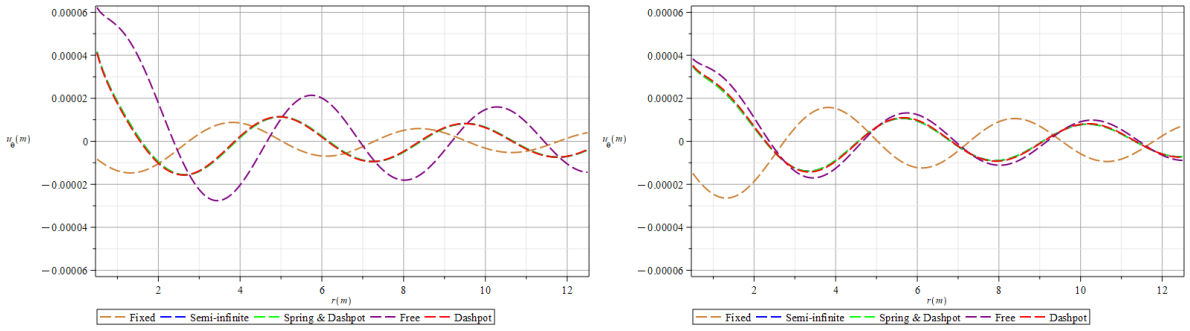

(a) $Re\big(u_\theta(r, 0y.000\,s)\big)\,(m)$ for $b = 12.5\,m$ (b) $Re\big(u_\theta(r, 0.0014\,s)\big)\,(m)$ for $b = 12.5\,m$

Figure 5.9: Significance of the outer boundary at large b

5.4. Damped torsional motion

5.4.1. Forced vibration with a distributed viscous damping in the medium

To make sense the steady state solution and since every engineering system experiences energy dissipation, a form of damping force in the continuum is considered. Among other form of damping, a viscous damping is assumed, which is proportional to the velocity. Unlike the viscous elements in Section 5.1, which acts at the boundary, the following distributed damping acts in the continuum (Metrikine, 2021; Metrikine & Tsouvalas, 2021). When this kind of damping is employed, the model is often called a linear visco-elastic model because the resulting stress-strain relation is linear. For this type of model, Kelvin model is adopted instead of Maxwell model. That is to add dashpots, which

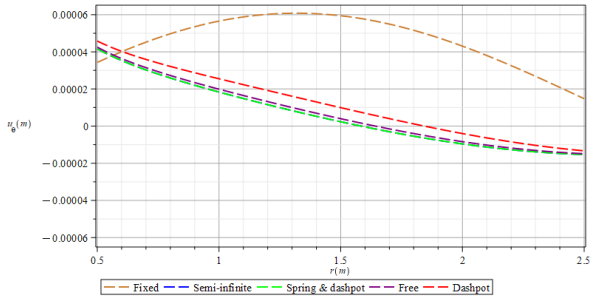

Figure 5.10: Significance of the outer boundary at small b

represents the damping, parallel[19] to the existing springs, which represents the stiffness. In earthquake engineering, the Kelvin model is often generalized in terms of

$$\tau = G\gamma + G'\frac{\partial \gamma}{\partial t} \tag{5.37}$$

where the shear stress τ is composed of the stiffness term $G\gamma$ and the damping term $G'\frac{\partial \gamma}{\partial t}$. γ is the shear strain and G' is called the loss modulus (Ishihara, 1996). In this study, instead of the form in (5.37), the following form of visco-elastic model, in the Cartesian coordinate, will be adopted to ease the mathematical computation.

$$\tau A_o = G\gamma A_o + c_d \frac{\partial u}{\partial t} \tag{5.38}$$

where A_o is the cross-sectional area of a solid element cut and c_d is the distributed damping coefficient. Therefore, from (5.1), the torsional equation of motion subjected to a distributed damping becomes

$$Gr\left(u_\theta'' + \frac{1}{r}u_\theta' - \frac{1}{r^2}u_\theta\right) = \rho\, r\, \ddot{u}_\theta + c_d \dot{u}_\theta, \qquad a < r < \infty \tag{5.39}$$

where the accent $\dot{}$ denotes $\partial/\partial t$. (5.39) can also be written as

$$u_\theta'' + \frac{1}{r}u_\theta' - \frac{1}{r^2}u_\theta = \frac{1}{c_2^2}\ddot{u}_\theta + \frac{2n_d}{c_2^2}\dot{u}_\theta, \qquad 2n_d = \frac{c_d}{\rho r} \tag{5.40}$$

where n_d denotes the damping factor (Metrikine & Tsouvalas, 2021). The initial and boundary conditions in Section (5.3.1) still holds. Following a similar procedure as in Section (5.3.1), the steady state solution is searched for in the form $u_\theta(r,t) = U_\theta(r)\exp(i\omega t)$, which upon substitution into the governing equations, for a periodic solution to exist, (5.40) and (5.2) reads

$$\begin{aligned} U_\theta'' + \frac{1}{r}U_\theta' - \frac{1}{r^2}U_\theta &= \frac{-\omega^2}{c_2^2}U_\theta + \frac{i\omega 2n_d}{c_2^2}U_\theta \\ U_\theta'' + \frac{1}{r}U_\theta' + \left(\beta_d^2 - \frac{1}{r^2}\right)U_\theta &= 0, \qquad \beta_d = \sqrt{\frac{\omega^2 - i\omega 2n_d}{c_2^2}} \end{aligned} \tag{5.41}$$

$$\left\{-\omega^2 m_p U_\theta - G\left(\frac{dU_\theta}{dr} - \frac{U_\theta}{r}\right) = \tau_o\right\}_{r=a} \tag{5.42}$$

Comparing (5.41) with (5.7), it can be seen that these two equations are identical in the form of Bessel equations, except that the wavenumber β_d is now a complex number. Since the equations are similar, a similar general solution should hold but with different wavenumber

$$U_\theta(r) = A_1 H_1^{(1)}(\beta_d r) + A_2 H_1^{(2)}(\beta_d r) \tag{5.43}$$

[19]Maxwell model assumes the spring and dashpot in series.

Likewise, the same technique to satisfy the radiation condition and the boundary condition at $r = a$ (5.42) can be applied as done throughout (5.12) and (5.15). Consequently, one may deduce that the solution is

$$u_\theta(r,t) = Re\left(\frac{\tau_o a}{\left(-a\omega^2 m_p + 2G\right) H_1^{(2)}(\beta_d a) - \beta_d a G H_0^{(2)}(\beta_d a)} H_1^{(2)}(\beta_d r)\, \exp(i\omega t)\right) \tag{5.44}$$

A remark on the physical meaning of (5.44) is that a decaying amplitude of displacement in space will be evident, in addition to the decaying behavior of the undamped cylindrical waves, due to energy dissipation has entered the equation of motion. Mathematically, this is because the i of $i\omega 2n_d$ in (5.41) is multiplied by another i in the Hankel function. One extreme is that the radical $\sqrt{\omega^2 - i\omega 2n_d}$ must be positive, which means a lightly damped system, to adhere to common engineering sense (Metrikine & Tsouvalas, 2021). Otherwise, the soil is too hard to be deformed or the forcing frequency is too small. To this end, the appropriate damping factor is still unknown and subject of discussion in the later sections. Lastly, in the case of incoming damped waves, the coefficient of the non-reflective elements can be recovered by replacing the wavenumber β with the wavenumber that corresponds to the damped waves β_d.

5.5. Calibrating the damping ratio

It is convenient to specify damping in terms of damping ratio ζ. This appears everywhere when discussing a discrete dynamical system subjected to viscous damping. For example, in a single degree of freedom system (SDOF), the damping ratio is usually defined as to scale the damping coefficient with respect to twice the natural frequency. $\zeta > 1$ means that the system is over-damped, which is shown by no oscillation after an imposed initial conditions (*i.e.* initial displacement or velocity or both). $\zeta = 1$ is the limit between an over-damped and lightly-damped system, which is also shown by aperiodic motion or else $\zeta < 1$ where the system oscillates both after an imposed initial conditions. A new problem arose due to the requirement of initial conditions that are not formulated in the beginning of Section 5.3. To facilitate the use of damping ratio in Ansys, firstly, an inspection on the well-known SDOF mass-spring-dashpot system is made (Metrikine & Tsouvalas, 2021).

$$\begin{aligned} &m_o\ddot{x} + c_o\dot{x} + k_o x = F(t) \\ &\ddot{x} + 2n_o\dot{x} + \omega_n^2 x = \frac{F(t)}{m_o}, \qquad 2n_o = \frac{c_o}{m_o}, \quad \omega_n = \sqrt{\frac{k_o}{m_o}} \\ &\ddot{x} + 2\zeta\omega_n\dot{x} + \omega_n^2 x = \frac{F(t)}{m_o}, \qquad \zeta = \frac{c_o}{2\sqrt{k_o m_o}} \end{aligned} \tag{5.45}$$

where m_o, c_o, k_o, and F are an arbitrary mass, damping, spring coefficient, and external force of an SDOF system, respectively. n_o and ω_n is the damping factor and the natural frequency of that system, respectively. From (5.45) and comparison with simulation results, which will be shown later on, a similar notion of the damping ratio for the continuous system discussed in this study can be defined as $2n_d = 2\zeta c_2/r$. So, (5.40) becomes

$$u_\theta'' + \frac{1}{r}u_\theta' - \frac{1}{r^2}u_\theta = \frac{1}{c_2^2}\ddot{u}_\theta + \frac{1}{r}\frac{2\zeta}{c_2}\dot{u}_\theta, \qquad \frac{1}{r}2\zeta c_2 = \frac{c_d}{\rho r} \tag{5.46}$$

This means that β_d in the second of (5.41) is equivalent to

$$\beta_d = \sqrt{\frac{\omega^2 - i\omega 2\zeta c_2/r}{c_2^2}} \tag{5.47}$$

To verify the use of damping ratio in Ansys, a simulation in Ansys is performed and then compared with the solution (5.44) by using the new β_d in (5.47). It is found that the *constant structural damping coefficient* in Ansys is approximately the same with the notion of damping ratio here. This verification is made because Ansys uses several terminologies to define damping.

5.6. Non-reflective coefficient for torsional motion propagating in longitudinal direction

Since the infinite nature of the soil domain also extends in the z-direction, another type of non-reflective boundary should be established. In the same manner with the derivation in Section 5.3.2, the first and foremost is to state the equation of motion, which reads

$$\frac{\partial^2 u_\theta(z_*,t)}{\partial z_*^2} = \frac{1}{c_2^2}\frac{\partial^2 u_\theta(z_*,t)}{\partial t^2} \tag{5.48}$$

as derived in Appendix B.2, where z_* is a new local coordinate that acts in the opposite of z for mathematical convenience to avoid confusion in the formulation of the boundary condition. To find the non-reflective coefficient, viscous elements are first assumed at z_Ω. The boundary condition thus reads

$$\left\{c_{dp,z}\dot{u}_\theta = -\tau_{z\theta}\right\}_{r=z_\Omega} \tag{5.49}$$

Note that the displacement in (5.48) and (5.49) is $u_\theta(z_*,t)$. The steady state solution is searched for in the form of $u_\theta(z_*,t) = \tilde{U}_\theta(z_*)\exp(i\omega t)$. In the frequency domain, (5.48) and (5.49) become

$$\tilde{U}_\theta'' + \beta^2\tilde{U}_\theta = 0, \qquad \beta = \frac{\omega}{c_2} \tag{5.50}$$

$$\left\{i\omega c_{dp,z}\tilde{U}_\theta + G\frac{d\tilde{U}_\theta}{dr} = 0\right\}_{r=z_\Omega} \tag{5.51}$$

The general solution to (5.50) is

$$\tilde{U}_\theta(z_*) = A_3\exp(i\beta z_*) + A_4\exp(-i\beta z_*) \tag{5.52}$$

where A_3 and A_4 are the unknown amplitudes that propagate in negative and positive z_*-direction, respectively. With respect to z_Ω, the reflected wave must be A_3. Substituting (5.52) into (5.51) and solve for A_3 will give

$$A_3 = \frac{A_4\left(\beta G - \omega c_{dp,z}\right)\exp\left(i\beta z_\Omega\right)}{\left(\beta G + \omega c_{dp,z}\right)\exp\left(-i\beta z_\Omega\right)} \tag{5.53}$$

In the same manner with (5.21), the non-reflective coefficient for the torsional wave that propagates in z_*-direction reads

$$C_{dp,z} = \frac{G}{c_2} = \rho c_2 \tag{5.54}$$

This means that (5.54) is constant and the same with the standard LK boundary discussed in Section 5.1.

5.7. Torsional motion of a thin shell on (visco)-elastic elements

As a tool to inspect the simulation result of the pre-stressed harmonic analysis in Section 7.6, an analytical solution considering a forced torsional vibration $u_{\theta,p}(z,t)$ of a monopile, represented by a thin shell, in the longitudinal direction seems useful. It is because the equation of motion of an axisymmetric torsion of a circular cylindrical thin shell is independent of the radial and longitudinal motion as can be seen in the second of (2.2), ergo a simplified derivation can be proposed. A 1D axisymmetric torsional problem will be very likely to be able to represent the 3D FE problem in this case. Following Winkler foundation concept with a distributed viscous damping as introduced in Section 5.5, a parallel springs and dashpots can represent the soil reaction along the embedded pile shaft. The model will assume no damping in the monopile for simplicity. Assuming an undamped steel and a harmonic load in a cosine

form at the pile top with force amplitude over the pile perimeter $F_\theta(t) = \frac{f_o}{p_p}\cos(\omega t)$, the governing equations of $u_{\theta,p}(z,t)$ reads

$$\frac{1}{c_{2,p}^2}u_{\theta,p,1,tt} - u_{\theta,p,1,zz} = 0, \qquad z_{bed} < z < z_{top} \tag{5.55}$$

$$\frac{1}{c_{2,p}^2}u_{\theta,p,2,tt} - u_{\theta,p,2,zz} + \frac{\zeta_o}{c_{2,p}^2}u_{\theta,p,2,t} + \frac{\alpha z}{c_{2,p}^2}u_{\theta,p,2} = 0, \qquad z_{tip} < z < z_{bed} \tag{5.56}$$

$$\left\{G_p\, wt\, u_{\theta,p,1,z} + F_\theta(t) = 0\right\}_{z_{top}} \tag{5.57}$$

$$\left\{u_{\theta,p,2,z} = 0\right\}_{z_{tip}} \tag{5.58}$$

$$\left\{u_{\theta,p,2} - u_{\theta,p,1} = 0\right\}_{z_{bed}} \tag{5.59}$$

$$\left\{u_{\theta,p,2,z} - u_{\theta,p,1,z} = 0\right\}_{z_{bed}} \tag{5.60}$$

where $G_p\, wt = K_p\frac{(1-\nu_p)}{2}$ is used to modify the stiffness term in the second of (2.2). While the subscript $_p$ denotes the pile, 1 and 2 means the first and second segment of the pile that is above and below the soil surface, respectively. The subscripts $_t$ and $_z$ denote the time and spatial derivative, respectively. $\zeta_o = \frac{2\zeta c_2}{R_p} = \frac{c_d}{\rho_p wt}$ and $\alpha = \frac{k_\theta}{\rho_p wt}$. $k_\theta = 2G$ modifies the spring coefficient originated by Randolph for the torque-rotation $T-\theta$ relationship of a rigid pile with the embedded length P_p and reads $k_{\theta,R} = T/\theta = 4\pi R_p^2 G P_p$, which is utilized in experiments by other researchers (Georgiadis & Saflekou, 1990). Note that the modification assumes small angle approximation (*i.e* $\theta \approx u_\theta/R_p$) Notice that the embedded length P_p as a constant is replaced by z to approximate a linearly increasing soil stiffness.

Having four boundary/interface conditions for two second order PDE, the mathematical statement is well-posed for the steady state condition. Aiming for the transfer function (TF) or amplitude-frequency response function (A-FRF) or the response amplitude operator (RAO) along the pile $\left|\tilde{u}_{\theta,p}(z,\xi)/\tilde{F}_\theta(\xi)\right|$, the governing equations in the frequency domain can be obtained through the following Fourier transform

$$\begin{aligned}\tilde{u}_{\theta,p}(\xi) &= \int_{-\infty}^{\infty} u_{\theta,p}(t)\exp(-i\xi t)\,dt \\ u_{\theta,p}(t) &= \frac{1}{2\pi}\int_{-\infty}^{\infty}\tilde{u}_{\theta,p}(\xi)\exp(i\xi t)\,d\xi\end{aligned} \tag{5.61}$$

where $\xi = 2\pi f$. Consequently,

$$\tilde{u}_{\theta,p,1,zz}(z,\xi) + \beta_p\tilde{u}_{\theta,p,1}(z,\xi) = 0, \qquad \beta_p = \frac{\xi}{c_{2,p}}, \qquad z_{bed} < z < z_{top} \tag{5.62}$$

$$\tilde{u}_{\theta,p,2,zz}(z,\xi) + \frac{\Lambda}{c_{2,p}^2}\tilde{u}_{\theta,p,2}(z,\xi) = 0, \qquad \Lambda = i\zeta_o\xi + \alpha\, z - \xi^2, \qquad z_{tip} < z < z_{bed} \tag{5.63}$$

$$\tilde{F}_\theta(\xi) = f_o/p_p\pi\big(\delta(-\xi+\omega) + \delta(\xi+\omega)\big) \tag{5.64}$$

$$\left\{G_p\, wt\, \tilde{u}_{\theta,p,1,z}(z,\xi) + \tilde{F}_\theta(\xi) = 0\right\}_{z_{top}} \tag{5.65}$$

$$\left\{\tilde{u}_{\theta,p,2,z}(z,\xi) = 0\right\}_{z_{tip}} \tag{5.66}$$

$$\left\{\tilde{u}_{\theta,p,2}(z,\xi) - \tilde{u}_{\theta,p,1}(z,\xi) = 0\right\}_{z_{bed}} \tag{5.67}$$

$$\left\{\tilde{u}_{\theta,p,2,z}(z,\xi) - \tilde{u}_{\theta,p,1,z}(z,\xi) = 0\right\}_{z_{bed}} \tag{5.68}$$

where $\delta()$ is the Dirac delta function. With the help of Maple, the general solution to the ODE (5.62) and Airy DE (5.63) reads

$$\tilde{u}_{\theta,p,1}(z,\xi) = \tilde{U}_1(\xi)\exp(i\beta_p z) + \tilde{U}_2(\xi)\exp(-i\beta_p z) \tag{5.69}$$

$$\tilde{u}_{\theta,p,2}(z,\xi) = \tilde{U}_3(\xi)Ai\big(-\alpha_o\Lambda(z)/\alpha\big) + \tilde{U}_4(\xi)Bi\big(-\alpha_o\Lambda(z)/\alpha\big), \qquad \alpha_o = \left(\frac{-\alpha}{c_{2,p}^2}\right)^{1/3} \tag{5.70}$$

where Ai and Bi are Airy wave functions that satisfy the Airy differential equation. Ai and Bi are first checked in Maple to ensure which one produces the downward and upward propagating waves in Maple by introducing a much higher frequency than $80\,Hz$, though in this particular problem the check is not so important due to the summation of both the downward and upward propagating waves as the problem is bounded at the two ends.

Substituting the general solution $\tilde{u}_{\theta,p,1}(z,\xi)$ and $\tilde{u}_{\theta,p,2}(z,\xi)$ into (5.65), (5.66), (5.67), and (5.68) yields the following matrix form

$$\underbrace{\begin{bmatrix} i\beta_p G_p\, wt\exp(i\beta_p z_{top}) & -i\beta_p G_p\, wt\exp(-i\beta_p z_{top}) & 0 & 0 \\ 0 & 0 & \frac{d}{dz}\left(Ai\left(-\frac{\alpha_o}{\alpha}\Lambda(z_{tip})\right)\right) & \frac{d}{dz}\left(Bi\left(-\frac{\alpha_o}{\alpha}\Lambda(z_{tip})\right)\right) \\ -i\beta_p\exp(i\beta_p z_{bed}) & i\beta_p\exp(-i\beta_p z_{bed}) & \frac{d}{dz}\left(Ai\left(-\frac{\alpha_o}{\alpha}\Lambda(z_{bed})\right)\right) & \frac{d}{dz}\left(Bi\left(-\frac{\alpha_o}{\alpha}\Lambda(z_{bed})\right)\right) \\ -\exp(i\beta_p z_{bed}) & -\exp(-i\beta_p z_{bed}) & Ai\left(-\frac{\alpha_o}{\alpha}\Lambda(z_{bed})\right) & Bi\left(-\frac{\alpha_o}{\alpha}\Lambda(z_{bed})/\right) \end{bmatrix}}_{\mathbf{M_p}} \underbrace{\begin{pmatrix} \tilde{U}_1 \\ \tilde{U}_2 \\ \tilde{U}_3 \\ \tilde{U}_4 \end{pmatrix}}_{\mathbf{u_p}}$$

$$= \underbrace{\begin{pmatrix} -f_o/p_p\pi\big(\delta(-\xi+\omega)+\delta(\xi+\omega)\big) \\ 0 \\ 0 \\ 0 \end{pmatrix}}_{\mathbf{f_p}} \tag{5.71}$$

the unknown vector $\mathbf{u_p}$, thus $\tilde{U}_1$, $\tilde{U}_2$, $\tilde{U}_3$, and $\tilde{U}_4$, can be found by evaluating

$$\mathbf{u_p} = \mathbf{M_p}^{-1}\mathbf{f_p} \tag{5.72}$$

If one focuses on the shear stress only, the transfer function of the shear stress above the soil surface $H_{1,\tau}(z,\xi)$ and below the soil surface $H_{2,\tau}(z,\xi)$ read

$$\begin{aligned} H_{1,\tau}(z,\xi) &= G_p\left|\frac{\tilde{u}_{\theta,p,1,z}(z,\xi)}{\tilde{F}_\theta(\xi)}\right| \\ H_{2,\tau}(z,\xi) &= G_p\left|\frac{\tilde{u}_{\theta,p,2,z}(z,\xi)}{\tilde{F}_\theta(\xi)}\right| \end{aligned} \tag{5.73}$$

Accordingly, the amplitude of the shear stress in the frequency domain along the monopile reads

$$|\tau_{z\theta}(z,\xi)| = \big(H_{1,\tau}(z,\xi)\left(H(z-z_{tip}) - H(z-z_{bed})\right) + H_{2,\tau}(z,\xi)\left(H(z-z_{bed}) - H(z-z_{top})\right)\big)\frac{f_o}{p_p} \tag{5.74}$$

where $H()$ is the Heaviside step function.

Correction on the spring elements and simplifying the model

It is found during the analysis that the linearly increasing stiffness of the soil is not correctly formulated proven by the inconsistent unit compared to the mass and stiffness term of the pile. Therefore, a correction is made by using a more simplified spring elements through constant coefficient and that the soil damping is neglected for simplicity. Accordingly, (5.56) is replaced by

$$\frac{1}{c_{2,p}^2}u_{\theta,p,2,tt} - u_{\theta,p,2,zz} + \frac{\alpha}{c_{2,p}^2}u_{\theta,p,2} = 0, \qquad z_{tip} < z < z_{bed} \tag{5.75}$$

where $\alpha = \frac{k_\theta}{\rho_p wt}$. $k_\theta = 2G/R_p$. Additionally, the reaction of the soil at the pile tip is now considered. The spring at the bottom helps to achieve a somewhat stable solution during the evaluation of a convergence problem later on. Therefore, (5.58) becomes

$$\left\{-G_p\, wt\, u_{\theta,p,2,z} = k_\theta\, wt\, u_{\theta,p,2}\right\}_{z_{tip}} \tag{5.76}$$

Following the Fourier transform, Λ in (5.63) is replaced by $\Lambda = -\alpha + \xi^2$. The inverse problem in (5.71) is then replaced by

$$\underbrace{\begin{bmatrix} i\beta_p G_p\, wt \exp(i\beta_p z_{top}) & -i\beta_p G_p\, wt \exp(-i\beta_p z_{top}) & 0 & 0 \\ 0 & 0 & -\left(i\Lambda G_p + k_\theta\right)\exp(i\Lambda z_{tip}) & -\left(i\Lambda G_p + k_\theta\right)\exp(-i\Lambda z_{tip}) \\ -i\beta_p \exp(i\beta_p z_{bed}) & i\beta_p \exp(-i\beta_p z_{bed}) & i\Lambda \exp(i\Lambda z_{bed}) & -i\Lambda \exp(-i\Lambda z_{bed}) \\ -\exp(i\beta_p z_{bed}) & -\exp(-i\beta_p z_{bed}) & \exp(i\Lambda z_{bed}) & \exp(-i\Lambda z_{bed}) \end{bmatrix}}_{\mathbf{M_p}} \underbrace{\begin{pmatrix} \tilde{U}_1 \\ \tilde{U}_2 \\ \tilde{U}_3 \\ \tilde{U}_4 \end{pmatrix}}_{\mathbf{u_p}}$$

$$= \underbrace{\begin{pmatrix} -f_o/p_p \pi\left(\delta(-\xi+\omega) + \delta(\xi+\omega)\right) \\ 0 \\ 0 \\ 0 \end{pmatrix}}_{\mathbf{f_p}} \tag{5.77}$$

Finally, the transfer function of the shear stress can be found by following the same procedure as in the previous analysis.

6

2D FE modeling, result, and discussion

6.1. Modeling under plane strain assumption

Figure 6.1: Workflow in Ansys

A typical workflow to perform a FE analysis in Ansys is shown in Figure 6.1. Important steps to be taken are explained for each step, where pitfalls are experienced. It is best to model the system in the global x-y plane for 2D plane strain analysis. In other words, the dimension in z-axis is assumed to be infinitely long. The monopile thickness must be modeled geometrically at this stage. Otherwise, a profile with a cross-section perpendicular to the x-y plane should be assigned, which is incorrect. Even though material libraries are available, customized material properties are created to ensure that only the properties that belong to the assumption of isotropic elastic material are put. The homogeneous and linear assumptions are implemented by assigning a single material property to the corresponding geometrical properties of the pile-soil system and by turning off the non-linear effects. It is important to create a new cylindrical coordinate system so that the new x-y-z coordinate is equivalent to r-θ-z to ensure that the torsional loading is applied correctly. The cylindrical coordinate system will also alleviate the difficulty during the post-processing as the desired results can be set directly in the θ-direction.

The boundary or interface conditions are defined in the Connection and Harmonic Response. The first includes the contact between the interfaces and the application of the spring element. As introduced in Section 5.2, a bonded connection is set at the pile-soil interface. A large initial gap or penetration should be avoided to minimize inaccuracies, which is usually done by iteration of the meshing. When defining the contact, exploiting the so-called *named selection* is beneficial so that one may not repetitively define the contact through *geometrical selection*. Under the spring element, the non-reflective coefficient is applied as a *longitudinal stiffness* and *longitudinal damping* with *rigid* behavior. The rigid behavior is set to ensure that the spring gives reaction force. Currently, the longitudinal spring element cannot be applied as if it acted in the θ-direction. Despite this limitation, the Test case will show that the results approximate well the exact solution.

As guided by Section 5.3.2, a key important step is defining the correct coefficient. Since the element acts only at one degree of freedom, the coefficient found in the analytical computation shall be integrated along the perimeter. It shall be modeled symmetrically to obtain a symmetric solution. The spring element must be modeled continuously along the perimeter to get an axisymmetric problem as in the analytical model. However, it is not done due to practical implementation because it requires a uniform mesh in the θ and z-direction, which is impossible due to the use of tetrahedral mesh. If one uses hexahedral mesh to overcome this problem, another problem appears in the meshing around the

pile-soil interface (*i.e.* the difficulty of hexahedral mesh to fill a cylindrical shape), which is not desired because it is the location where the interests are focused. It is found that applying four spring elements in symmetry yields a relatively good result even though the reflection is expected due to imperfect modeling. The use of non-reflective elements through this spring element is seldom discussed in the Ansys forum. It is possible that a better way of implementing the spring element as a non-reflective boundary exists.

Most of the simulations in this study are performed in the Harmonic Response toolbox to obtain the steady-state solution. With harmonic analysis, the meshing will be only in space. The meshing size should satisfy the criteria discussed in Section 5.1. In 2D, the meshing process is straightforward, especially when assuring conformity at the pile-soil interface. Nonetheless, an output called *total deformation* must be checked to ensure that no stress concentration occurs at the pile-soil interface, which means that both the meshing criteria and the conformity are met. An automatic linear meshing generates a hexahedral mesh with mid-side nodes by default. Mid-side node is one of the most important features in meshing with linear elements to ensure better accuracy than without it.

The remaining task for the modeling is to apply the harmonic load. Since any load input defined under the Harmonic Response toolbox will be assumed to be a harmonic load, the effect of gravity must be defined separately and done in the Static Structural toolbox. Finally, the load components must be carefully assigned to act in the θ-direction through cylindrical coordinates. At this point, a fictitious[1] force that is uniformly distributed along the monopile perimeter at the pile-soil interface is applied. When post-processing the result, the amplitude and phase response are used with the interpretation as introduced in Section 4.1. Due to axisymmetric assumption, it seems sufficient to sample the displacement amplitude $|U_\theta(r)|\,(m)$ or stress field $|\tau_{r\theta}(r)|\,(Pa)$ along a *path*. In this case, evaluating the solution along a path from $r = a$ to $r = b$ will be the best option rather than looking at the result of the *contour plot*. In spite of taking a little bit more effort to process the data, the result is considered the most relevant. On the contrary, the contour plot seems obvious at first glance, but it is more difficult to interpret the deformation data from the *contour legend*.

6.2. Summary of the test cases

To see the bigger picture and to navigate the scheme, an illustration through Figure 6.2 is made. It shows that the soil geometry is built up in Ansys from the simplest model at TC1 up to the most complicated model at TC6. The end goal is to minimize the error of the final simulation, on which no validated analytical solution is yet available. At each test case, a verification is performed to get one or some conclusions that are used to evolve the model. The conclusion is taken by measuring the average of the relative error $\bar{\epsilon}$ and the correlation coefficient r_c. To this end, the maximum relative error $\bar{\epsilon}_{r,max}$ is not definitive. Instead, the conclusion is deduced in relative to the other results in the same plot.

6.3. TC1: verifying the non-reflective coefficient and damping ratio

TC1 is aimed to evaluate the interpretation of the amplitude and phase response in Ansys harmonic analysis introduced in Section 4.1, the application of the non-reflective coefficient, and to calibrate the use of the damping ratio in Ansys by looking at the undamped motion. Since the amplitude will be revealed simultaneously with the last two, the phase response will be discussed after the second one. The discussion on the non-reflective problem is made by comparing the results that use kinematic boundaries and also the LK boundary with the exact solution. The second goal is achieved by considering three figures in Figure 6.3, 6.4, and 6.5. Together with Table 6.2, 6.3, 6.4, and 6.5, the evaluation can be made quantitatively. Each figure compares the displacement and the shear stress along the sampling points. $b = 12.5\,m$, $b = 5\,m$, and $b = 2.5\,m$ are assumed as the large, medium, and small soil domain. To get confidence on the obtained results, a fine mesh size of $\Delta l = 0.1\,m$ is used.

Significance of the non-reflective boundary

[1] It is fictitious because the force at the pile-soil interface is the one that is unknown and is to be found. However, it is assumed that this force is known for the test cases. By means of this assumption, the theoretical equilibrium force can be checked due to dynamic boundary conditions at the pile-soil interface.

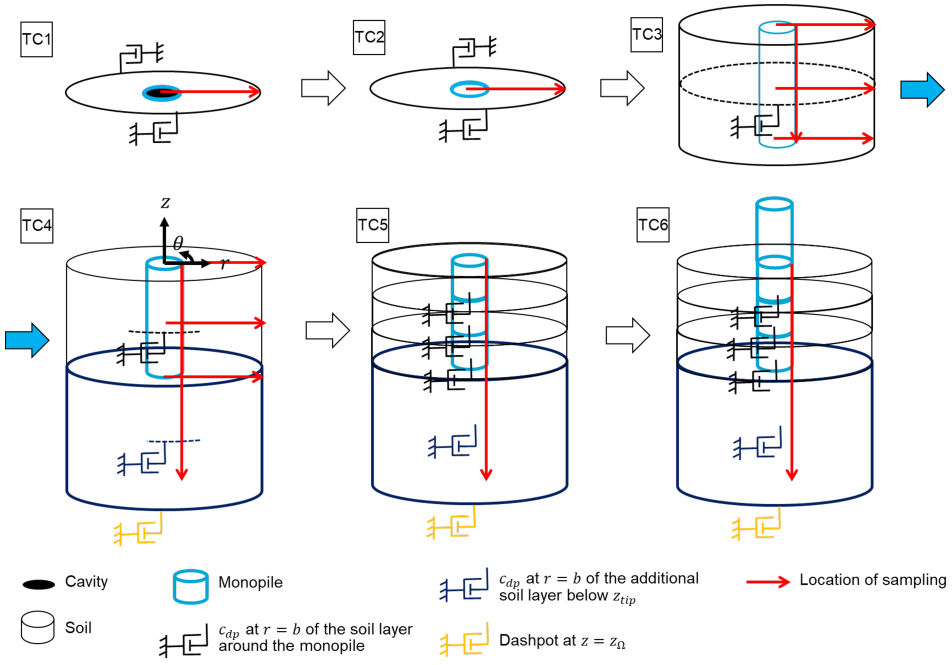

Figure 6.2: Summary of the test cases

$L_{\Omega p}$			b	K_{dp}		C_{dp}		LK_{dp}	
D_o	λ	m	m	N/m^3	N/m	Ns/m^3	Ns/m	Ns/m^3	Ns/m
12	$2\frac{2}{3}$	12	12.5	3.15×10^7	6.18×10^8	7.27×10^5	1.43×10^7	7.27×10^5	5.71×10^7
4.5	1	4.5	5	7.90×10^7	6.21×10^8	7.23×10^5	5.68×10^6	7.27×10^5	2.28×10^7
2.5	$\frac{5}{9}$	2	2.5	1.6×10^8	6.29×10^8	7.08×10^5	2.78×10^6	7.27×10^5	1.14×10^7

Table 6.1: Horizontal extent of the soil domain, the non-reflective coefficient, and the mesh size

From Figure 6.5, the application of K_{dp} and C_{dp} in the FE model matches the exact solution. Nevertheless, its error increases with b, which can be attributed to the fact that the the spring elements are assigned imperfectly as introduced in Section 6.1. Despite of this limitation, the assignment of four spring elements seems fine with the following considerations. The mean of the mean relative error $\bar{\bar{\epsilon}}_r$ in Table 6.2 and 6.3 show that all of the finite model contain error. Considering both $\bar{\bar{\epsilon}}_r$ and $\sigma_{\bar{\epsilon}_r}$, using non-reflective coefficient will be the best option. It is found that at this frequency, the frequency-independent LK boundary gives almost identical solution to the model that uses K_{dp} and C_{dp}.

On the other hand, finite model using $free$ and $fixed$ boundary lead to larger error, where the latter being the worst. Looking at Table 6.4 and 6.5, the same trend can be observed where the non-reflective correlate well to the exact solution. Additionally, $free$ boundary also displays a good correlation to the exact solution. The negation is true when using the $fixed$ boundary, which is somehow cluttered with the negative correlation at $b = 5\,m$. The measure of $\bar{r}_c$ and σ_{r_c} confirm that the non-reflective boundary excel the $free$ boundary. Even though using either the frequency- dependent or independent coefficient seems fine at frequency $80\,Hz$, it is decided to continue the simulation only with the frequency-dependent one due to its frequency-dependent nature as introduced in Section 5.3.4. Since the the non-reflective behavior is independent of b (*i.e.* the domain size) discussed in Section 5.3.4, a moderate choice is taken by implementing $b = 5\,m$ for the next simulation. Moreover, the simulation from this point forward will focus only on the shear stress because of the interest on the shear stress at failure.

Amplitude and phase response

Figure 6.6.a illustrates that the there is a deviation between the amplitude $|(U_\theta(r)|$ of the exact solution and the FE analysis even though the maximum amplitude is in good agreement. This can be

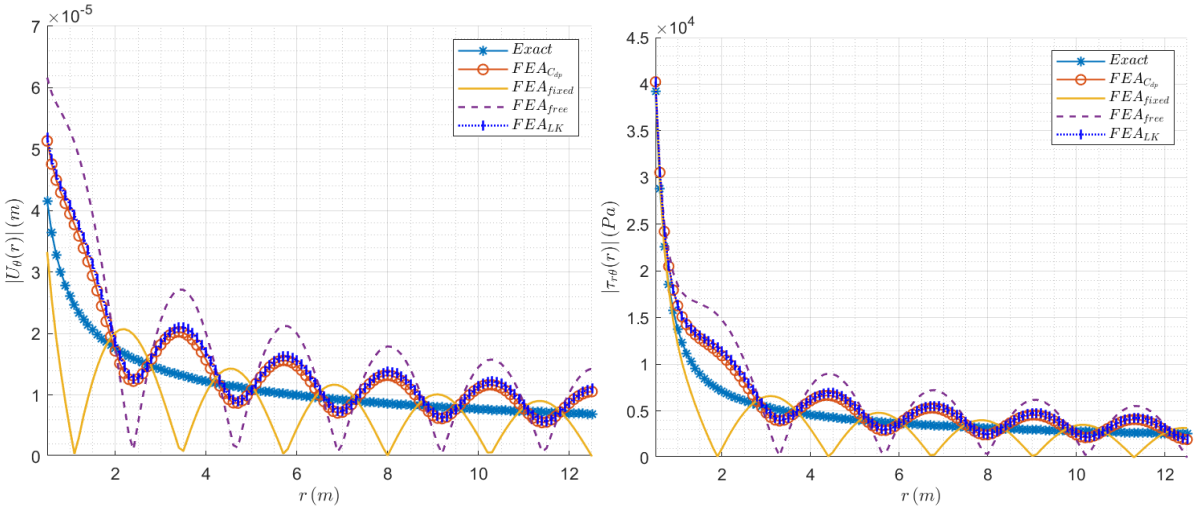

(a) $|(U_\theta(r)|\,(m)$ for different outer boundary conditions (b) $|\tau_{r\theta}(r)|\,(Pa)$ for different outer boundary conditions

Figure 6.3: Significance of outer boundary conditions for $b = 12.5\,m$

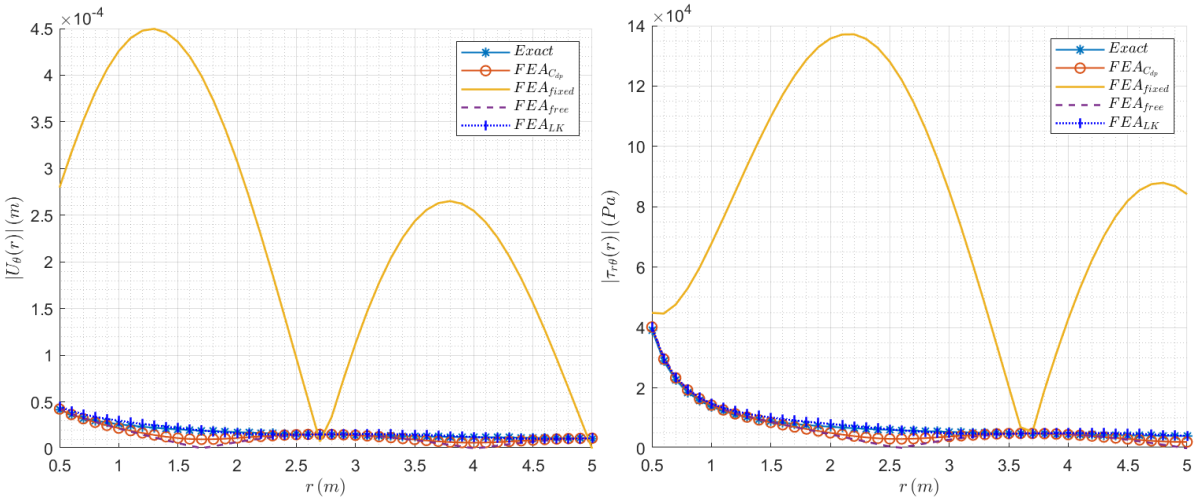

(a) $|(U_\theta(r)|\,(m)$ for different outer boundary conditions (b) $|\tau_{r\theta}(r)|\,(Pa)$ for different outer boundary conditions

Figure 6.4: Significance of outer boundary conditions for $b = 5\,m$

$L_{\Omega p}$		$\bar{\epsilon}_r K_{dp}\&C_{dp}$	$\bar{\epsilon}_r Fixed$	$\bar{\epsilon}_r Free$	$\bar{\epsilon}_r LK_{dp}$
D_o	λ	–	–	–	–
12	$2\frac{2}{3}$	0.29	0.35	0.65	0.32
4.5	1	0.22	12.87	0.35	0.07
2.5	$\frac{5}{9}$	0.03	1.31	0.40	0.15
$\bar{\bar{\epsilon}}_r$		0.18	4.84	0.47	0.18
$\sigma_{\bar{\epsilon}_r}$		0.13	6.97	0.16	0.13

Table 6.2: Error in the displacement

attributed to the presence of damping term $i\Omega\mathbf{C}$ in the formulation of equation of motion, as introduced in Section 4.1, despite of nil percent damping is assigned. A question must be asked based on Figure 6.6.a where the sign of the imaginary parts oppose each other, which is not the case for the real part. The pair of wave function from Ansys resembles the Hankel function $H_1^{(1)}(\beta r)$ and not yet understood fully why this is the case. It can be the indication of imperfect assignment of spring element that

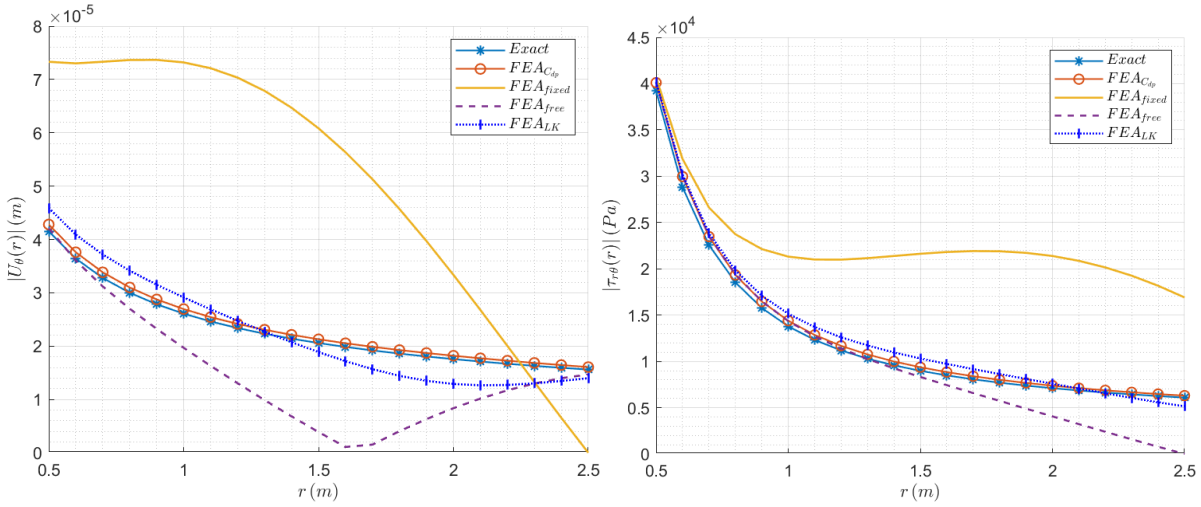

(a) $|(U_\theta(r)|\,(m)$ for different outer boundary conditions

(b) $|\tau_{r\theta}(r)|\,(Pa)$ for different outer boundary conditions

Figure 6.5: Significance of outer boundary conditions for $b = 2.5\,m$

$L_{\Omega p}$		$\bar{\epsilon}_r K_{dp}\&C_{dp}$	$\bar{\epsilon}_r Fixed$	$\bar{\epsilon}_r Free$	$\bar{\epsilon}_r LK_{dp}$
D_o	λ	–	–	–	–
12	$2\frac{2}{3}$	0.28	0.34	0.63	0.31
4.5	1	0.19	11.87	0.30	0.08
2.5	$\frac{5}{9}$	0.04	1.22	0.26	0.09
$\bar{\bar{\epsilon}}_r$		0.17	4.48	0.40	0.16
$\sigma_{\bar{\epsilon}_r}$		0.12	6.42	0.20	0.13

Table 6.3: Error in the shear stress

$L_{\Omega p}$		$r_c K_{dp}\&C_{dp}$	$r_c Fixed$	$r_c Free$	$r_c LK_{dp}$
D_o	λ	–	–	–	–
12	$2\frac{2}{3}$	0.94	0.56	0.84	0.93
4.5	1	0.92	−0.59	0.81	0.99
2.5	$\frac{5}{9}$	0.99	0.75	0.87	0.99
$\bar{r_c}$		0.95	0.63	0.84	0.97
σ_{r_c}		0.04	0.10	0.03	0.03

Table 6.4: Correlation of the displacement

$L_{\Omega p}$		$r_c K_{dp}\&C_{dp}$	$r_c Fixed$	$r_c Free$	$r_c LK_{dp}$
D_o	λ	–	–	–	–
12	$2\frac{2}{3}$	0.97	0.93	0.90	0.97
4.5	1	0.99	−0.17	0.98	0.99
2.5	$\frac{5}{9}$	0.99	0.95	0.98	0.99
$\bar{r_c}$		0.98	0.57	0.95	0.98
σ_{r_c}		0.01	0.64	0.05	0.01

Table 6.5: Correlation of the shear stress

makes the pile-soil far than an axisymmetric problem. The flipped sign of the imaginary part leads to a reversed phase response Φ in Figure 6.6.b. Nevertheless, since $\cos(\Phi)$ for both the analytical and FE solution returns approximately the same values, as shown in Figure 6.6.b, the assumed load in a cosine form, that is concluded in Section 4.1, is adequate together with the corresponding amplitude.

Another takeaway from the phase response in 6.6.b is that the motion delay in the proximity of the pile-soil interface, with the assumed parameters, is small with respect to the force.

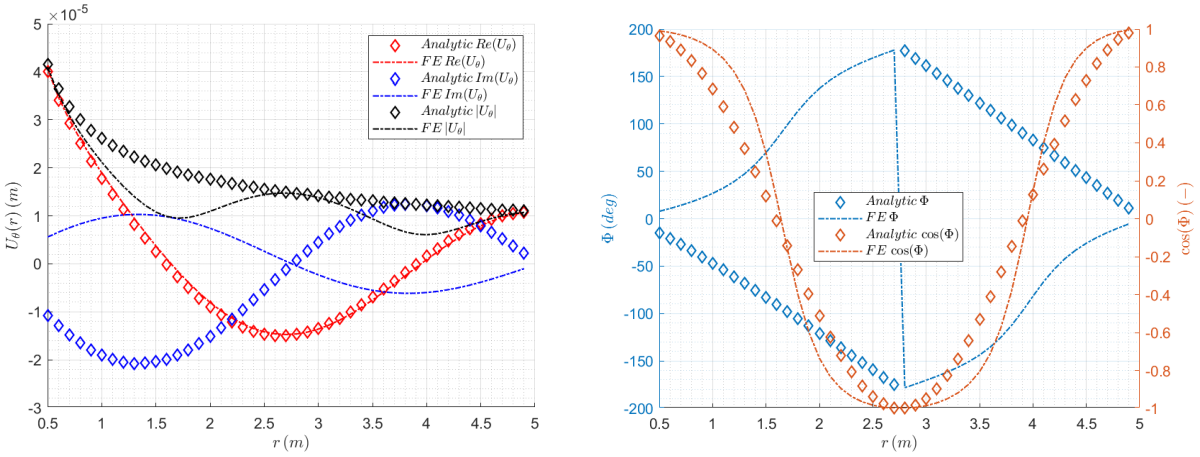

(a) $|(U_\theta(r)|\,(m)$ for $b = 5\,m$

(b) $\Phi(r)\,(^\circ)$ and $\cos(\Phi)(r)$ for $b = 5\,m$

Figure 6.6: Comparison of the displacement amplitude and phase response

Calibration of the damping ratio

Three cases of damping ratio $\zeta < 1$, $\zeta = 1$, and $\zeta > 1$ are depicted in Figure 6.7. The same numerical input is fed into Ansys as the constant structural damping coefficient. Figure 6.7 verifies that the decaying behavior due to the increasing damping ratio in the continuum is apparent. Also, the previously distorted graph in Figure 6.4 due to the solution to the $fixed$ boundary is now becoming vivid. Table 6.6 shows that even though the error increases with the damping ratio, the correlation is very good. The increasing error with the damping ratio means that there can be neglected terms in the assumed damping force in Section 5.4.1. Nonetheless, since damping ratio in engineering system is usually small, especially when linearity is assumed such as between $\zeta = 1\%$ to $\zeta = 5\%$ (S.S. Gómez, personal communication, 9 January, 2023), the assumed form of damping seems not a big problem if one look at the graph for $\zeta = 0$ and $\zeta = 0.25$. Furthermore, the agreement is sound around the pile-soil interface between $r = 0.5\,m$ and $r = 1\,m$. Therefore, by assuming small damping ratio and focusing on the pile-soil interface, this discussion concludes that the damping ratio in the analytical solution is approximately equal to the constant structural damping coefficient in Ansys. From this point forward, the damping ratio will not be used in the test cases except at the final simulation.

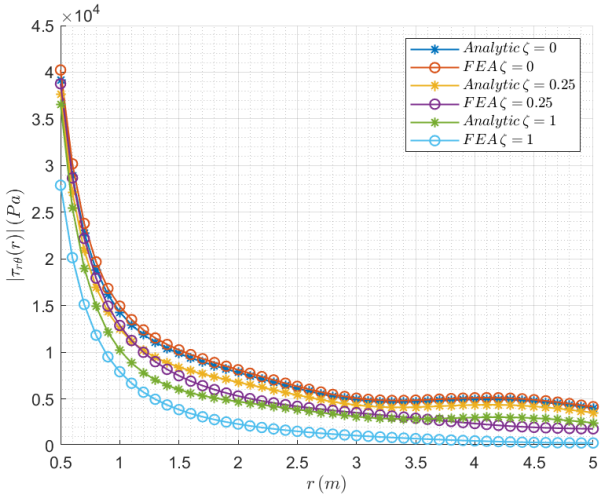

Figure 6.7: $|\tau_{r\theta}(r)|\,(Pa)$ for different ζ

Radius	Damping ratio	Error and correlation	
b	ζ	$\bar{\epsilon_r}\lvert\tau_{r\theta}(r)\rvert$	$r_c\lvert\tau_{r\theta}(r)\rvert$
m	–	–	–
5	0	0.04	0.99
5	0.25	0.26	0.99
5	1	0.60	0.99

Table 6.6: Error and correlation of the shear stress for different ζ

6.4. TC2: Effect of inner soil and mesh sensitivity check

TC2 searches the effect of the inner soil with respect to the model with cavity. Three graphs are plotted in Figure 6.10.a namely the exact solution to the semi-infinite cavity-pile-soil problem, the FE solution to the cavity-pile-soil-dashpot problem, and the FE solution to the soil-pile-soil-dashpot problem. By visual inspection, Figure 6.10.a illustrates that the presence of the inner soil gives small effect to the shear stress response measured by $\bar{\epsilon_r} = 0.17$ and $r_c = 0.99$. This is by assuming that the solution is sampled between $r = 0.5\,m$ and $r = 5.0\,m$ just like the foregoing cases. A closer look at $r = 0.5\,m$ shows that the shear stress increases $2\,\%$ when the inner soil is taken into account in the model. This can be caused by reflection from the opposite side of the monopile. The discussion concludes that the effect of the inner soil to the overall soil response outside the monopile is considerably small.

Additionally, a convergence test of the shear stress distribution around the pile-soil interface is conducted by simulating difference discretization sizes. The goal is to use non-uniform mesh in the soil domain that is to avoid the use of small $\Delta l, s$ in the entire soil domain. From the minimum mesh size of the soil $\Delta l_{soil} = \lambda/10 = 0.45\,m$, several sequential simulations with smaller mesh size is done and plotted in Figure 6.10.b. It shows, from right to left, that $\Delta l_{soil} \leq 0.08\,m$, around the pile-soil interface, leads to small relative error from the preceding simulation ε^* that is defined as

$$\varepsilon^*_{ns} = \left| \frac{\tau_{r\theta,ns} - \tau_{r\theta,ns-1}}{\tau_{r\theta,ns-1}} \right| \tag{6.1}$$

where ns is the number of simulation. Figure 6.9 illustrates the decrease, from right to left, of the mesh size around the pile-soil interface discussed in this section. On the basis of Figure 6.10.b, $\Delta l_{soil} \leq 0.08\,m$ is adopted for the 3D problem.

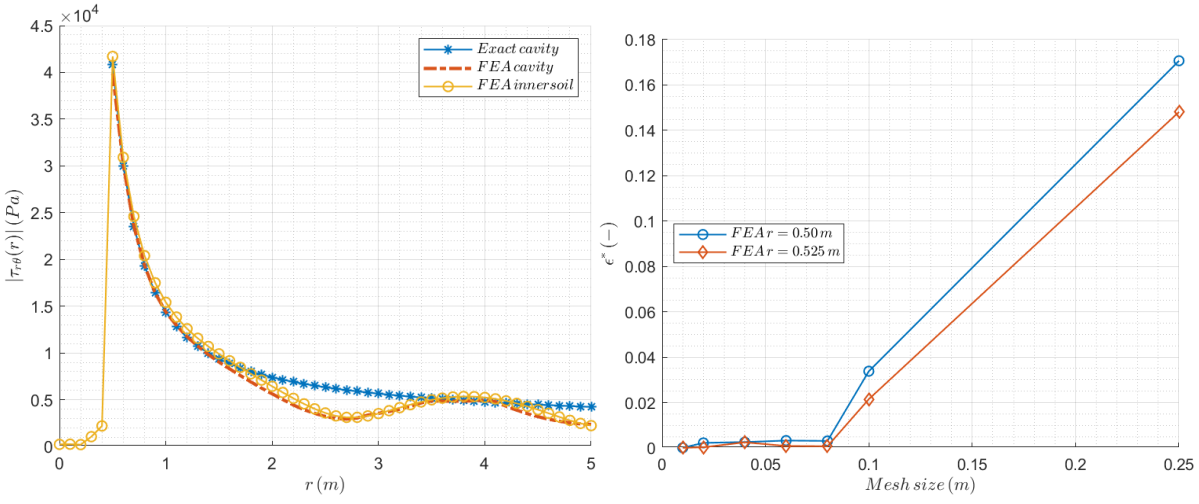

(a) $|(\tau_\theta(r)|$ with and without inner soil (b) ϵ^* (–)

Figure 6.8: Effect of inner soil and mesh sensitivity analysis

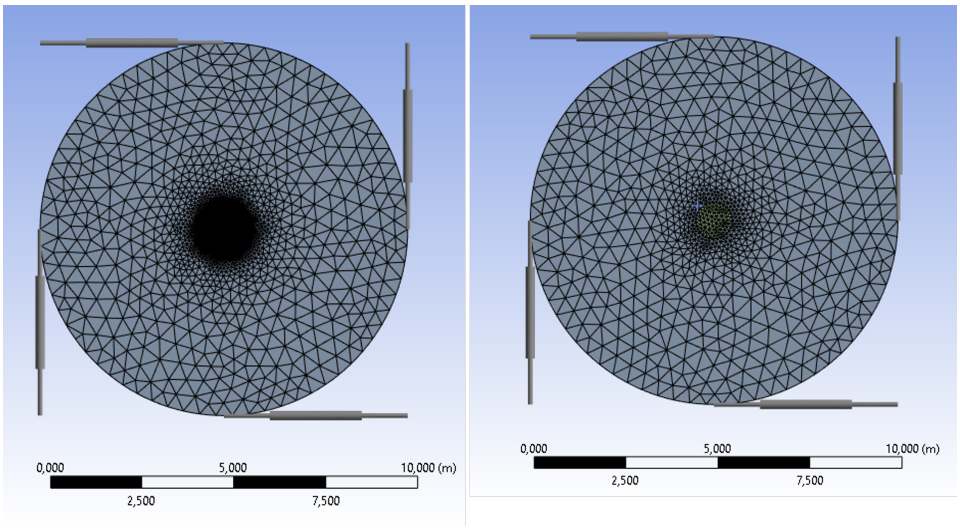

Figure 6.9: Mesh sensitivity study around the pile-soil interface for $\Delta l, s \leq 0.45\, m$

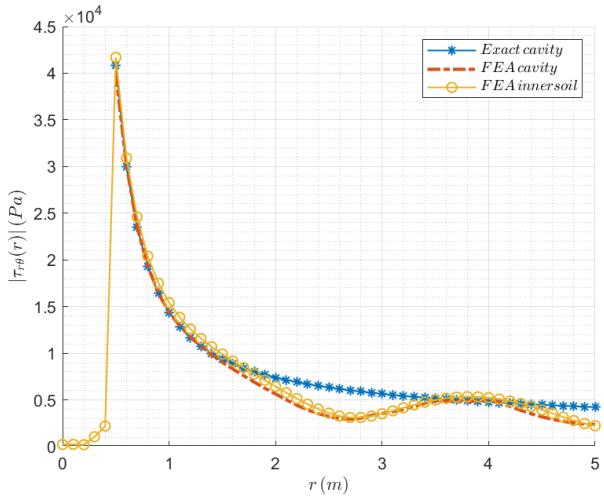

Figure 6.10: Effect of inner soil

7

3D FE modeling, result, and discussion

7.1. 3D modeling

A much the same workflow in Figure 6.1 is applied when modeling in three dimensions. The significant differences from the 2D model are the following. The monopile is now a shell structure, geometrically constructed as a surface. The influence of the thickness will be ensured by activating the *thickness effect*. 3D modeling can be considered extruding both the pile and soil model. However, this is not the case here since the pile is a cylindrical surface. Therefore, a new geometrical model must be produced for the monopile instead of only adding an extrusion unless it is solid. With the soil as a solid, the assembly and meshing will be less complicated when using the pile as a surface. These two advantages stand out when the additional layer is added. The shell structure should have the membrane and bending stiffness activated, which is vital when the analysis considers force in the longitudinal direction of the shell due to self-weight in this case. Otherwise, the error will occur due to excessive deflection in the rotational degree of freedom about the z-direction. To approximate the reality, the soil model is divided into two groups: the soil around the monopile and the additional layer in which no monopile is embedded. The latter is related to imitating the infinite nature of the soil domain in z-direction.

The monopile mesh is formed from triangles with mid-side nodes. Tetrahedral mesh with mid-side nodes is used to mesh the solid instead of the hexahedral mesh. A speedy simulation can be achieved by tetrahedral meshing rather than hexahedral meshing, which is beneficial. One of the most difficult routines has been to conform the mesh at the pile-soil interface, which is the contact between the shell-solid interface. Four meshing procedures are taken through *body sizing*, *patch conforming method*, *contact sizing* and *contact match* to maximize the conforming mesh at the interfaces. However, by visual inspection, while solid-solid contact is conforming or shares the same nodes at the interface, many shell-solid contacts are not conforming. An effort to solve this problem by *node merging* still does not solve the problem. Instead, it creates a problem because the element shape becomes distorted.

Regarding the forcing input, a similar concept of fictitious force is applied following Section 6.1. In 3D, the force is also first distributed along the pile length and its perimeter. At the final simulation, the force is put at $z = z_{top}$ of the extended monopile above the soil surface at $z = 0.0\,m$. Extra sampling points are now taken into account as introduced in Figure 6.2. In r-direction, the solution is investigated at three elevations: at the top $z = 0.0\,m$, middle $z = 0.0 - P_p/2$, and the bottom level $z = z_{tip}$ of the monopile embedded length. In z-direction, the response at the pile-soil interface is of interest from $z = 0.0\,m$ to $z = z_{tip}$. In the first few cases, the response at $r = a$ cannot be captured. Thus, the response at $r = a + 0.1\,m$ is used as an alternative. However, it is found later on that the response at $r = a$ can be obtained after mesh refinement. Before continuing the test cases, the system parameters for the 3D FE modeling are summarized in Table 7.1 and figures in Appendix C are referred.

7.2. TC3: Effect of finite depth

TC3 marks the first 3D model in this report by incorporating a finite length in z-direction, which will be defined here as a finite thickness. The inner soil is also taken into account as a continuation of the

c_2	ρ	G	ρ_p	wt	a	b	τ_o	f
m/s	kg/m^3	N/m^2	kg/m^3	m	m	m	Pa	Hz
360	2022	262051200	7850	0.01	0.5	5.0	40000	80

Table 7.1: Material, geometrical, and external load properties for the 3D test cases

latest test case. Therefore, the effect of the finite thickness is of interest at this stage. As suggested in the preceding paragraph, sampling at three locations is rendered at the top, mid, and bottom elevations. All the parameters follow Table 5.2 in addition to $b = 5\,m$ that follows the conclusion in TC1. With the finite thickness of $6\,m$ following $Data1$ in Table 2.1, the non-reflective coefficient K_{dp} and C_{dp} as in Table 6.1 becomes $3.7 \times 10^9\,N/m$ and 3.4×10^7 due to the integration along the depth. At $z = 0.0\,m$ and $z = z_{tip}$, $free$ boundary condition is applied to the pile-soil system.

Figure 7.1.a is the image of the shear stress responses corresponding to the three depths and the exact solution. Notice that all three responses befall each other, shown by a single visible response next to the exact solution. Although not displayed in the same plot, a slight difference is observable if Figure 6.10 is recalled. However, if not attentive, one would miss the fact that the shear stress at the pile-soil interface becomes practically zero in Figure 7.1.a. The computed error and correlation of $\bar{\epsilon_r} = 0.13$ and $r_c = 0.99$ for the response between $r = 0.51\,m$ and $r = 5\,m$ prove that the FE solution agrees with the exact solution in the region away from the pile.

What is more, TC3 examines the shear stress along the monopile depth at the pile-soil interface as plotted in Figure 7.1.b. As mentioned in the previous paragraph, the solution at the interface cannot be captured well. Therefore, an additional solution in the vicinity of the interface at $r = 0.51\,m$ is shown here. Visually, it shows that the shear stress, along the depth at $r = 0.51\,m$, is in the same order of magnitude as the shear stress in Figure 6.10. The constant response, along the depth at $r = 0.51\,m$, in Figure 7.1.b, reinforces the previous statement that the shear response is the same at three different levels of z. In view of force equilibrium, the response is in the same order of magnitude compared to the fictitious force amplitude $\tau_o = 40\,kPa$ as in Table 5.2.

Despite the inability to capture the response at $r = a$, the maximum response in Figure 7.1.a still agrees with the exact solution. Secondly, in z-direction, the response at $r = 0.50\,m$ can be interpolated from the response at $r = 0.51\,m$, which shows good agreement with the principle of force equilibrium. For these reasons, the discussion for TC3 is closed by concluding: in terms of the shear stress response, the finite thickness model with $free$-$free$ boundary condition will be assumed to be equivalent to the 2D plane strain semi-infinite model by noting the elaborated limitations.

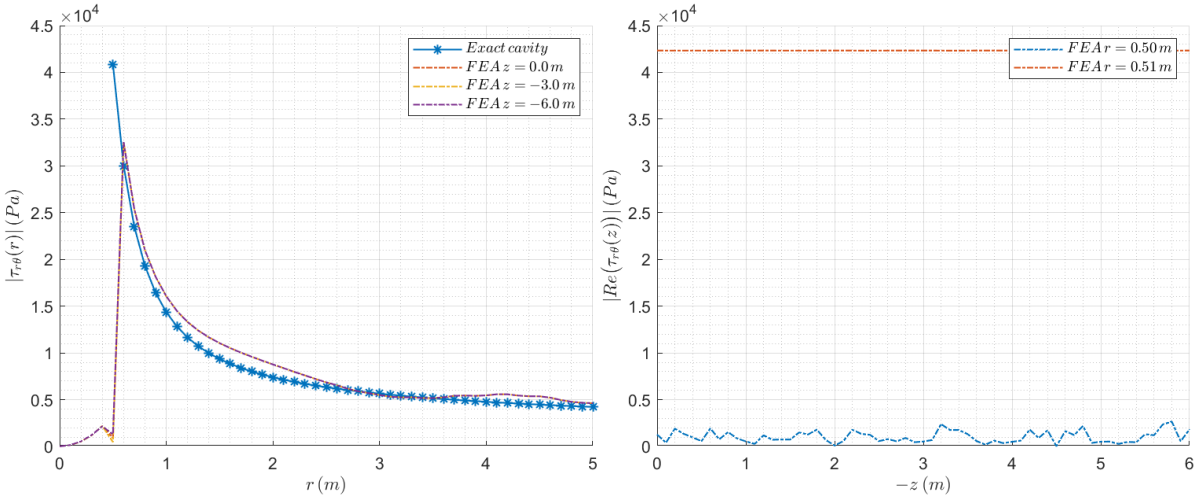

(a) $|\tau_{r\theta}(r)|\,(Pa)$ (b) $|\tau_{r\theta}(z)|\,(Pa)$

Figure 7.1: Effect of finite depth

7.3. TC4: Effect of an additional soil layer below the pile tip

To designate the depth of the additional layer below the pile tip, TC4 is carried out. This task is deemed necessary because of the following. Firstly, the presence of soil underneath the pile is essentially true. Secondly, the extent to which the depth is modeled has yet to be fully understood. Section 5.1 demonstrates that the effect of the bottom boundary is small when applying $H_\Omega = 13D_o$. In the same manner as the discussion regarding the horizontal extent of the soil domain, the vertical extent of the soil domain below the pile tip is desired to be small. The interface condition between the additional soil layer and the top soil and pile assumes displacement and stress continuity (*i.e.* perfectly bonded). A new pair of non-reflective coefficients K_{dp} and C_{dp} are assigned at the outer boundary of the additional soil layer, similarly to the outer boundary of the top layer.

It is sought in such a way that the effect of the boundary at the bottom is negligible. The matter is settled by establishing force equilibrium at the pile-soil interface. Also, a non-reflective boundary in $C_{dp,z}$ is added in r-θ plane at the bottom of the additional soil layer. A similar idea for deriving its radial counterpart K_{dp} and C_{dp} yields the non-reflective boundary without a spring element as described in Section 5.6. Note that these two non-reflective boundaries are approximated by means of one-dimensional wave theory. However, it will be shown later that force equilibrium at the pile-soil interface can be approximated by using these viscous boundaries.

The same material as the soil in the upper layer is assumed. At TC4, the tetrahedral mesh is imposed upon the upper and additional soil layers. The monopile mesh is in the form of triangles to maximize contact matching with the tetrahedral mesh. Although the meshing method is different, the meshing size is still the same with TC3, which are $\Delta l_{soil} = \lambda/10 = 0.45\,m$ and $\Delta l = 0.2\,m$. By contact sizing, the soil around the pile-soil interface will have $\Delta l_{soil} = \Delta l = 0.2\,m$. At this point, the meshing is twice larger than in the 2D modeling to explore faster simulations at the risk of larger error around 10% according to Figure 6.10.

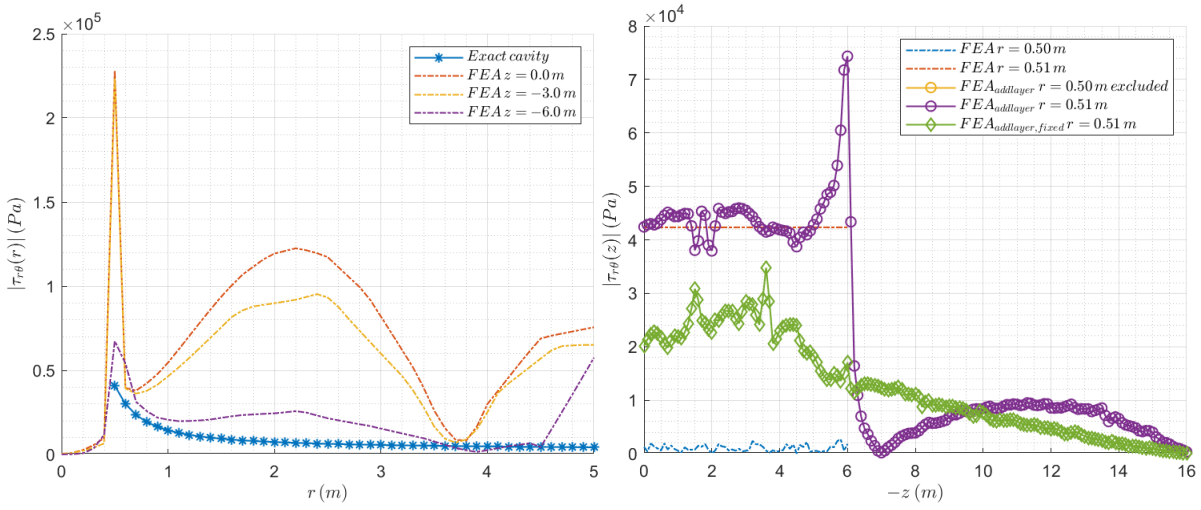

(a) $\tau_{r\theta}(r)|\,(Pa)$ (b) $\tau_{r\theta}(z)|\,(Pa)$

Figure 7.2: Effect of finite depth

Plots of the shear stress in the radial direction at three elevations of the top layer in Figure 7.2.a shows that the deviation becomes larger than the exact solution. Visually, the largest deviation appears at $z = 0\,m$ and decreases to the smallest deviation at $z = -6.0\,m$. It can be the indication that the one-dimensional non-reflective boundary breaks down. The appearance of nodes and antinodes is obvious, similar to the response to the semi-infinite problem when $free$ or $fixed$ boundary is used under the plane strain assumption. It seems that assessing the response with respect to the semi-infinite solution is no longer relevant and more difficult.

Figure 7.2.b shows the shear stress in the proximity of pile-soil contact at $r = 0.51\,m$. Once again, this is because the response at $r = 0.50\,m$ cannot be captured well. Force equilibrium due to the

fictitious force of $\tau_o = 40\,kPa$ can be approximated when the additional soil layer $H_{\Omega p} = 10\,m$. This means that $H_\Omega = \frac{6+10}{1.0} = 16D_o > 13D_o$ as introduced in Section 5.1. When a $fixed$ boundary is used at the bottom of the additional soil layer, the shear response at $r = 0.51\,m$ is not in the order of $\tau_o = 40\,kPa$, which indicates that the solution in the interior domain is disturbed by reflection. The $fixed$ boundary is highlighted because a rigid boundary is often assumed due to the existence of a hard-bearing stratum at a large depth of earth. However, a fixation should not be used in this case.

A stress jump at the pile-soil contact normal to $r-\theta$ plane is seen from the first time, shown at z_{tip}. The occurrence of stress jump somewhat counteracts the assumption on the continuity of displacements and stresses, which are enforced at the interfaces. It is expected due to material discontinuities where the pile tip meets the soil underneath it. Jumps are also pictured at $r = 0.5\,m$ when Figure 7.2.a is recalled. It can be associated with the fact that the stress-free condition at the top and bottom of the pile-soil system in the previous analyses is no longer the case. In other words, the presence of the additional soil layer gives a reaction at the pile-soil contact. Stress jumps have also been observed even at the soil-soil interface in another study about soil-pile interaction (Anoyatis & Mylonakis, 2011).

The stress jump can also be associated with a stress singularity where the elasticity theory tends to be inaccurate at corners (C. Kasbergen, personal communication, 17 January, 2023) (A. Metrikine, personal communication, 20 January, 2023). Finally, the response below the pile tip is not interesting to be examined, ergo not discussed further. To sum up the TC4 matter, force equilibrium along the pile-soil interface seems handier than assessing the shear stress response in the radial direction with reference to the exact solution. Therefore, in what follows, force equilibrium at the pile-soil interface will be used as the primary tool to examine the simulation.

7.4. TC5: Effect of soil layering around the monopile

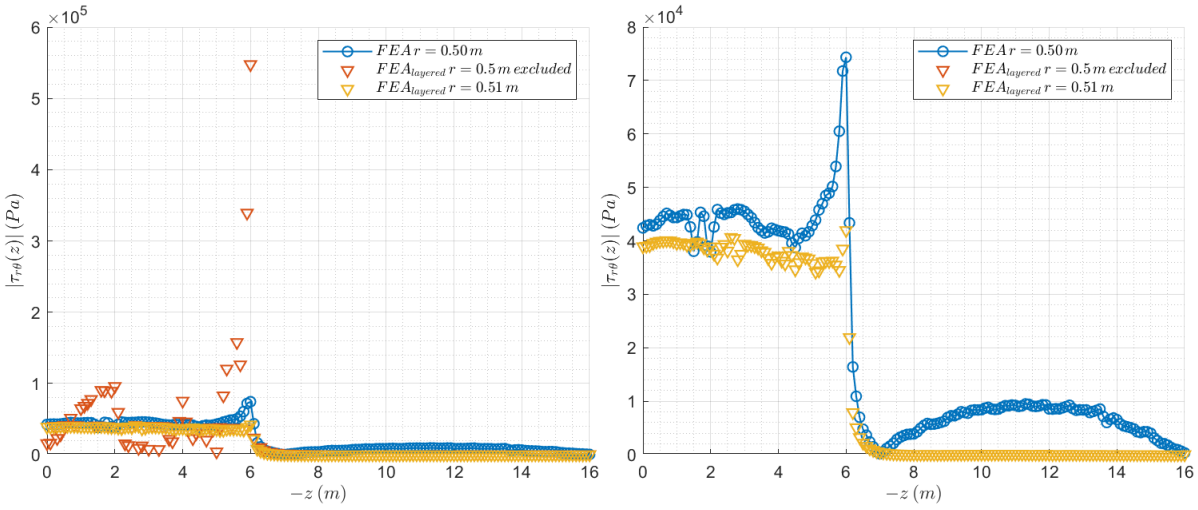

(a) $|\tau_{r\theta}(z)|\,(Pa)$ (b) $|\tau_{r\theta}(z)|\,(Pa)$

Figure 7.3: Effect of soil layering

To accommodate the hypothesis on the overall behavior of the pile-soil system, as introduced in Section 3.4.3, the top soil is modeled as three discrete layers. The contact between these layers is also perfectly bonded, as described in the previous Section. Therefore, the coefficient K_{dp} and C_{dp} must be adjusted per the thickness of the layers. Other than that, the model is a copy of the TC4 model. It is found that layering influences the solution to some extent. It indicates that the solution does not converge yet, and mesh refinement is needed.

Figure 7.3.a demonstrates that the shear stress at $r = 0.5\,m$ is not captured well like at TC4, although a fictitious force is uniformly distributed at $r = a$ along the monopile. At $r = 0.51\,m$, the shear stress is in the order of magnitude of the fictitious force $\tau_o = 40\,kPa$ with a noticeable variation in view

of TC4. The most considerable difference occurs around the pile tip, where the amplitude of the jump reduces. Since the shear stress below the pile tip is unimportant, it is left as is and no further discourse is made about it. Finally, TC5 concludes that the model with a layered top soil is acceptable because the force equilibrium near the pile-soil interface can be approximated.

7.5. TC6: Effect of gravity without and with the monopile above the soil surface

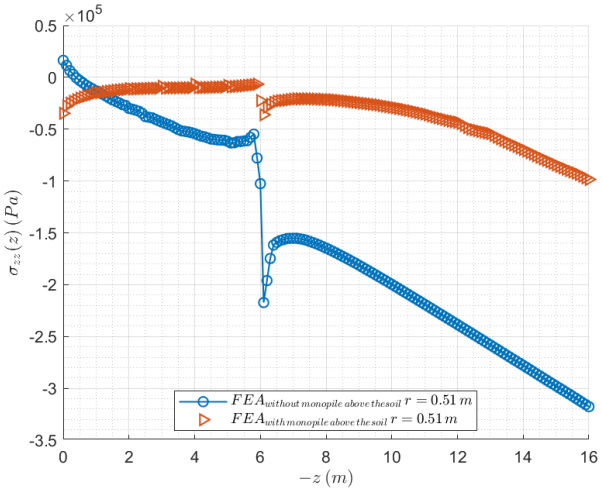

Figure 7.4: The initial vertical stress without and with the monopile above the soil

The test case is continued by the insertion of constant acceleration of earth gravity $g = 9.81\,m/s^2$ in the negative z-direction with reference to Figure 7.18. Two FE analyses are performed, namely without and with the monopile that extends from $z = 0\,m$ to $z = z_{top}$ and the vertical stress $\sigma_{zz}(z)$ at $r = 0.51\,m$ is evaluated in the Static Structural toolbox. The assumption of hydrostatic distribution for the vertical stress holds by implementing the boundary conditions introduced in Section 4.2. Notice that up until TC5, no monopile above the soil is yet included and the simulation is done within the harmonic analysis framework in the Harmonic Response toolbox. The stiffness of the overall pile-soil system is expected to change to some extent due to the initial stress. Figure 7.4 is quoted to verify the implementation of initial stress.

Without the monopile above the soil surface, the assumed hydrostatic distribution of the vertical stress is clarified with the linearly increasing magnitude from the surface to the depth beneath it. For example, at a large depth below the pile tip

$$\sigma_{zz}(z = -15.5) = \rho\, g\, z = 2022 \times 9.81 \times -15.5 \approx -307\,kPa \tag{7.1}$$

which agrees well with Figure 7.4. Nonetheless, the expected zero vertical stress does not hold at the soil surface, which can be related to the assumption of a perfectly bonded connection at the pile-soil interface in the modeling. So, there is a local tension around the pile due to the larger steel mass density than the soil. The jump appears at the pile tip as before due to material discontinuity.

The monopile above the soil surface alters the soil vertical stress distribution that spans from the soil surface down to the large depth below the pile tip, particularly near the embedded pile where hydrostatic distribution is not the case anymore. The vertical stress at the soil surface even becomes compressed unlike the one discussed in the preceding paragraph. More compression at the soil surface can be associated with the additional weight from the extended monopile and then the Poisson's effect comes into play by expanding the monopile radially, which compresses the soil.

Below $z = -1\,m$, the magnitude of the vertical stress decreases non-linearly in magnitude until the pile tip, which shows that the pile tends to tension the soil. If sand is considered, the appearance of

tension in it is not realistic due to the absence of chemical bonding between its grain that allows tension. The same tendency can be observed below the pile tip, in which the magnitude of the vertical stress increases non-linearly, starting from $z = 7.5\,m$ where the influence of stress jump subsides. These can also be related to the assumption of perfectly bonded contact at the pile-soil interface, where the simulation ensures displacement continuity. Hence, the soil follows the monopile due to its larger weight.

7.6. Finding the torque amplitude and the clamping force

Since the initial stress has been included, the pre-stressed harmonic analysis of the torsional vibration of the monopile is ready to be carried out. A fictitious force per unit area with amplitude τ_o that is uniformly distributed along the monopile circumference and depth between $z = 0\,m$ and $z = z_{tip}$ is no longer applied. Instead, a force amplitude f_o is uniformly distributed along the circumference at the pile top $z = z_{top}$. The very first force amplitude is arbitrary because this force amplitude will be the one that is to be found. Damping will be incorporated in terms of damping ratio, for which the soil damping ratio $\zeta = 5\%$ is assumed as introduced in Section 6.3, and the steel damping ratio assumes $\zeta_p = 2\%$.[1] At this stage, the soil layers are updated from three to six discrete layers to explore more simulation possibilities. Table 7.2 and Table 7.3 summarize the system parameters used to find the force amplitude.

D_o	L_p	wt	P_p	D_Ω	H_Ω	a
m	m	m	m	m	m	m
1.0	10.5	0.01	6.0	10	16	0.5

Table 7.2: Geometrical properties for finding the torque amplitude

c_2	ρ	G	ζ	$c_{2,p}$	ρ_p	G_p	ζ_p	f
m/s	kg/m^3	N/m^2	%	m/s	kg/m^3	N/m^2	%	Hz
360	2022	2.62×10^8	5	3208	7850	8.08×10^{10}	2	80

Table 7.3: Material and external load properties for finding the torque amplitude

Due to the thickness of the assumed monopile dimensions, the ideal location to sample the maximum shear stress will be at $r = 0.505\,m$. However, it is observed that in the region between $r = a$ and $r = a + 0.1\,m$, the maximum shear stress does not converge, which is not the case for the stress at $r = a$ and $r = a + 0.1\,m$. Note that a stress jump occurs at $r = a$ and the shear stress drops very fast at $r = a + 0.1\,m$ due to material discontinuities like in the case of stress jump at the pile tip described in the previous test case. The shear stress at $r = a + 0.1\,m$ is in the order of 1% of the shear stress at $r = a$. The magnitude of the maximum shear stress for the soil failure is then assumed at $r = a + 0.1\,m$ to allow for conservatism. Although the assumption is controversial, intuition on the relative difference between simulation outcomes can still be understood. Hence, the discussion is continued and the stress jump problem is saved for further discussion.

By assuming six discrete layers, eight possible simulations are done to delve into the hypothesis on the overall pile-soil failure mechanisms. Figure 7.6 and 7.7 exemplify the distributions of the maximum shear in the soil τ_{max} along the depth z when they exceed the Mohr-Coulomb failure criterion of the targeted soil layers. While Figure 7.6.a and 7.6.b assume six and three discrete layers, Figure 7.7.a and 7.7.b assume two and one discrete layers shown by the number of peaks in each plot. Crossings between the maximum shear and the dotted blue line (*i.e.* failure criterion) at each depth of the discrete layer identify the failure condition in which slip takes place.

[1] For the given range of small soil damping assumption $1\% - 5\%$, $\zeta = 5\%$ is deemed the worst condition, which leads to the smallest amplitude response. $\zeta_p = 2\%$ is, in fact, above the upper limit of the typical damping ratio in steel structures $\zeta_p = 0.5\% - 1.5\%$ (Shirzadeh et al., 2013). It is intended to account for hydrodynamic damping due to wave radiation. However, it is a mere rough approximation because damping must be measured experimentally and measuring the damping ratio is beyond the scope of this study.

Let Figure 7.6.b be an example to focus the discussion. It is clear that the green solid line l_4 crosses the failure criterion at depth $z = -4\,m$. The location of the peak at $z = -2\,m$ shows that the pile-soil contact between $z = z_{bed} = 0$ and $z = -1\,m$ is detached as per assumption. The disconnection is also justified by the magnitude of the shear stress that is close to zero above the peak. The shear stress decreases exponentially from the peak toward the depth where the pile-soil contact is active below the peak. It indicates that the shear stress radiates into deeper soil region in addition to the radiation in the radial direction as discussed in Chapter 5. Whilst the latter is governed by the Hankel function, the former is dictated by the Airy function, and of course they are both weakened more by the energy dissipation due to viscous damping. At the region close to the pile tip, a singular behavior appears as the pile meets the soil, where the shear stress increases but with the magnitude much lower than the peak stress. It informs that the source comes from the depth above it, which is true.

When looking at the overall trend of the peak in Figure 7.6.a and 7.6.b, the peaks form a peak group shown by the largest magnitude of around $3.3 \times 10^5\,Pa$ and $6.3 \times 10^5\,Pa$, respectively. Going back to the bigger picture in Figure 7.6 and 7.7, it is noticeable that the magnitude of the peak differs for each pile-soil failure assumptions, where the largest magnitude occurs when the failure assumes full depth (*i.e.* one layer) and the smallest one when the failure assumes six layers, which makes sense at least due to the linearly increasing failure criterion with depth. The force amplitudes that generate the maximum shear stress distribution are then analyzed to get more insight.

Other hypothetical failure sequences are simulated and the resulting force amplitudes f_o of eight $VIII$ simulations are summarized in Figure 7.8. While the bar chart with blue color shows the local trend within each simulation, the red colored bar chart displays the relation between the maximum force amplitudes in each simulation. As indicated in the previous paragraph, the local maximum of the force amplitudes arise at different location following different assumptions. For instance, whilst in simulation I the peak is at l_3, simulation II has a peak at l_{3-4}. Notice that the peak location is not exactly the same between the force amplitude and the maximum shear stress. It can be associated with the combined effect of larger shear stress produced by larger torsion due to longer unsupported length of the monopile and the increasing failure criterion with depth. The exponentially decreasing behavior of the shear stress and the linearly increasing failure criterion also contribute into it.

Furthermore, Figure 7.8 says that the maximum force amplitude is smallest when the simulation assumes six layers and largest when the simulation assumes one layer because the former divides the job into smaller tasks rather than doing all in one go in addition to the increasing failure criterion with depth. The maximum force amplitude in the other simulations vary in between the two. All together, the maximum force amplitude in each simulation corresponds to the discrete layer in which the third layer l_3 is part of. It can be attributed to the centroid of the shearing resistance triangle at $z = -4\,m$. Therefore, a new hypothesis can be proposed, which says that it is sufficient to fail the first two-third of the soil layers in sandy soil. Besides, one can also examine that at depth $z = -4\,m$, the shear stress begins to approximate zero in Figure 7.7.b when the thickest soil layer is assumed. Hence, the soil failure at $z = -4\,m$ tends to not happen due to small shearing is left. Then, another hypothesis is proposed, which says that the depth at which the shear stress approaches zero is the location that determines the soil failure below it.

The first hypothesis seems unlikely when the soil is stiff such as dense sand or stiff clay and at the same time the embedded length is long. It is because in a relatively stiff soil, the decaying shear stress will be so quick which leads to a huge force $f_{o,h}$ to generate large shear stress at the two-third of the embedded depth if the elasticity holds. Even if $f_{o,h}$ is excited, the shear stress closer to the soil surface will experience larger shear stress, which likely to have exceeded the failure criterion. Thus, a smaller force $f_{o,s}$ such that $f_{o,s} < f_{o,h}$ is preferred to evaluate the shear stress at the depth closer to the soil surface, which leads to the second hypothesis. However, it brings up a new issue about to what extent the zero is approached. The matter is put on hold for the time being and another concern is addressed.

Scattered force amplitudes

If the assumed failure mechanisms are true, there will be infinitely many possible combinations if infinitely many discrete soil layer (*i.e.* infinitely small thickness) is considered, which necessitate the concept of probability distribution to describe the maximum force amplitude for each combination.

A commonly used probability distribution in reliability engineering is the Weibull distribution[2]. Due to the limited number of simulations, and since more soil layering in 3D FE modeling tends to be computationally expensive because of the demand of small element size with a large domain, the local maxima of force amplitudes will be assumed to follow the Weibull distribution.

Following the Weibull distribution, Figure 7.8 is converted to Figure 7.5, which leads to the expected force amplitude $\bar{f}_o = 3.19 \times 10^6\ N$, where the Weibull shape and scale parameter are $\alpha_W = 0.932$ and $\beta_W = 3.09 \times 10^6$, respectively. The expected value is in the same order of magnitude with the force to fail the first four layers $f_{o,IV,1-4} = 3.10 \times 10^6\ N$ shown in simulation IV with 2% difference. Since the difference is small, $\bar{f}_o \approx 3.10 \times 10^6\ N$. From the cumulative distribution function (CDF) of the Weibull distribution, the probability that the force amplitude is less than $\bar{f}_o = 3.10 \times 10^6\ N$ $P(f_o \leq \bar{f}_o)$ will be 63%. In other words, the probability that the soil will fail by applying $\bar{f}_o$ is 63%. If $f_{o,VIII,1-6} = 9.34 \times 10^6\ N$ in Figure 7.8 is applied the probability to fail the soil becomes 94% and will be defined as the maximum value $f_{o,max}$.

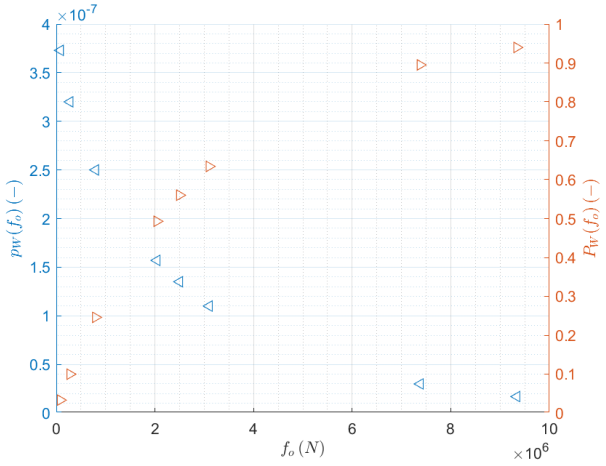

Figure 7.5: The assumed Weibull distribution of the maximum force amplitudes f_o

Accordingly, the torque amplitude T_o can be specified to be between $\bar{T}_o = 3.10 \times 10^6 \times 0.5 = 1.55 \times 10^6\ Nm$ and $T_{o,max} = 9.34 \times 10^6 \times 0.5 = 4.67 \times 10^6\ Nm$. Finally, the clamping force can be obtained as $\bar{N}_o = \bar{f}_o / \mu_{ex,ss} = 3.10 \times 10^6 / 0.7 = 4.43 \times 10^6\ N$ and $N_{o,max} = f_{o,max} / \mu_{ex,ss} = 9.34 \times 10^6 / 0.7 = 1.33 \times 10^7\ N$. The results are then summarized in Table 7.4 and 7.5.

$-$	f_o	$Re(U_\theta)$	$Im(U_\theta)$	$\lvert U_\theta \rvert$	Φ
$-$	N	m	m	m	rad
$Expected\ value$	3.10×10^6	8.69×10^{-3}	5.17×10^{-4}	8.71×10^{-3}	0.0594
$Maximum\ value$	9.34×10^6	2.60×10^{-2}	1.65×10^{-3}	2.61×10^{-2}	0.0634

Table 7.4: Summary of the output for $D_o = 1.0\ m$ (1/2)

7.7. The required power

Since the forcing amplitudes and the real and imaginary part of the displacement are now known, the average power consumption to vibrate the monopile can be estimated. As can be seen in Table 7.5, the expected power is ten times smaller than the maximum power, which is not the case for the computed

[2]Weibull distribution is often suitable to describe structural engineering phenomena such as fatigue, fracture, and strength. The probability density function of a variable x is defined as $p_W(x) = \frac{\alpha_W x^{\alpha_W - 1}}{\beta_W^{\alpha_W}} \exp\left(-\left(\frac{x}{\beta_W}\right)^{\alpha_W}\right), x \geq 0, \alpha_W > 0, \beta_W > 0$ and the corresponding cumulative distribution function is $P_W(x) = 1 - \exp\left(-\left(\frac{x}{\beta_W}\right)^{\alpha}\right), x > 0$ (Choi et al., 2007)

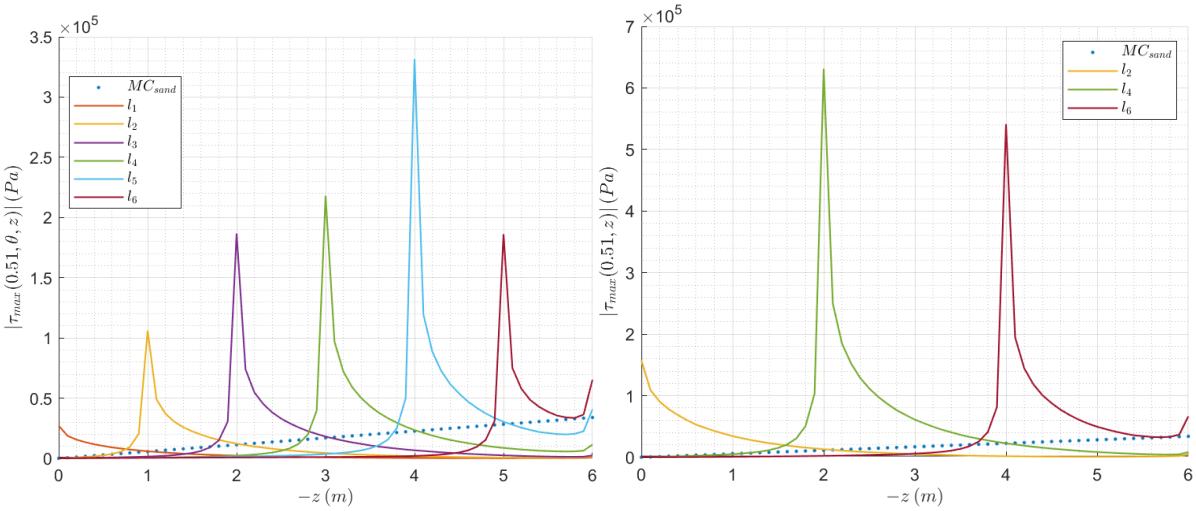

(a) $|\tau_{r\theta}(0.5,z)|\,(Pa)$ assuming 6 discrete layers (b) $|\tau_{r\theta}(0.5,z)|\,(Pa)$ assuming 3 discrete layers

Figure 7.6: Maximum shear stress at the pile-soil interface

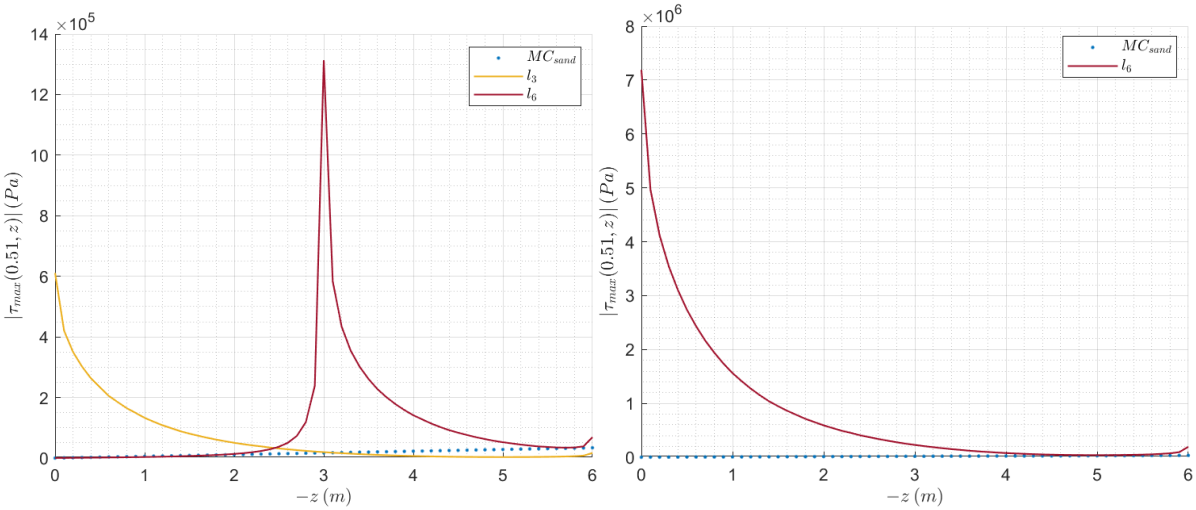

(a) $|\tau_{r\theta}(0.5,z)|\,(Pa)$ assuming 2 discrete layers (b) $|\tau_{r\theta}(0.5,z)|\,(Pa)$ assuming 1 discrete layer

Figure 7.7: Maximum shear stress at the pile-soil interface

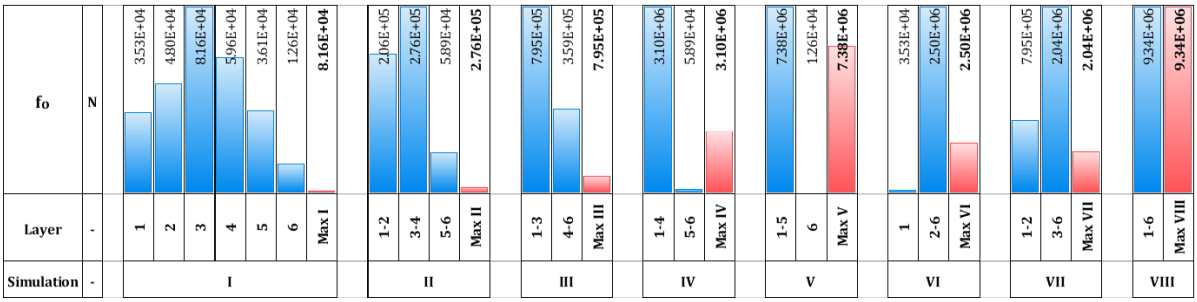

Figure 7.8: Summary of the force amplitude to fail the soil layer $f_{o,l}$

circumferential force f_o, torque T_o, and clamping force N_o, where $\frac{\bar{f}_o}{f_{o,max}} \approx \frac{\bar{T}_o}{T_{o,max}} \approx \frac{\bar{N}_o}{N_{o,max}} \approx 0.33$. It is mainly because $\frac{|\bar{U}_\theta|}{|U_{\theta,max}|} \approx 0.33$ shown implicitly in Table 7.4, which leads to a squared difference of the

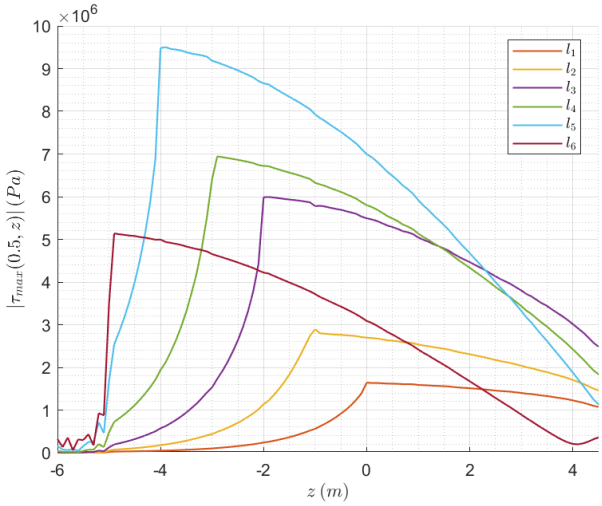

Figure 7.9: Amplitude of the shear stress along the monopile

expected and maximum power. If the assumption on the gradual soil failure mechanism is true, then it is preferred to apply the force amplitude at the expected value that will fail the first two-third layer of the soil rather than applying the maximum force amplitude. Additionally, the squared difference confirms that the linear assumption is held as intended shown by the same force-displacement proportionality throughout the simulations.

Finally, if the expected value of the average power is regarded as the operational power, Table 7.5 also predicts that the current GDP shaker will need to be upgraded for the purpose of monopile decommissioning with the dimensions D_o, L_p, wt, and P_p assumed in Table 7.2, since its operational power is $188\,kW < 403\,kW$. Recalling the emergence of stress jumps at the pile-soil interface, the computed operational power is questionable due to the assumed shear stress that is taken at $r = a + 0.1\,m$. If the shear stress at $r = a$ (*i.e.* in the pile) is used, the power can be as small as $40.34\,W$, thus the computed power cannot yet be relied upon. So, a validation through laboratory or field tests are required.

–	T_o	N_o	P_{ave}
–	Nm	N	W
$Expected\,value$	1.55×10^6	4.43×10^6	4.03×10^5
$Maximum\,value$	4.67×10^6	1.33×10^7	3.87×10^6

Table 7.5: Summary of the output for $D_o = 1.0\,m$ (2/2)

7.8. Inquiring the shear stress in the pile

The procedure to fail the soil layers by assuming discrete layers still contain uncertainty due to no validation against experimental data is yet conducted. Contrasting one of the outcomes of the 3D FE analysis and 1D shell-spring-dashpot derived in Section 5.74 is done to reduce the uncertainty. But first, an example of overall shear stress in the pile is plotted in Figure 7.9 taking an example from simulation I, which has six discrete layers and therefore will have six graphs. The shear stress in the pile forms six peaks and peak envelope that are similar as in Figure 7.6.a, which confirms that they correspond to the same simulation[3].

The same exponentially decreasing behavior with soil depth of the shear stress is generally the same between the two, which starts from the topmost part of the targeted soil layer where the pile-soil contact is maintained. The main difference is the non-zero shear stress distribution above the targeted soil layer, which has a quadratic trend from the pile top $z = 4.5\,m$. An inflection point is visible when

[3]Note that the x-axis in Figure 7.9 and 7.6.a must be read in the opposite manner to each other.

the remaining soil layer is $1\,m$ thick. Additionally, the trend of the shear stress at the pile top does not follow the trend of the peak, for instance, at $\tau_{max}(z = 4.5)$ of l_5 is not the maximum among other shear stresses at the same z. While the emergence of an inflection point is not fully understood, the latter can be linked to the presence of soil mass around the pile-soil contacts that are disconnected.

The use of a shell-spring-dashpot model

When l_1 in Figure 7.9 is plotted together with the amplitude of the shear stress due to the analytical formulation in Section 5.74, a comparable pattern can be seen in Figure 7.10, which shows that the analytical solution $Analytic\,l_1$ underestimates the FE solution $FEA\,l_1$ except at the pile top, with the average error $\bar{\epsilon}_r = 0.52$, correlation coefficient $r_c = 0.98$, and error $\epsilon_{r,peak} = 0.13$ is recorded at the peak shear at $z = 0\,m$. Note that the same f_o is applied at the pile top to make a fair comparison. On the other hand, though $Analytic\,l_6$ and $FEA\,l_6$ do not agree well with each other in terms of magnitude, $Analytic\,l_6$ can roughly capture the onset of the exponentially decreasing behavior of the shear stress due to the presence of the pile-soil contact and the quadratic distribution of the shear stress above the soil with $\bar{\epsilon}_r = 1.44$, $r_c = 0.86$, and $\epsilon_{r,peak} = 0.17$. Due to these discrepancies, it is expected that error in terms of displacement also exists, which means that the corresponding power consumption is not yet reliable if computed through the current analytical model.

Furthermore, it is expected that the analytical solution will deviate the FE model because it simplifies the problem more. While around $z = -4\,m$ to $z = -2.5\,m$, the $Analytic\,l_6$ underestimates the $FEA\,l_6$, $Analytic\,l_6$ overestimate the $FEA\,l_6$ between $z = -2.5\,m$ to $z = 4.5\,m$. The lack of matching between $Analytic\,l_6$ and $FEA\,l_6$ can be due to ignoring the soil mass around the failed pile-soil interface, which is substantiated by a better agreement between $Analytic\,l_1$ and $FEA\,l_1$ which assume complete pile-soil contact (*i.e.* no pile-soil contact failure has yet occurs). Also, the effect of initial stresses is neglected by the analytical model. In view of a quite good agreement between the $Analytic\,l_1$ and $FEA\,l_1$, one can concludes that the FE model performs as assumed in which an elastic cylindrical shell partly rests on a visco-elastic foundation subject to a harmonic circumferential force at the pile top.

It seems that the analytical model will match the FE model better if better assumptions and calibration are made to construct the model, for example by the inclusion of mass elements in addition to spring and dashpots to represent the soil or by considering plasticity through plastic slider as suggested by another work for large-diameter pile installation (Tsetas et al., 2021). It is natural to prioritize the use of a more simplified model if it can already give insight similar to the 3D FE analysis. Taking advantage of axisymmteric condition through analytical model can lead to clear advantages such as shorter duration and smaller memory requirements due to less equations are being solved. Therefore, this thesis suggests to move on to the improvement of 1D shell-spring-dashpot model.

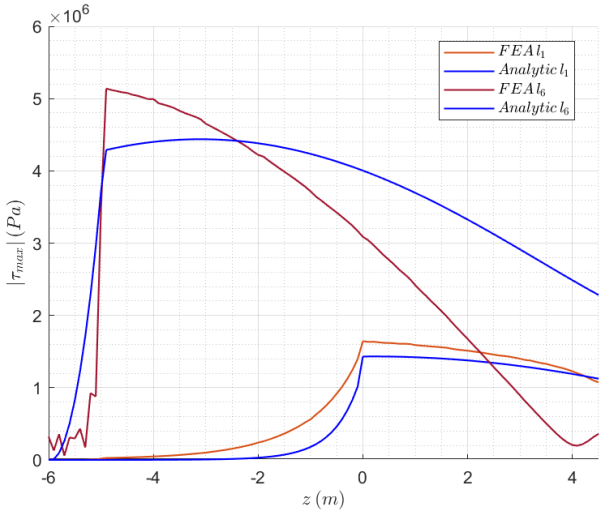

Figure 7.10: 3D FE analysis versus 1D shell-spring-dashpot model

7.9. Toward validation against field experiments

By virtue of a comparable shear stress distribution between the 3D FE analysis, an extrapolation to predict the force amplitude and its by-products for larger diameters and the effect of the GDP shaker's mass is of interest. First the analytical model is calibrated against two literature concerning torsional response of piles by Georgiadis and Saflekou (Georgiadis & Saflekou, 1990) and Stoll (Dong Guo & Randolph, 1996). Since no available information on the shear stress distribution of the soil in the r-direction, the shear stress in the pile is used. Inspired by the hypothesis in the 7^{th} and 10^{th} paragraph in Section 7.6 regarding the tendency of the soil failure location, a computation schema to determine the force amplitude f_o, thus torque amplitude T_o, is proposed.

It says that f_o is the average of several force amplitudes, which generate the shear stresses larger than the failure criterion at their corresponding points within depth, where the decaying function due to spring reaction approaches zero. In step-wise, the calculation scheme essentially consists of four steps: 1. plot the TF with the spring along the embedded depth of the pile; 2. estimate and assume the coordinates where the shear stresses approach zero; 3. find the force amplitudes that produce the shear stresses over the failure criterion ratio larger or equal to unity at the assumed coordinates; and 4. take the average of the force or torque amplitudes. Due to the failure of the first layer, a new embedded depth is assumed and four steps are repeated. Finally, take the maximum of the average torque amplitudes to obtain the torque capacity.

Comparison with a prediction by Georgiadis and Saflekou

Figures and tables in Appendix D are referred to compare the proposed method with the first literature. Figure D.1 shows three predictions of torque capacity with the influence different additional axial load. Due to the additional axial load, the comparison is essentially not apples to apples. However, it is still possible to get an insight from the one with the smallest axial load around $0.5 \times 10^3\ kN$ that gives a torque capacity $T_{o,GS} = 7000\ kNm$. Generally, Figure D illustrates that the torque capacity decreases with the increase of the axial load. Thus, it is natural to expect that without the additional axial load, the torque capacity will be larger than $7000\ kNm$.

The prediction refers to an offshore steel pipe piles characterized in Table D.1. Steel material following Section 2.2 is assumed due to no specific metric of steel material properties provided. Soft clay is identified from Table D.1 and its shear wave speed is assumed as $c_2 = 100\ m/s$ following Eurocode 8 in Table 3.1 for soft clay. Finally, the loading frequency is assumed as static due to no specific information about it, which means that $\omega = 0\ rad/s$. Five A-FRF due to a unit force are plotted to assume five discrete layers. With the help of Excel spreadsheet and Maple, the proposed calculation method estimates the torque capacity of $T_o = 7878\ kNm$ shown in Figure D.1, which means that $7878\ kNm > 7000\ kNm$ as expected. In light of the error in the previous section, the estimated torque will be larger than $7878\ kNm$. Therefore, the calculation scheme through 1D shell-spring-dashpot derived in Section 5.7 can approximate, to some extent, the torque capacity described by Georgiadis and Saflekou. Additionally, its tendency to overestimate the actual torque is shown here that is similar with the comparison against the FE model.

Comparison with an experiment by Stoll as described by Guo and Randolph

Figures and tables in Appendix E are shown for the second comparison with the torque capacity of a so-called pile $A-3$ tested by Stoll within the case study of Guo and Randolph. The system parameters are summarized in Table E.1 from which the soil shear modulus is assumed as $G = \frac{3\times1.38\times10^6}{2\times(1+0.4)} \approx 1.48 \times 10^6 Pa$ due to the use of standard penetration test (SPT) test to investigate the soil properties. Similarly with the previous comparison, static analysis is assumed. Only a single A-FRF is used, since the decaying function approaches zero near the pile tip from the first plot. The torque capacity of $T_o = 53\ kNm$, which overestimates 1.8 times the torque capacity of pile $A-3$ stated by Guo and Randolph $T_{o,GR} = 29\ kNm$. It is the third times that the overestimation is recorded, which suggests a refinement to improve the accuracy of the analytical model.

The overestimation means that the proposed method needs to be improved to increase the accuracy. However, there are always uncertainties when dealing with soil, for example in this case, Guo and Randolph highlighted a range of possible correlation between the N_{SPT} values and the modulus elasticity of soil such as $E = 2.8N\ MPa$, $E = 4N\ MPa$, and $E = 7N\ MPa$. Even though overestima-

tion seems favorable for the purpose of monopile extraction, an almost twice overestimation seems unacceptable when dealing with larger diameter. The inaccuracy can be related to the fact that shorter embedded length than the first comparison is considered so that only one discrete layer is assumed. When a single layer is assumed, the difficulty in determining the optimum depth becomes significant. More experiment data is thus required to improve and validate the proposed scheme.

Restating the torque and the clamping force

With regard to the occurrence of stress jumps, the overestimation against the literature is similar with the one against the FE analysis. Since the overestimation is in the order of twice the torque capacity mentioned in the literature, which is much smaller than 100, the shear stress in the pile seems more plausible to be decisive. Since a shell structure assumes a uniform stress through the thickness and a stress continuity is assumed at the pile-soil interface, the soil shares the same shear stress as in the pile at the pile-soil interface. Therefore, it concludes that the current GDP shaker will be able to aid the monopile extraction if similar monopile dimensions are used for the field experiments with the expected value of circumferential force, torque, clamping force, and power of $f_o = 3.10 \times 10^4\, N$, $T_o = 1.55{\times}10^4\, Nm$, $N_o = 4.43{\times}10^4$, and $P_{ave} = 40\, W$, whereas the maximum value of $f_o = 9.34{\times}10^4\, N$, $T_o = 4.67 \times 10^4\, Nm$, $N_o = 1.33 \times 10^5$, and $P_{ave} = 387\, W$.

7.10. Questioning the displacement at the pile top

The tendency of overestimation of the analytical model[4] in terms of shear stresses is clear but not yet in terms of displacement. The displacement at the pile top is then discussed to examine the suitability of the analytical model to replace the FE model by taking an example from $FEA\, l_1$ and $Analytic\, l_1$ and indicated in Figure 7.11 and Table 7.6. Figure 7.11 shows that non-uniform displacement[5] is visible in the area close to the pile top. It seems have to do with the mode of vibration that is activated by the applied forcing frequency of $80\, Hz$. It can also be influenced by the initial stress due to the self-weight.

If Figure C.3 and C.4 in Appendix C are referred, the non-uniform distribution seems localized at the top. It can be the indication of imperfectly distributed force due to non-uniform meshing, which may increase the risk of local buckling. Since it resembles the actual condition where the non-uniform stress response due to non-uniform mass of the shaker appears, future research regarding the stress check to avoid local buckling at the pile top can be of interest.

From Table 7.6 shows that 9.6% difference of the real part of $Analytic\, l_1$ with respect to $FEA\, l_1$ and 100% difference is shown between the imaginary part. They will lead to large deviation when computing the average power P_{ave} due to the $\sin(\Phi)$ term. It is because the 1D shell-spring-dashpot cannot capture the mode of vibration in the r and θ direction due to the axial symmetric assumption. Since the modal analysis is not studied, it is recommended to apply the modal analysis technique in the future to further study the vibration modes to obtain better accuracy of the phase response at the pile top, thus the average power. It can be concluded that the analytical model that assumes steady state response cannot fully replace the 3D FE model.

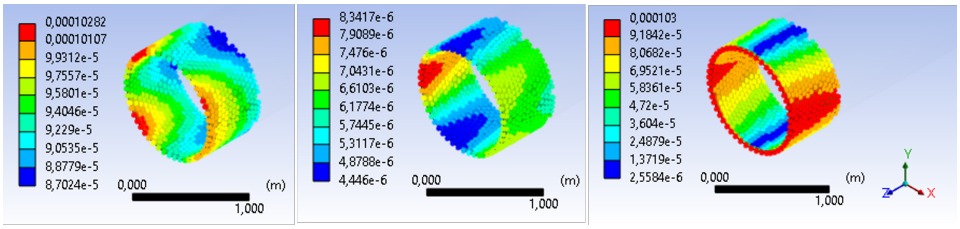

Figure 7.11: Displacement $FEA\, l_1$ versus $Analytic\, l_1$. From left to right: 1. $Re\,(U_\theta)$ 2. $Im\,(U_\theta)$ 3. $|U_\theta|$

[4] A better correlation is found through a more simplified analytical model that will be clear later on. It is found that in the latter model, the displacement amplitude agrees well with the FE model. However, the phase response cannot approximate the FE model too. Therefore, the same conclusion is made regarding the inability of the current analytical model to fully replace the FE model in order to obtain accurate estimate of power consumption.

[5] The average value of the displacement is used to compute the power in Section 7.7

–	f_{o,l_1}	$Re\,(U_\theta)$	$Im\,(U_\theta)$	$\lvert U_\theta \rvert$	Φ	$\sin(\Phi)$
–	N	m	m	m	rad	–
$FEA\,l_1$	3.53×10^4	9.83×10^{-5}	6.23×10^{-6}	9.85×10^{-5}	6.33×10^{-2}	0.063
$Analytic\,l_1$	3.53×10^4	8.90×10^{-5}	-1.20×10^{-14}	8.90×10^{-5}	-1.34×10^{-10}	-1.34×10^{-10}

Table 7.6: Displacement $FEA\,l_1$ versus $Analytic\,l_1$

7.11. Searching for a convergence through a more simplified analytical model

Even though the analytical shell-spring-dashpot model shows a comparable plot against the FE model, the spring reaction is found incorrect due to inconsistent unit. A correction is made in Section 5.7 together with a more simplifying assumption through the use of constant spring and neglecting the dashpot. The resulting shear stress compared to the results in the previous discussion is shown in Figure 7.12.

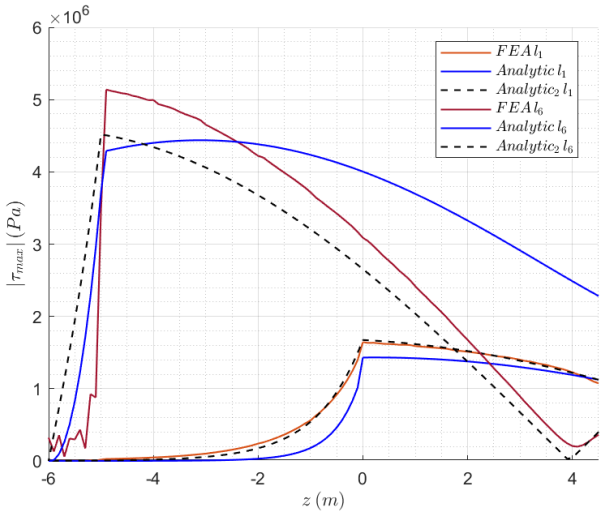

Figure 7.12: 3D FE analysis versus 1D shell-spring-dashpot versus 1D shell-spring model

While $Analytic_2\,l_1$ matches very well with the $FEA\,l_1$ visually, which corresponds to $\bar{\epsilon}_r = 0.22$ and $r_c = 0.99$, $Analytic_2\,l_6$ does not agree and underestimates $FEA\,l_6$ well with $\bar{\epsilon}_r = 0.77$ and $r_c = 0.92$. This means that the analytical model with a constant spring corresponds better to the FE analysis. Due to a good agreement when all the soil layers are in contact with the pile, it indicates that the effect of the linearly increasing soil stiffness is not captured well by the FE analysis. It is expected that the decaying shear stress in the FE analysis, due to the soil, is faster than the one that considers constant spring. The good agreement also indicates that the effect of material damping in the FE analysis seems negligible, which can lead to a further underestimation of the torque amplitude. On the other hand, the underestimation of the shear stress by $Analytic_2\,l_6$ seems due to the effect of soil mass around the failed pile-soil contact. However, it is not yet understood why that is the case. Moreover, $Analytic_2\,l_6$ is able to show the appearance of a node near the pile top similar to the shear stress shown by $FEA\,l_6$.

Since the torsional shell-spring model correlates well with the FE analysis results, an effort to check for a convergence on the torque amplitude is made. It is hypothesized that more soil discretization will lead to the convergence. It is indicated by first considering several cases in Figure 7.8 that assumes uniform discretization of the soil layers such as in simulation I, II, III, and $VIII$. As can be seen in Figure 7.13, the torque amplitudes[6] is shown in the descending order and reveals that the change of the amplitude becomes smaller as more soil layers are assumed, which infers a convergence. Since it

[6]Note that the torque is computed from the obtained force amplitude that has been divided by 100 due to the occurrence of the stress jump as discussed in the previous section

is not practicable to apply more layers in the 3D FE analysis, the analytical shell-spring model is used to check the convergence.

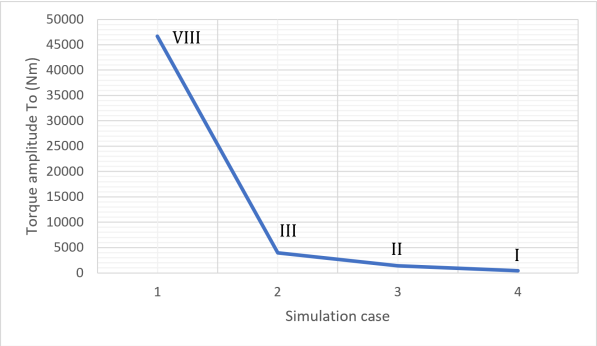

Figure 7.13: Torque amplitude of the cases with uniform soil discretization

A flowchart in Figure 7.14 is developed to show how an iteration is performed to check for the convergence of the torque amplitude following the gradual soil failure assumption. Note that the iteration assumes a decreasing depth of the spring similar to the FE model except that the presence of the soil around the failed pile-soil contact is not taken into account. Six layers are first assumed to verify the result against the FE analysis in simulation I and plotted in Figure 7.15.

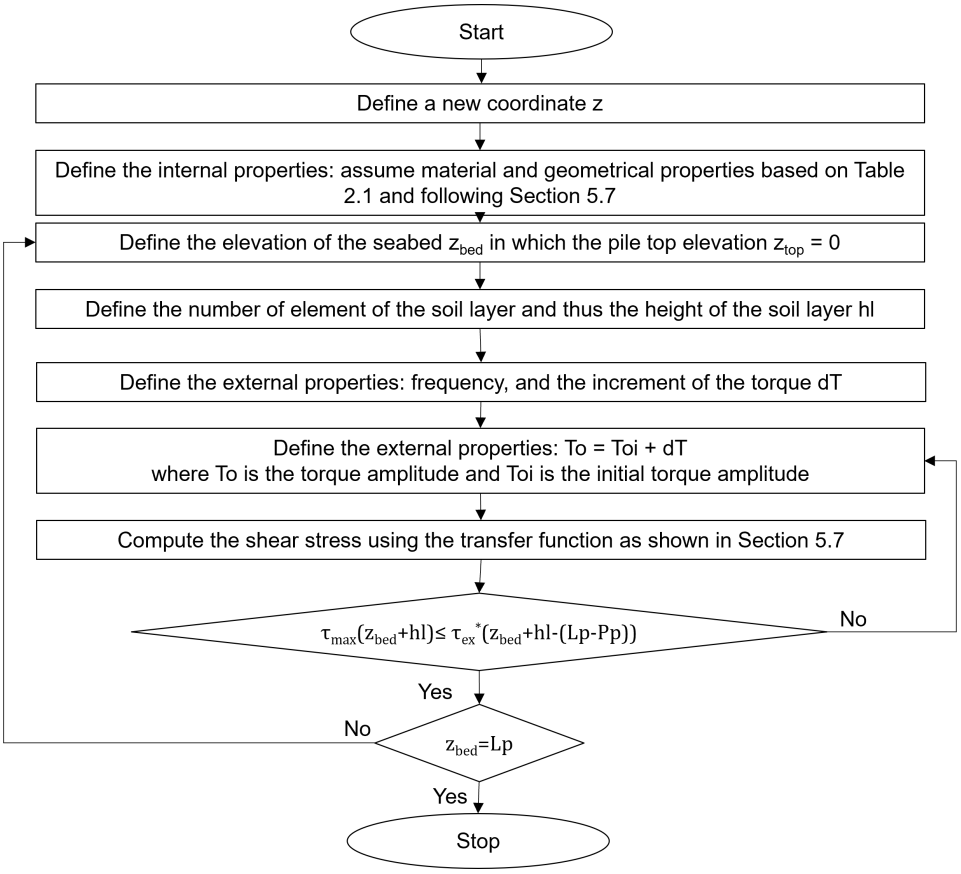

Figure 7.14: Flow chart to check for a convergence of the torque amplitude

Figure 7.15 illustrates a roughly similar envelope of the torque amplitudes to fail six soil layers gradually between the analytical shell-spring model and FE analysis. It shows that the first torque is almost identical and increases before eventually decreases starting from the fourth layer until the sixth

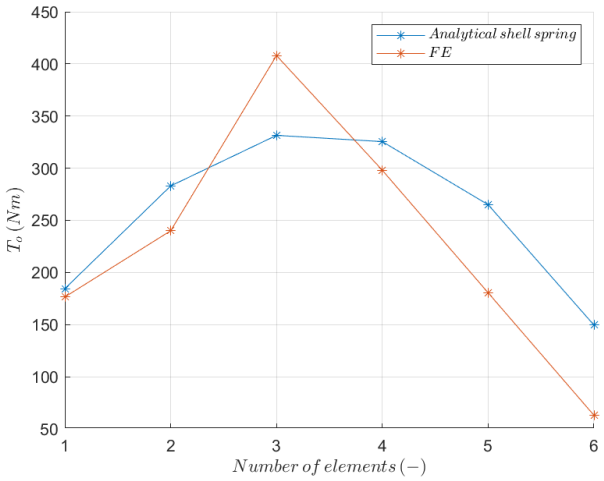

Figure 7.15: Torque according to the gradual soil failure assumption based on the shell-spring model and FE analysis assuming six discrete layers

layer. For this reason, the analytical model seems useful to study the convergence of the maximum torque amplitude when more soil elements are examined. Furthermore, the analytical model can be used to provide first approximation of the torque and clamping force for larger diameters. It should be noted that although the analytical and FE model seems not converge yet due to only six layers are examined, the analytical model underestimates the maximum torque of the FE analysis, which in this case in the order of 19%.

Further examination of more discrete layers, according to the analytical shell-spring model for a typical monopile dimensions with $D_o = 1\,m$, is plotted in Figure 7.16. It shows that the torque amplitude converges to $T_{o,2\times10^4} = 74.5\,Nm$ with 2×10^4 layers, which is 22% smaller than the previously found torque amplitude with six layers $T_{o,6} = 331.5\,Nm$. Therefore, it reinforces the statement regarding the applicability of the GDP shaker for a monopile extraction test with $D_o = 1\,m$. Additionally, it counteracts the proposed method to obtain the optimum depth because a much smaller soil thickness is now considered due to large number of discretization. Despite the modeling limitations that comes from a more simplification assumption than the 3D FE model, estimating the torque amplitude, thus the clamping force, for larger diameters is of interest because a convergence is obtained.

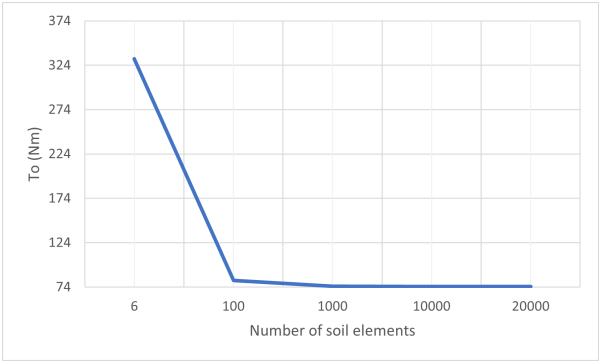

Figure 7.16: Convergence study of the torque amplitude for $D_o = 1\,m$

A first approximation of the torque and clamping force for larger diameters

In view of good correlation between the analytical shell-spring and FE model and the convergence that is found for $D_o = 1\,m$ in the earlier discussion, this thesis offers a first approximation of the torque amplitude and the clamping force for larger diameters such as $2\,m$, $3\,m$, $4\,m$, $5\,m$, $6\,m$[7]. While the

[7] $6\,m$ diameter is chosen by considering a moderate choice due to the so-called *soon to be decommissioned monopile* according

steel monopile geometries are determined by referring to Table 2.1, the steel material properties are as described in the early paragraph of Section 2.2. Finally, the soil spring and the failure criterion[8] assumes $c_2 = 360\,m/s$ and $\rho = 2022\,kg/m^3$ based on Section 3.5 and Table 3.1.

Figure 7.17 shows a first approximation of the required torque and clamping force during the torsional vibration of larger diameters with loading frequency of $80\,Hz$. Since the clamping force is directly proportional to the torque, a similar trend can be expected and therefore only the torque is plotted. It is found during the iteration, for larger diameters, that considering full depth of soil layer is impractical due to requiring large number of elements to obtain convergence near the pile tip and therefore only 85% of the embedded depth is assumed. Figure 7.17 illustrates that the torque increases non-linearly from the smallest $T_{o,D_o=1\,m} = 0.075\,kNm$ to the largest diameter $T_{o,D_o=6\,m} = 1205\,kNm$. Why this is the case is not fully understood and subject for further research.

A comparison to another study by Nielsen in the field of monopile extraction by axial vibratory hammer is performed to check whether the computation is going into the right direction or not to reduce the uncertainty. Even though the comparison is not precisely apples to apples and that the study is not validated against experiments, some similarities are evident such as the monopile diameter and sand unit weight, which are cited in Appendix F. Due to a suggestion by Stoll (Poulos, 1975) regarding *it may be easier and cheaper to determine the ultimate axial load capacity of a pile from a torsion loading test rather than a conventional axial load tests for friction piles in clay*, it is logical to argue that a smaller force that generates torque can fail the pile-soil interface compared to the same force that acts axially. Although the suggestion specifically mentions clay, it is somewhat neutralized by the word friction piles, which includes sand as well.

To further reduce the uncertainty, the analytical model is run for a frequency of a typical vibratory hammer $20\,Hz$. According to Nielsen, around $8.5\,MN$ of axial force is required to fail the pile-soil interface of a monopile with diameter $6\,m$ by means of a typical axial vibratory hammer. Comparing to Figure 7.17 is referred, only a couple of tangent force of $0.086\,MN$ each is required to generate the torque at the pile top, which indicates the superiority of the concept of torsional vibration within the GDP shaker framework in terms of magnitude of force. Since it agrees with the suggestion regarding a smaller force amplitude to generate torque than to produce an axial load, it indicates that the calculation is in the right direction. Finally, further research is recommended to validate the estimated torque.

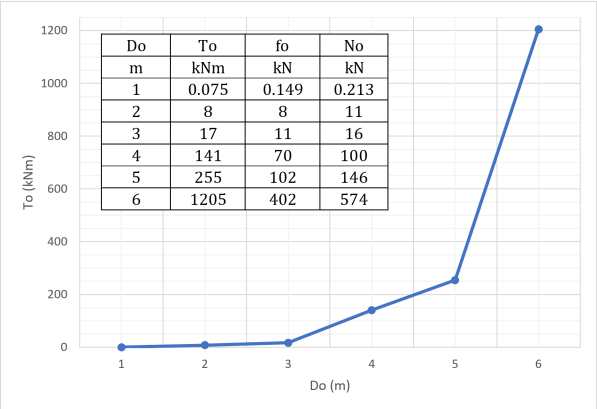

Figure 7.17: A first approximation of the torque and clamping force to twist the monopile for decommissioning

to the other research works (Meijer, 2022; Nielsen, 2022). This thesis will make a rough comparison to get insight into estimated force amplitude.

[8] A linearly increasing failure criterion is assumed without the application of limiting shear stress at a particular depth limit as often introduced in the standard computation of pile skin friction. It is intended to somewhat compensate the use of constant spring so that a conservative result is approximated.

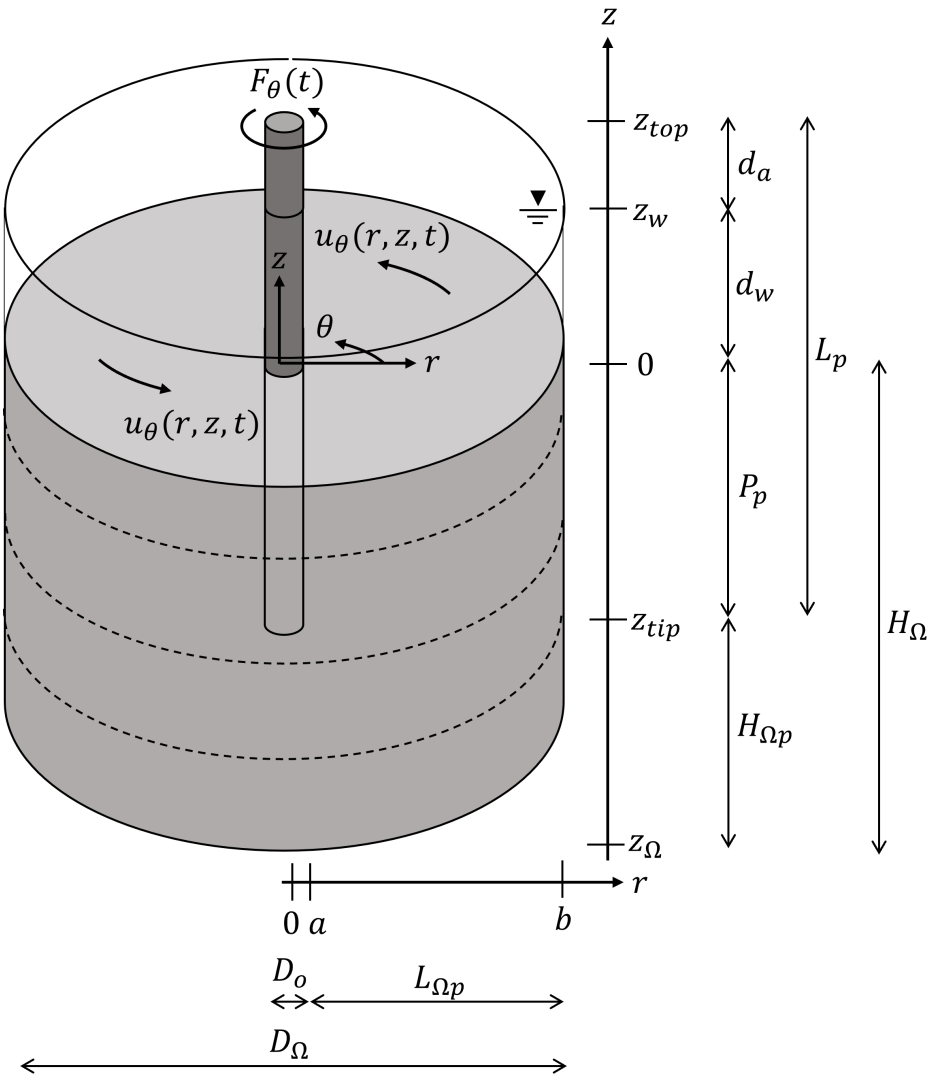

Figure 7.18: Nomenclature of the 3D model

8

Conclusions and recommendations for future research

8.1. Conclusions

The need for removing offshore wind monopiles completely from the seabed at the end of their lifetime is inevitable, particularly to allow redevelopment of offshore wind farms and a more environmentally and economically friendly approach than the cutting method. A potentially win-win solution through a novel GDP technique to extract monopiles is studied with a focus on modifying the shaker-pile interface. Answering a question regarding the amount of clamping force to fix the interface during the torsional vibration of the GDP shaker is fundamental before commissioning the technology in the offshore decommissioning market to guarantee its safety and economic feasibility. Therefore, this thesis seeks to understand the magnitude of the corresponding torque to slide the monopile over the soil before eventually arriving at the gripping force.

The linear elastic theory is implemented in the form of Navier Stokes equations to examine the idealized soil continuum as a solid and Love-Timoshenko equations to investigate the idealized monopile as a thin shell structure approximated by 3D FE method in Ansys Mechanical under a pre-stressed steady-state dynamic analysis. Soil failure criterion that resembles offshore soil in the North Sea is defined separately and does not enter the equation of motion within Ansys simulation. Static friction of sand following Mohr-Coulomb is the first focus of the study before the shear strength of clay. Then, gradual pile-soil interface failure is assumed on account of the failure criterion and generated shear stress.

1D analytical models within circular cylindrical coordinates are established to construct and comprehend the 3D FE analysis through the semi-infinite cavity-pile-soil, wave reflection, and finite cavity-pile-soil-dashpot subjected to torsional excitation with the help of Maple, Mathematica, Matlab, and Excel. A decaying amplitude behavior as the cylindrical torsional waves spread away from the pile is evident due to the Hankel function. Non-reflective boundaries to minimize the error within the 3D FE analysis are derived and implemented as frequency-dependent spring and dashpot coefficients for the outer r domain and frequency-independent dashpot coefficients for the outer z domain. It is found that the non-reflective coefficients work for small, moderate, and large soil domain sizes and have proven to excel the essential and natural boundaries to replace the infinite extent of the soil domain as a finite domain.

Care must be taken before choosing the soil domain size because the proposed non-reflective coefficients are based on 1D analysis. A thorough assessment of the domain size and non-reflective coefficients will lead to a reasonable approximation of force equilibrium at the pile-soil interface. Amplitude and phase response is checked to ensure correct interpretation during post-processing of the Ansys outputs. Material damping is incorporated in terms of viscous damping in the form of a damping ratio. A good agreement between the response in the FE analysis and analytical model under the plane strain assumption verifies the modeling of the geometrical and material properties, boundary/interface

conditions, meshing, and harmonic analysis in Ansys despite the discrepancy in the axial symmetry. Non-uniform hexahedral mesh with mid-side nodes is employed because it can better fill the cylindrical shape and grow in size with the increasing distance from the pile-soil interface compared to the tetrahedral one. Mesh convergence is achieved by a small change in the solution when assuming a uniformly distributed force along the monopile.

During the construction of the 3D FE model, it is found that the effect of the inner soil is considerably small, which confirms the plane strain cavity-pile-soil model. In terms of shear stress, while the 3D FE model with $free$-$free$ boundary at the top and bottom domain show correspondence with the plane strain cavity-pile-soil model, the one with the additional soil layer below the pile-soil system cancels the congruity. Therefore, the force equilibrium near the pile-soil interface is prioritized as the primary tool for examining the solution. Stress jumps are evident in the radial and longitudinal direction at the pile-soil interface due to material discontinuity. It also found that a fixed boundary at the bottom of the additional layer is not recommended to be used due to deviating the force equilibrium near the pile-soil interface.

An element size of $0.04\,m$ is applied around the pile-soil interface after changes in the solution due to soil layering at the pile-soil interface arise. The initial stresses due to the constant gravitational acceleration are delivered without and with the unsupported length of the monopile above the soil surface through static analysis following the hydrostatic pressure distribution of the soil vertical stress. Unrealistic tension in the soil continuum becomes significant due to perfectly bonded contact at the pile-soil interface when the monopile above the seabed is added. Six discrete layers are assumed to explore simulation possibilities regarding the gradual pile-soil interface failure due to the torque excitation at the pile top.

As a result of simulation possibilities, the resulting force amplitudes at the pile top to fail the discrete soil layers can be grouped in several bins, which leads to the need for probabilistic sense to grasp the pattern. It is found that the pile-soil interface failure tends to occur in the neighborhood of zero shear stress as described by the expected value of the compiled amplitudes through the assumption of Weibull distribution. Even though the mesh convergence is realized in the previous steps, the force amplitudes are still questionable due to the development of stress jump in the order of 100 times difference between the shear stress in the pile and in the soil close to the pile-soil interface. It leads to a possible error of the estimated power consumption in the order of squared difference coming from the product of force and velocity amplitudes and eventually leads to the prediction of insufficient GDP shaker's operating power.

A 1D shell-spring-dashpot model is developed to question the shear stress in the pile. It is found that there is a good correlation between the analytical and FE model in terms of shear stress in z-direction, which verifies the linear elastic and steady-state assumption of the FE model. A better consistency between the two is noticeable when a complete pile-soil contact from the pile tip to the soil surface is assumed compared to when the pile-soil connection in the first top layers failed, indicating the effect of soil mass around the detached pile-soil contact. The analytical model shows that the decaying shear stress in the soil is due to the Airy function, which decays faster when the soil is stiffer.

Comparison against the literature is made to question further the stress jumps and to possibly promote the improvement of the 1D shell-spring-dashpot model with the proposed calculation procedures, which indicates that the analytical model can predict the range of the torque capacity due to Georgiadis and Saflekou. The analytical model overestimates the torque capacity described by Guo and Randolph based on a test by Stoll. Concerning the occurrence of stress jumps, the overestimation against the literature is similar to the one against the FE analysis. Since the overestimation is in the order of twice the torque capacity mentioned in the literature, which is much smaller than 100, and that a uniform stress through thickness of shell structures is assumed, the shear stress in the pile seems more plausible to be decisive. Therefore, it concludes that the current GDP shaker will be able to aid the monopile extraction if similar monopile dimensions are used for an onshore field experiment with the expected value of the circumferential force, torque, clamping force, and power of $f_o = 3.10 \times 10^4\,N$, $T_o = 1.55 \times 10^4\,Nm$, $N_o = 4.43 \times 10^4$, and $P_{ave} = 40\,W$, whereas the maximum value of $f_o = 9.34 \times 10^4\,N$, $T_o = 4.67 \times 10^4\,Nm$, $N_o = 1.33 \times 10^5$, and $P_{ave} = 387\,W$ at the frequency of $80\,Hz$.

A seemingly better interpretation of the torque amplitude from the obtained simulation is due to a convergence check. It is found that through an iteration with the help of a more simplified analyt-

ical shell-spring model, the torque amplitudes converge into one value when more soil elements are considered in the order of 2^4 elements by considering only 85% of the soil depth due to numerical implementation. The estimated torque amplitude is now $T_o = 74.5\,Nm$ and the clamping force $N_o = 213\,N$. A first approximation of the torque amplitude, thus the clamping force, is then proposed to get the most out of the analytical model for larger diameters such as $D_o = 6\,m$ from which $T_{o,D_o=6\,m} = 1.205\,MNm$ and $N_{o,D_o=6\,m} = 0.574\,MN$. It is found that the required torque, thus the clamping force, increases nonlinearly with the monopile diameter. A first check regarding the required force amplitude to generate the torque is made by comparing it to another study about monopile extraction using axial vibratory hammer. Following a suggestion from a literature regarding the torsional response a pile, the check satisfies the suggestion that indicates the advantages of using torsional vibration compared to its axial counterpart.

8.2. Recommendations

The workflow to determine the torque amplitude and its corresponding clamping force through the FE method in Ansys is now clear. The first recommendation is to exercise the workflow to create a benchmark FE model by calibrating the model against laboratory experiments that consider the shaker's mass. The calibration process should help to evaluate the model assumptions such as the pile flexibility and the soil spring model. Force equilibrium checks through applying a fictitious force uniformly distributed along the pile should be prioritized so that an entire domain is constructed immediately. At the same time, the FE model is improved by considering soil plasticity or reduced spring coefficient either by putting a new constitutive model in the equation of motion or by perturbing the linear analysis within a small domain. Modifying the frequency-dependent non-reflective boundary to analyze a few different frequencies is suggested to make references. Secondly, a refinement of a simplified analytical model such as through the 1D shaker-shell-spring with the proposed iteration method is suggested to be developed to compete with the FE model by taking advantage of the axisymmetric loading assumption.

The improvement of the analytical model should consider soil plasticity and vibrator's mass throughout the gradual soil failure simulation. The analytical model is thus calibrated against the established benchmark to see the location and magnitude of the displacement and stress field at which the important outputs deviate and make compromises by considering the trade-offs. Modal analysis is recommended as the replacement of or addition to the steady state analysis if a better estimate of average power consumption is desired at the modeling level. When the analytical model can approximate the FE model well, finding the optimum forcing frequency through the analytical model is suggested. The A-FRF derived at the end of the chapter analytical model can be used as a first approximation to determine the optimum frequency. Through discrete soil layers, insight from probability theory such as the use of extreme value distribution is useful to indicate the likelihood of a force amplitude to fail the soil layers, thus the corresponding clamping force, especially when larger diameters and deeper soil layers are considered. Having the optimum forcing frequency and amplitude, an offshore field experiment is recommended to validate the model with larger diameters.

A

Monopiles dimensions

Two geometrical data of installed monopiles in Europe, which are collected and analyzed by other researchers (Meijer, 2022; Negro et al., 2017), are adopted[1]. It is deemed of secondary importance to criticize the way they are analyzed since a reasonable match, in terms of the relationship against the diameter, has been found between the two.

Wind farm	ISO 3166-2 country code	Project	Turbine	Minimum water depth	Maximum water depth	Diameter	Length	Driving length	Mass
-	-	MW	MW	m	m	m	m	m	tonne
Belwind	BE	165	3	15	24	5	72	48	550
Horns Rev 2	DK	209.3	2.3	9	17	3.9	40	23	280
Horns Rev 1	DK	160	2	6	14	4	42	28	230
Samsø	DK	23	2.3	10	13	4.5	45	32	300
Anholt	DK	399.6	3.6	15	19	5	54	35	630
EnBW Baltic 1	DE	48.3	2.3	16	19	4.3	37	18	215
Borkum Riffgrund 1	DE	312	4	23	29	5.9	66	37	700
Amrumbank West	DE	302	3.775	20	25	6	70	45	800
DanTysk	DE	288	3.6	21	31	6	65	34	730
Riffgat	DE	108	3.6	18	23	6	70	47	720
Lely	NL	2	0.5	5	10	3.7	30	20	89
Prinses Amalia	NL	120	2	19	24	4	54	30	320
Egmond aan Zee	NL	108	3	18	18	4.6	60	42	250
Bockstigen	SE	2.75	0.55	6	6	2.1	21	15	43
Utgrunden 1	SE	10.5	1.5	7	10	3.65	33.7	23.7	165
North Hoyle	GB	60	2	7	11	4	25	14	250
Kentish Flats	GB	90	3	5	5	4	38	33	247
Scroby Sands	GB	60	2	5	10	4.2	42	32	200
Robin Rigg	GB	174	3	4	13	4.3	35	22	310
Rhyl Flats	GB	90	3.6	6	12	4.7	40	28	235
Barrow	GB	90	3	15	20	4.75	60	40	530
Gunfleet Sands	GB	172.8	3.6	0	15	5	50	35	423
Teesside	GB	62.1	2.3	8	16.5	5	48	31.5	160
Burbo Bank	GB	90	3.6	2	8	5	52	44	400
Sheringham Shoal	GB	316.8	3.6	17	22	5.2	61	39	530
Lincs	GB	270	3.6	8.5	16	5.2	48	31.7	480
Gwynt Môr	GB	576	3.6	12	28	6	70	42	700
Greater Gabbard	GB	504	3.6	20	32	6	60	28	700
Walney Phase 2	GB	183.6	3.6	24	30	6	68	38	805
London Array	GB	630	3.6	0	25	7	85	60	650

Figure A.1: $Data2$ (Negro et al., 2017)

[1] On $Data1$, the water depth is taken as the maximum in the range. Two unavailable information in $Data2$ on the bottom diameter is assumed to be equal the top diameter.

Wind farm	ISO 3166-2 country code	Capacity	Year	Water depth	Length	Penetration depth	Mass	Bottom diameter	Top Diameter	TP connection
-	-	MW	-	m	m	m	mt	m	m	-
Horns Rev I	DK	80 x 2.0	2002	20	60	28	139	4.20	4.20	Grout
North Hoyle	GB	30 x 2.0	2003	12	53	41	275	4.00	4.00	Grout
Scroby Sands	GB	30 x 2.0	2004	8	46	30	200	4.20	4.20	Integrated
Kentish flats	GB	15 x 3.3	2005	5	38	33	247	4.50	4.30	Grout
Princes Amalia	NL	36 x 3.0	2006	24	54	30	320	4.00	4.00	Grout
Egmond aan Zee	NL	60 x 2.0	2006	18	60	30	250	4.60	4.60	Grout
Barrow	GB	90 x 3.0	2006	23	61	38	452	4.80	4.80	-
Burbo bank	GB	25 x 3.6	2007	6	37	31	212	5.00	5.00	Grout
Horns Rev II	DK	91 x 2.3	2009	17	40	23	210	3.90	3.90	Grout
Lynn and Inner Dowsin	GB	54 x 3.6	2009	11	36	25	225	4.70	4.70	Grout
Rhyl flats	GB	25 x 3.6	2009	12	40	28	235	4.70	4.70	Grout
Belwind	BE	50 x 3.3	2010	36	65	29	550	5.00	4.00	Grout
GF Sands 1 & 2	GB	48 x 3.6	2010	15	50	37	423	***4.70***	4.70	Grout
Thanet	GB	100 x 3.0	2010	25	60	35	371	5.10	4.90	-
Baltic 1	DE	21 x 2.3	2011	19	37	18	215	4.30	4.30	Grout
Sheringham Shoal	GB	88 x 3.6	2012	24	50	26	500	5.70	4.70	Grout
Greater Gabbard	GB	140 x 3.6	2012	32	68	30	676	6.30	5.10	Grout
Lincs	GB	75 x 3.6	2013	15	49	30	340	5.20	4.70	Grout
Teesside	GB	27 x 2.3	2013	15	51	36	352	4.60	3.90	-
Anholt	DK	111 x 3.6	2013	19	55	36	630	5.35	4.70	Grout
London Array	GB	175 x 3.6	2013	25	68	43	650	5.70	4.70	Grout
West of Duddon Sands	GB	108 x 3.6	2014	24	59	35	516	6.00	5.60	Grout
Meerwind Sud/Ost	DE	80 x 3.6	2014	26	64	38	680	5.50	5.50	Grout
Northwind	BE	72 x 3.0	2014	28	66	38	420	5.20	4.20	Grout
Riffgat	DE	30 x 3.6	2014	24	70	40	720	6.30	4.70	Grout
Luchterduinen (=hk zuid)	NL	150 x 4.0	2015	36	65	29	560	5.00	4.50	Integrated
EnBW Baltic 2	DE	80 x 3.6	2015	44	74	30	832	6.50	5.00	-
Borkum Riffgrund I	DE	78 x 4.0	2015	29	66	30	700	5.90	5.90	-
DanTysk	DE	80 x 3.6	2015	31	63	32	575	6.00	6.00	Grout SK
Gwynt y mor	GB	160 x 3.6	2015	33	70	37	688	6.50	4.60	Grout
Amrumbank West	DE	80 x 3.6	2015	25	60	30	700	6.00	6.00	BF
Humber Gateway	GB	73 x 3.0	2015	15	60	45	650	4.90	4.50	BF
Gemini	NL	43 x 3.0	2015	24	73	49	800	7.00	5.50	Grout
Gode Wind 1&2	DE	97 x 6.0	2016	33	67	34	939	7.50	5.70	Grout
Galloper	GB	58 x 6.0	2016	36	85	49	1237	7.50	6.30	-
Dudgeon	GB	67 x 6.0	2017	25	45	20	840	7.00	6.30	Grout
Sandbank	DE	72 x 4.0	2017	33	70	37	1083	6.80	5.50	-
Nordsee One	DE	54 x 6.2	2017	29	70	41	900	***5.50***	5.50	BF
Veja Mate	DE	67 x 6.0	2017	41	84	43	1300	8.70	6.50	BF
Nobelwind	BE	50 x 3.3	2017	30	77	47	800	6.80	4.50	BF
Walney extension	GB	47 x 7.0	2018	37	73	36	970	8.40	6.20	-
Arkona	DE	60 x 6.0	2018	37	81	40	1200	7.75	7.00	BF
Rampion	GB	116 x 3.45	2018	41	73	44	647	6.50	5.75	BF
Rentel	BE	44 x 7.0	2018	36	83	47	1250	8.00	5.60	Grout
Horns Rev III	DK	49 x 8.3	2019	20	50	30	610	6.50	6.50	-
Albatros	DE	16 x 7.0	2019	40	71	31	1081	8.00	6.00	-
Hohe See	DE	71 x 7.0	2019	40	71	31	1070	8.00	6.00	-
Merkur	DE	66 x 6.0	2019	33	73	35	970	7.80	6.00	BF
Deutsche Bucht	DE	33 x 8.2	2019	40	78	38	1100	8.00	6.50	-
Hornsea One	GB	174 x 7.0	2020	30	65	35	800	8.10	6.00	BF
Borssele 1&2	NL	94 x 8.0	2020	36	76	40	1188	8.30	6.50	-
Northwester 2	BE	23 x 9.5	2020	40	82	42	1000	8.00	6.50	-
Seamade	BE	58 x 8.4	2020	38	80	42	1040	8.00	6.30	BF
Triton Knoll	GB	90 x 9.5	2021	18	50	32	537	6.90	6.50	BF
Kriegers Flak	DK	72 x 8.4	2021	30	65	35	810	6.00	6.00	BF
Borssele 3&4	NL	77 x 9.5	2021	38	85	47	1280	7.40	6.50	Integrated
Hornsea Two	GB	165 x 8.4	2022	40	77	37	1285	9.50	6.50	-
Dogger bank A & B	GB	190 x 13	2023	35	50	15	1200	8.60	8.30	BF

Figure A.2: $Data1$ (Meijer, 2022)

B

Equation of motion

Equations of dynamic equilibrium in curvilinear coordinates

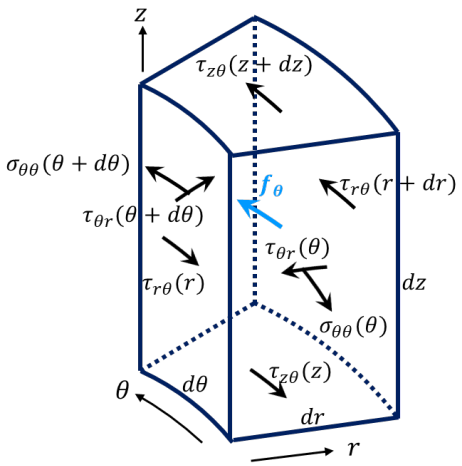

Figure B.1: Equilibrium of forces in θ-direction of a solid element cut

According to Newton's second law, the dynamic force equilibrium of an element cut of a solid in Figure B.1 consist of the internal force due to the material stiffness, external body force, and inertia force. Assuming no energy loss, in the circumferential direction θ, in terms of stresses, the equilibrium can be described as

$$\begin{aligned} -\sigma_{\theta\theta}(\theta)\cos\frac{d\theta}{2}\,dr\,dz + \sigma_{\theta\theta}(\theta+d\theta)\cos\frac{d\theta}{2}\,dr\,dz - \tau_{r\theta}(r)\,r\,d\theta\,dz + \tau_{r\theta}(r+dr)\,(r+dr)\,d\theta\,dz \\ \tau_{\theta r}(\theta)\,dr\,dz\sin\frac{d\theta}{2} + \tau_{\theta r}(\theta+d\theta)\,dr\,dz\sin\frac{d\theta}{2} - \tau_{z\theta}(z)\frac{r\,d\theta+(r+dr)d\theta}{2}dr \\ +\tau_{z\theta}(z+dz)\frac{r\,d\theta+(r+dr)\,d\theta}{2}dr + f_\theta\,r\,d\theta\,dr\,dz = \rho\,r\,d\theta\,dr\,dz\,\frac{\partial^2 u_\theta}{\partial t^2} \end{aligned} \tag{B.1}$$

Taking the Taylor Series Expansion (TSE) up to the first order (*i.e.* neglecting non-linear terms) (Metrikine & Vrouwenvelder, 2021) will lead to $\sigma_{\theta\theta}(\theta+d\theta) \approx \sigma_{\theta\theta}(\theta) + \frac{\partial\sigma_{\theta\theta}}{\partial\theta}d\theta$, $\sigma_{r\theta}(r+dr) \approx \sigma_{r\theta}(r) + \frac{\partial\sigma_{r\theta}}{\partial r}dr$, $\tau_{\theta r}(\theta+d\theta) \approx \tau_{\theta r}(\theta)+\frac{\partial\tau_{\theta r}}{\partial\theta}d\theta$, $\tau_{z\theta}(z+dz) \approx \tau_{z\theta}(z)+\frac{\partial\tau_{z\theta}}{\partial z}dz$. This is valid for small displacement assumption. Accordingly, $\sin d\theta \approx d\theta$, $d\theta^2 \approx 0$, $dr^2 \approx 0$. Thus, (B.1) reduces to

$$\frac{\partial \sigma_{\theta\theta}}{\partial \theta}\, d\theta\, dr\, dz + \tau_{r\theta}\, dr\, d\theta\, dz + \frac{\partial \tau_{r\theta}}{\partial r}\, r\, dr\, d\theta\, dz + \tau_{\theta r}\, dr\, dz\, d\theta + \frac{\partial \tau_{z\theta}}{\partial z}\, dz\, r\, d\theta\, dr + f_\theta\, r\, d\theta\, dr\, dz = \rho\, r\, d\theta\, dr\, dz\, \frac{\partial^2 u_\theta}{\partial t^2} \tag{B.2}$$

Due to the balance of moment about the centre point (Timoshenko & Goodier, 1951), $\tau_{\theta r} = \tau_{r\theta}$. Thus, (B.1) reduces further to

$$\frac{\partial \sigma_{\theta\theta}}{\partial \theta}\, d\theta\, dr\, dz + 2\tau_{r\theta}\, dr\, d\theta\, dz + \frac{\partial \tau_{r\theta}}{\partial r}\, r\, dr\, d\theta\, dz + \frac{\partial \tau_{z\theta}}{\partial z}\, dz\, r\, d\theta\, r + f_\theta\, r\, d\theta\, dr\, dz = \rho\, r\, d\theta\, dr\, dz\, \frac{\partial^2 u_\theta}{\partial t^2} \tag{B.3}$$

Dividing (B.3) by $r\, d\theta\, dr\, dz$ yields the following equilibrium equations (Graff, 1975)[1].

$$\frac{\partial \tau_{r\theta}}{\partial r} + \frac{1}{r}\frac{\partial \sigma_{\theta\theta}}{\partial \theta} + \frac{\partial \tau_{\theta z}}{\partial z} + \frac{2}{r}\tau_{r\theta} + f_\theta = \rho \frac{\partial^2 u_\theta}{\partial t^2} \tag{B.4}$$

where the normal stresses σ, shear stresses τ, and displacement u, are functions of space r, θ, z, and time t.

Strain-displacement relationship derived from the geometry

The shear strains, in θ direction, as a result of small changes of displacement can be written as (Wierzbicki, 2022)

$$\begin{aligned} \gamma_{r\theta} &= \frac{1}{r}\frac{\partial u_r}{\partial \theta} + \frac{\partial u_\theta}{\partial r} - \frac{u_\theta}{r} \\ \gamma_{\theta z} &= \frac{1}{r}\frac{\partial u_z}{\partial \theta} + \frac{\partial u_\theta}{\partial z} \end{aligned} \tag{B.5}$$

B.1. Torsional motion under a plane strain assumption

Equilibrium equation and strain-displacement relationship

By assuming a plane strain motion, the displacement in z are assumed to be uniform. This is reasonable by also assuming that the excitation from the vibrator is uniformly distributed along r and θ. The system is thus axisymmetric. The change of strains in θ and z direction are thus zero (*i.e.* $\frac{\partial}{\partial \theta} = 0$ and $\frac{\partial}{\partial z} = 0$). For that reason, (B.4) and the first of (B.5) reduces to

$$\frac{\partial \tau_{r\theta}}{\partial r} + \frac{2}{r}\tau_{r\theta} + f_\theta = \rho \frac{\partial^2 u_\theta}{\partial t^2} \tag{B.6}$$

$$\gamma_{r\theta} = \left(\frac{\partial u_\theta}{\partial r} - \frac{u_\theta}{r} \right) \tag{B.7}$$

Stress-strain relationship

Following Hooke's law, the force to restore every springing body to its natural position is proportional to the distance it is removed from. This law holds also when the restoring force is termed as a stress and the distance as a strain. Two possible deformations, which are independent to each other, can be described as elongations and distortions (*i.e.* normal and shear strain). In this particular case of torsional motion under plane strain assumption, the shear strain reads

[1] There is a slight difference in the notation.

$$\gamma_{r\theta} = \frac{1}{G}\tau_{r\theta} \tag{B.8}$$

where the shear modulus G is defined as

$$G = \frac{E}{2(1+\nu)} \tag{B.9}$$

where E is the Young's modulus and ν is the Poisson's ratio (Howell, 2017; Timoshenko & Goodier, 1951). It should be noted that the material constants (E, ν, and G) are due to the linear, homogeneous, and isotropic material assumption. Substituting (B.7) into (B.8) gives

$$\tau_{r\theta} = G\left(\frac{\partial u_\theta}{\partial r} - \frac{u_\theta}{r}\right) \tag{B.10}$$

Equation of torsional motion

Substituting (B.10) into (B.6) leads to the torsional equation of motion in terms of displacement.

$$G\left(\frac{\partial^2 u_\theta}{\partial r^2} + \frac{1}{r}\frac{\partial u_\theta}{\partial r} - \frac{u_\theta}{r^2}\right) + f_\theta = \rho\frac{\partial^2 u_\theta}{\partial t^2} \tag{B.11}$$

In the absence of external body force (*i.e.* $f_\theta = 0$), (B.11) can also be written as

$$\frac{\partial^2 u_\theta}{\partial r^2} + \frac{1}{r}\frac{\partial u_\theta}{\partial r} - \frac{1}{r^2}u_\theta = \frac{1}{c_2^2}\frac{\partial^2 u_\theta}{\partial t^2} \tag{B.12}$$

where the displacement in the θ direction is a function of radius and time $u_\theta(r,t)$, and $c_2 = \sqrt{\frac{G}{\rho}}$ is the shear wave speed.

B.2. One-dimensional torsional motion propagating in z-direction

If no stresses in r and θ-direction is now assumed, the torsional motion will propagate in z-direction. Following this assumption, and in the absence of body force, (B.4) and the second of (B.5) reduces to

$$\frac{\partial \tau_{\theta z}}{\partial z} = \rho\frac{\partial^2 u_\theta}{\partial t^2} \tag{B.13}$$

$$\gamma_{\theta z} = \frac{\partial u_\theta}{\partial z} \tag{B.14}$$

Stress-strain relationship Considering only the shear strain in z,

$$\gamma_{\theta z} = \frac{1}{G}\tau_{\theta z} \tag{B.15}$$

Therefore,

$$\tau_{\theta z} = G\frac{\partial u_\theta}{\partial z} \tag{B.16}$$

Equation of torsional motion

Substituting (B.16) into (B.13) leads to the torsional equation of motion in terms of displacement that propagates in z-direction.

$$\frac{\partial^2 u_\theta}{\partial z^2} = \frac{1}{c_2^2}\frac{\partial^2 u_\theta}{\partial t^2} \tag{B.17}$$

C

Snips of Ansys simulation

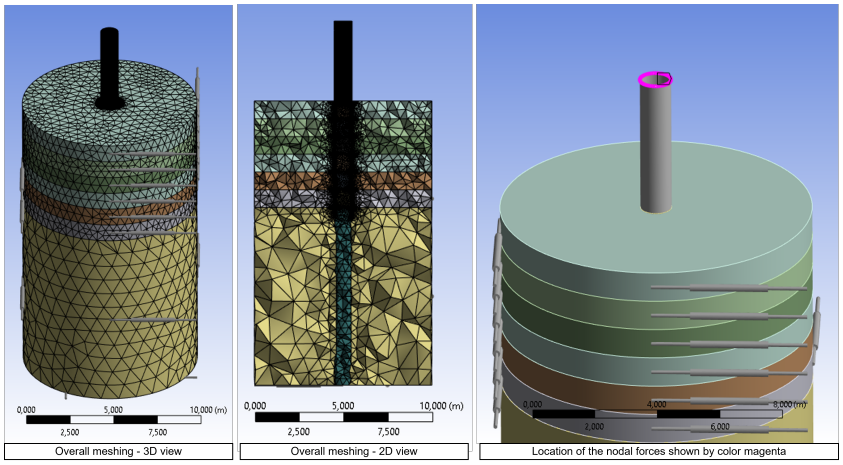

Figure C.1: Pile-soil meshing and location of loading input

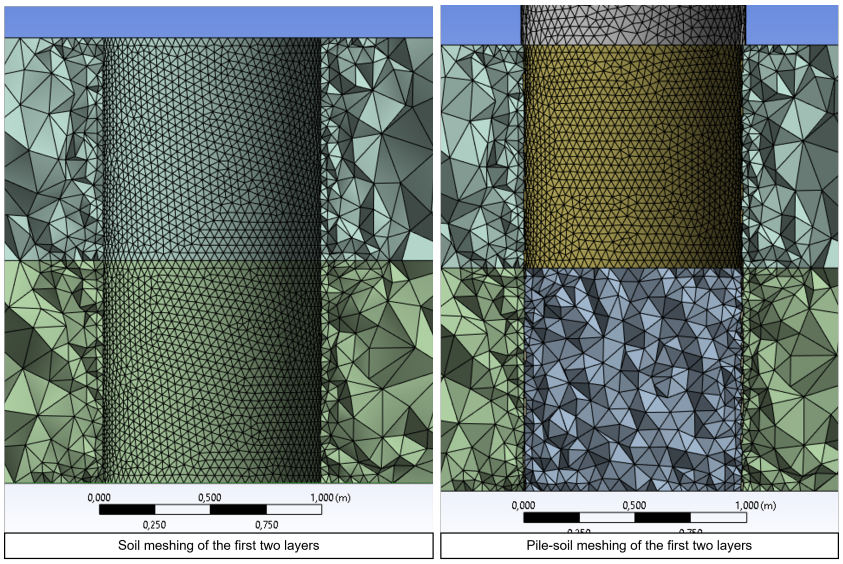

Figure C.2: Pile-soil meshing of the first two layers in 2D $r - z$ plane

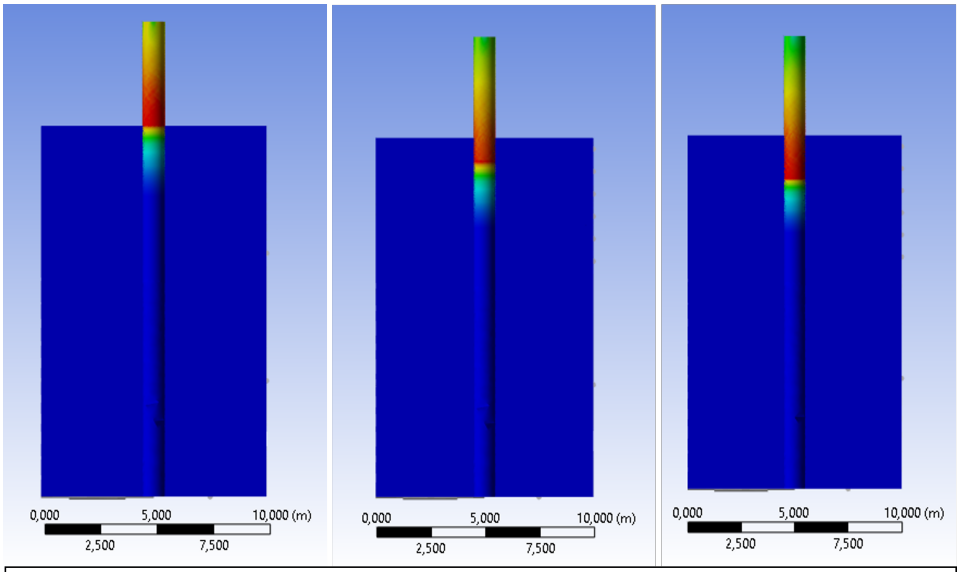

Normalized shear stress distribution with rainbow scale.
Depth of the pile-soil contact from the pile tip (from left to right pictures): 6 m, 5 m, and 4 m

Figure C.3: Normalized shear stress amplitude distribution with different depth of the pile-soil contact in 2D $r - z$ plane (1/2)

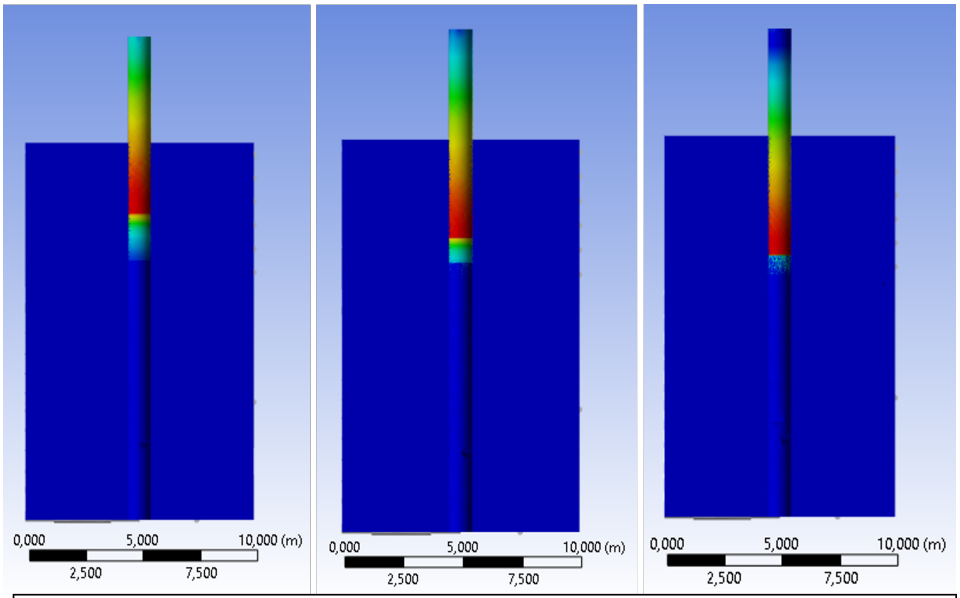

Normalized shear stress distribution with rainbow scale.
Depth of the pile-soil contact from the pile tip (from left to right pictures): 3 m, 2 m, and 1 m

Figure C.4: Normalized shear stress amplitude distribution with different depth of the pile-soil contact in 2D $r - z$ plane (2/2)

D

Comparison with a prediction by Georgiadis and Saflekou for an offshore steel pipe pile

[1]

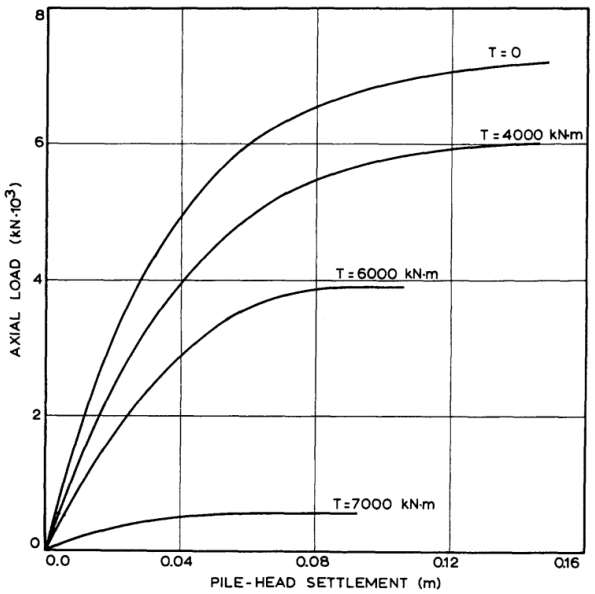

Figure D.1: Predicted offshore pile response (Georgiadis & Saflekou, 1990)

D_o	L_p	wt	s_u	ω
m	m	m	kPa	rad/s
2.1	50	28×10^{-3}	20	0

Table D.1: Geometrical and material properties discussed by Georgiadis and Saflekou

[1] z coordinate is shifted such that $z_{tip} = 0.0\,m$ (see Figure 7.18) for computation convenience

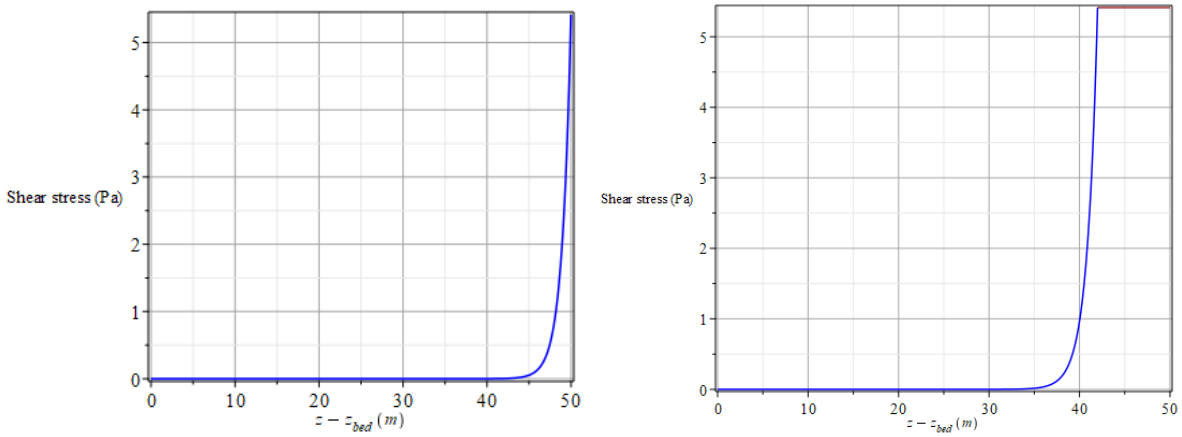

(a) TF for $z_{bed} = 49.99\,m$ (b) TF for $z_{bed} = 42\,m$

Figure D.2: Transfer function of the 1^{st} and 2^{nd} layer failure

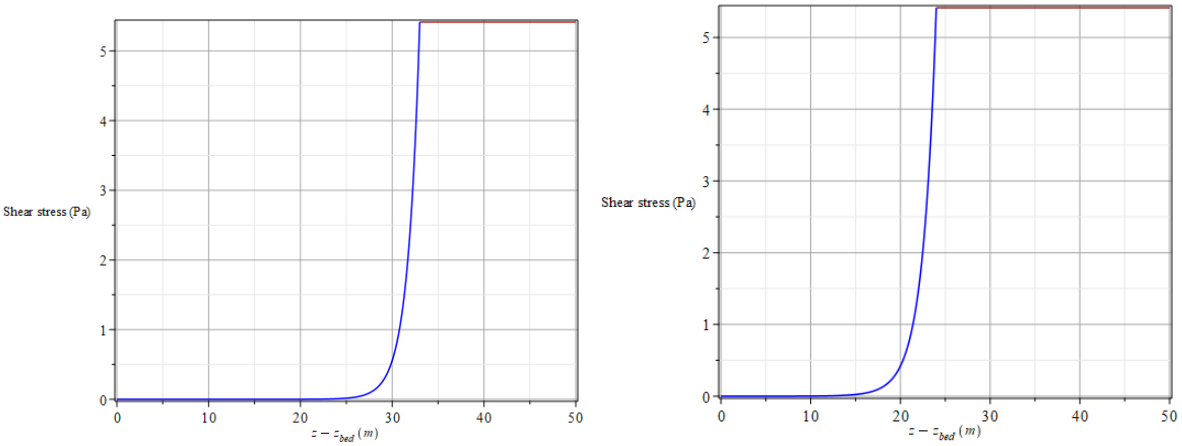

(a) TF for $z_{bed} = 33\,m$ (b) TF for $z_{bed} = 24\,m$

Figure D.3: Transfer function of the 3^{rd} and 4^{th} layer failure

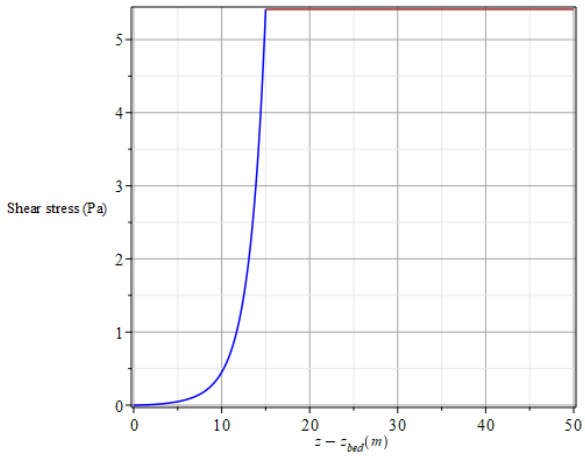

(a) TF for $z_{bed} = 15\,m$

z	Su	τmax	τmax/Su	fo	To
m	Pa	Pa	-	N	kNm
-7	20000	20057	1.003	2253502	2366
-8	20000	20010	1.001	5408404	5679
-9	20000	19920	0.996	12872001	13516
					7187
-16	20000	20000	1.000	2843386	2986
-17	20000	20093	1.005	6242200	6554
-18	20000	20001	1.000	13424206	14095
					7878
-25	20000	20004	1.000	1256438	1319
-26	20000	20000	1.000	2461487	2585
-27	20000	20000	1.000	4760320	4998
					2967
-34	20000	20050	1.002	489562	514
-35	20000	20000	1.000	844132	886
-36	20000	20000	1.000	1432932	1505
					968
-43	20000	20000	1.000	168959	177
-44	20000	20000	1.000	263315	276
-45	20000	20000	1.000	419498	440
					298

(b) The proposed computation scheme

Figure D.4: TF for $z_{bed} = 15\,m$ and the proposed computation scheme

E

Comparison with an experiment by Stoll discussed by Guo and Randolph for a steel pipe pile

[1]

D_o	L_p	wt	N	E	μ	ω
m	m	m	N_{SPT}	MPa	$-$	rad/s
0.273	17.4	6.3×10^{-3}	$1.38z$	$3N$	0.4	0

Table E.1: Geometrical and material properties discussed by Guo and Randolph

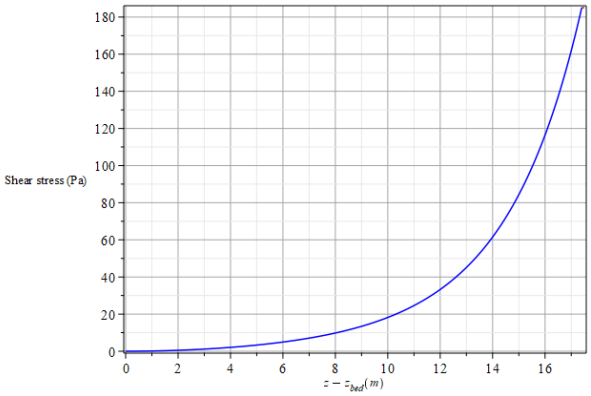

(a) Transfer function of the 1^{st} layer failure

z	τex*	τmax	τmax/Su	fo	To
m	Pa	Pa	-	N	kNm
-15.4	87135	87136	1.000	171528	23
-15.8	89399	89398	1.000	275388	38
-16	90530	93926	1.038	378104	52
-16.4	92794	92935	1.002	733761	100
					53

(b) The proposed computation scheme

Figure E.1: Transfer fucntion and the proposed computation scheme

[1] z coordinate is shifted such that $z_{tip} = 0.0\,m$ (see Figure 7.18) for computation convenience

Comparison with a prediction by Nielsen

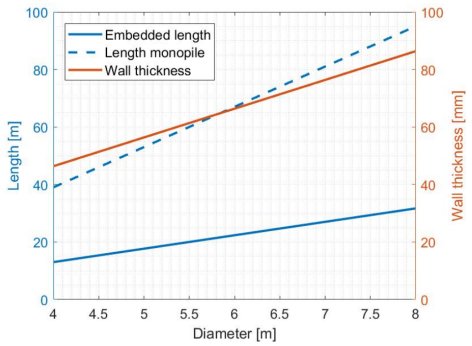

Figure F.1: Monopile dimensions (Nielsen, 2022)

Soil 1: Cohesive	Symbol	Value	Soil 2: Non-cohesive	Symbol	Value
Type of soil	-	Stiff Clay	Type of soil	-	Medium Dense Sand
Undrained shear strength	c_u	200 kPa	Dimensionless skin friction factor	β	0.37
Saturated unit weight	γ_s	21 kN/m^3	Limit unit skin friction	f_{lim}	81 kPa
			Saturated unit weight	γ_s	20 kN/m^3

Figure F.2: Soil properties (Nielsen, 2022)

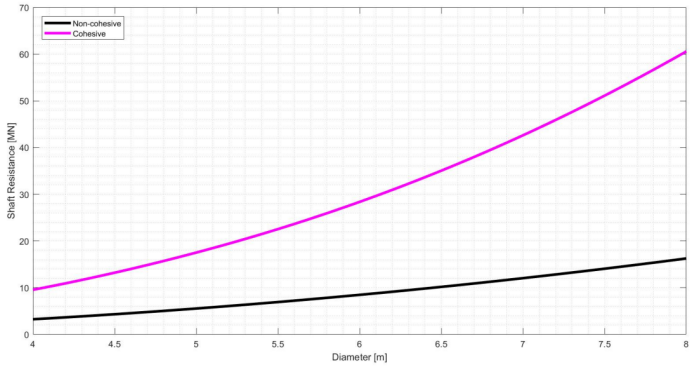

Figure F.3: Soil properties (Nielsen, 2022)

Bibliography

Achenbach, J. D. (1975). *Wave propagation in elastic solids*. Elsevier Science Publishers B.V>.

Adnan Durakovic. (2022). Nearshore Wind Farm to Be Dismantled. https://www.offshorewind.biz/2022/03/08/nearshore-wind-farm-to-be-dismantled/

Andersen, K. H. (2009). Bearing capacity under cyclic loading — offshore, along the coast, and on land. The 21st Bjerrum Lecture presented in Oslo, 23 November 2007. *Canadian Geotechnical Journal*, *46*(5), 513–535. https://doi.org/10.1139/T09-003

Anoyatis, G., & Mylonakis, G. (2011). Novel Tajimi models for static and dynamic soil-pile interaction. *Proceedings of the 8th International Conference on Structural Dynamics, EURODYN*.

Arya, S., O'Neill, M., & Pincus, G. (1979). *Design of structures and foundations for vibrating machines*. Gulf Publishing Company Book Division.

Askarinejad, A., Wang, H., Chortis, G., & Gavin, K. (2022). Influence of scour protection layers on the lateral response of monopile in dense sand. *Ocean Engineering*, *244*. https://doi.org/10.1016/j.oceaneng.2021.110377

Bond, A. J., Hight, D. W., & Jardine, R. J. (1997). *Design of piles in sand in the UK sector of the North Sea*. Copyright Unit, Her Majesty's Stationery Office.

Bonsink, W. (2018). WindDays 2018 Decommissioning Windpark Lely. https://www.topsectorenergie.nl / sites / default / files / uploads / Wind % 20op % 20Zee / Documenten / WindDays % 202018 / 20180614_Hebo_Wiebbe_Bonsink.pdf

Bowles, J. E. (1997). *Foundation analysis and design* (5th). The McGraw-Hill Companies, Inc.

Bowman, F. (1958). *Introduction to Bessel functions*. Dover Publications, Inc.

Brinkgreve, R. B. J. (2019). Behaviour of soils & rocks (CIE4361) Failure criteria of soils and rocks. *Powerpoint presentation*.

CAPE Holland. (2020). Vibro driving: the next chapter in offshore wind. https://capeholland.com/news/vibro-driving-the-next-chapter-in-offshore-wind/%20https://www.youtube.com/watch?v=5-AO60dm7rw

CAPE Holland. (2022). *Offshore vibro technology*.

CEN. (2002). EN 1991-1-1 Eurocode 1 Actions on structures Part 1-1 General actions densities self-weight imposed loads for buildings.

CEN. (2004a). *EN 1998-1 Eurocode 8: Design of structures for earthquake resistance - Part 1: General rules, seismic actions and rules for buildings*.

CEN. (2004b). *NEN-EN 10025-1 Hot rolled products of structural steels - Part 1: General technical delivery conditions*.

CEN. (2004c). NEN-EN 1993-1-1 Eurocode 3: Design of steel structures Part 1-1: General rules and rules for buildings.

CEN. (2015). NEN-EN-ISO 9001 Quality management systems - Requirements.

Choi, S., Grandhi, R., & Canfield, R. (2007). *Reliability-based Structural Design*. Springer-Verlag London Limited.

Coronel, M. (2020). *Hydraulic pile extraction scale tests for testing the removal of piles from the soil at the end of their operational life* (tech. rep.). https://www.youtube.com/watch?v=ZFQ0crZDcpI&t=27s

Deeks, A. J., & Randolph, M. F. (1994). Axisymmetric time-domain transmitting boundaries. *Journal of Engineering Mechanics*, *120*.

Denkena, B., Bergmann, B., & Holger, B. (2021). A novel tool monitoring approach for diamond wire sawing. *Production Engineering*, (0123456789), 3–10. https://doi.org/10.1007/s11740-021-01087-7

Dieseko. (2016). Decommissioning Lely offshore wind farm. https://www.youtube.com/watch?v=fJc0TD7Fg0s

DNVGL. (2016). DNVGL-ST-0126 Support structures for wind turbines.

Dong Guo, W., & Randolph, M. F. (1996). *Torsional Piles in Non-homogeneous Media* (tech. rep. No. 4).

European Comission. (2021). *Directive of the European parliament and of the council as regards the promotion of energy from renewable sources* (tech. rep.).

Fugro, DNV-GL, & RVO.nl. (2016). *Geotechnical Report / Investigation Data Seafloor In Situ Test Locations Borssele Wind Farm Site IV* (tech. rep.).

Georgiadis, M., & Saflekou, S. (1990). Piles under axial and torsional loads. *Computers and Geotechnics*.

Gómez, S. S., Tsetas, A., & Metrikine, A. V. (2022). Energy flux analysis for quantification of vibratory pile driving efficiency. *Journal of Sound and Vibration*, *541*. https://doi.org/10.1016/j.jsv.2022.117299

Gourvenec, S. (2018). Shaping the offshore decommissioning agenda and next-generation design of offshore infrastructure. *171*, 54–66.

Gourvenec, S., & Randolph, M. (2011). *Offshore geotechnical engineering*. Spon Press.

Graff, K. F. (1975). *Wave motion in elastic solids*. Oxford University Press.

Grote, K.-H., & Hefazi, H. (Eds.). (2021). *Handbook of Mechanical Engineering*. Springer International Publishing. https://doi.org/10.1007/978-3-030-47035-7

Hinzmann, N., Gattermann, J., & Lehn, P. (2020). Large-Scale Tests With Hydraulic and Pneumatic Overpressure for Monopile Decommissioning of Offshore Wind Turbines. *Volume 10: Offshore Geotechnics*. https://doi.org/10.1115/OMAE2020-18775

Hinzmann, N., Lehn, P., & Gattermann, J. (2021). Large-Scale Model Investigation for Monopile Decommissioning of Offshore Wind Turbines: Overpressure and Vibratory Pile. *International Conference on Offshore Mechanics and Arctic Engineering*. https://doi.org/10.1115/IOWTC2021-3539

Hinzmann, N., Stein, P. S., & Gatterman, J. (2018). DECOMMISSIONING OF OFFSHORE MONOPILES, OCCURING PROBLEMS AND ALTERNATIVE SOLUTIONS, 1–8.

Holeyman, A. (, Berghe, J.-F. v. (.-F., & Charue, N. ((2002). *Vibratory pile driving and deep soil compaction : TRANSVIB2002 : proceedings of the International Conference on Vibratory Pile Driving and Deep Soil Compaction, Louvain-La Neuve, Belgium, 9-10 September 2002*. A.A. Balkema Publishers.

Holthuijsen, L. H. (2007). *Waves in oceanic and coastal waters*. Cambridge University Press.

Howell, P. (2017). Elasticity and plasticity. *Lecture notes chapter 1*. https://courses-archive.maths.ox.ac.uk/node/55689/materials

Igwemezie, V., Mehmanparast, A., & Kolios, A. (2018). Materials selection for XL wind turbine support structures: A corrosion-fatigue perspective. *Marine Structures*, *61*, 381–397. https://doi.org/10.1016/j.marstruc.2018.06.008

IMO. (1989). *RESOLUTION A.672(16) adopted on 19 October 1989 GUIDELINES AND STANDARDS FOR THE REMOVAL OF OFFSHORE INSTALLATIONS AND STRUCTURES ON THE CONTINENTAL SHELF AND IN THE EXCLUSIVE ECONOMIC ZONE* (tech. rep. October).

Ishihara, K. (1996). *Soil behaviour in earthquake geotechnics*. Clarendon Press.

ISO. (2002). *ISO 11886 Building construction machinery and equipment-Pile driving and extracting equipment-Terminology and commercial specifications* (tech. rep.). www.iso.ch

Jonker, G. (1987). Vibratory pile driving hammers for pile installations and soil improvement projects. *Proceedings of the Annual Offshore Technology Conference*, *1987-April*, 549–560. https://doi.org/10.4043/5422-ms

Jr. Roger Easton. (2004). Chapter 7 propagation of waves. https://www.cis.rit.edu/class/simg303/Notes/Ch7-PropagationofWaves.pdf

Karasudhi, P., Rajapakse, R. K. N. D., & Hwang, B. Y. (1984). *TORSION OF A LONG CYLINDRICAL ELASTIC BAR PARTIALLY EMBEDDED IN A LAYERED ELASTIC HALF SPACE* (tech. rep.).

Lefebvre, G., & LeBoeuf, D. (1987). Rate effects and cyclic loading of sensitive clays. *Journal of geotechnical engineering*, *113*(5).

Lehn, P., Hinzmann, N., & Gattermann, J. (2020). New Approach for Offshore Pile Decommissioning With Hydraulic Presses and Floating Panels. *Volume 10: Offshore Geotechnics*. https://doi.org/10.1115/OMAE2020-18784

Leissa, A. W. (1973). *Vibration of shells*. U.S. Government Printing Office.

Li, X., Zhang, Z., & Sheng, J. (2021). Exact Solution for the Torsional Vibration of an Elastic Pile in a Radially Inhomogeneous Saturated Soil. *Journal of Mathematics*, *2021*. https://doi.org/10.1155/2021/6644057

Liu, Y. E. (2021). *Monopile forever*. http://resolver.tudelft.nl/uuid:5526ed6b-6a40-43b5-b96d-563c6891ae3f

Luco, J. E. (1976). *Torsion of a Rigid Cylinder Embedded in an Elastic Half Space* (tech. rep.). http://www.asme.org/about-asme/terms-of-use

Lysmer, J., & Kuhlemeyer, R. L. (1969). Finite dynamic model for infinite media. *Journal of the engineering mechanics division*.

Maio, F. D., & Rem, P. C. (2015). A Robust Indicator for Promoting Circular Economy through Recycling. (October), 1095–1104.

Male, P. v. d. (2021). *OE44135 Offshore Wind Support Structures 2020-2021 (Lecture notes)*.

Maplesoft, a. d. o. W. M. I. (2022). Maple.

Meijer, D. J. M. (2022). *Dynamic modelling of offshore monopile decommissioning. A study into the first moments of complete removal of monopiles.* http://resolver.tudelft.nl/uuid:e910be60-05bf-4dda-a926-bcb44df87c15

Mesri, G., & Hayat, T. M. (1993). *The coefficient of earth pressure at rest* (tech. rep.). www.nrcresearchpress.com

Metrikine, A. (2021). *Dynamics, Slender Structures and an Introduction to Continuum Mechanics CT 4145 (Lecture notes)*. Delft University of Technology.

Metrikine, A., Gómez, S. S., & Verichev, S. (2021). Vibratory extraction of monopiles phase 1 takeoff application.

Metrikine, A., & Tsouvalas, A. (2021). Dynamics of structures CIE4140. *Powerpoint presentation*.

Metrikine, A., & Vrouwenvelder, A. (2021). *Dynamics of Structures - CT4140 Part 2 Wave Dynamics (Lecture notes)*. Delft University of Technology.

Meulen, T. H. v. d., Bastein, T., Swamy, S. K., Saraswati, N., & Joustra, J. (2020). *Offshore wind farm decommissioning* (tech. rep.). SmartPort.

Miedema, S. A. (2014). *The Delft Sand, Clay & Rock Cutting Model* (1st). IOS Press BV.

Milne, C., Jalili, S., & Maheri, A. (2021). Decommissioning cost modelling for offshore wind farms : A bottom-up approach. *Sustainable Energy Technologies and Assessments*, *48*(February), 101628. https://doi.org/10.1016/j.seta.2021.101628

Nanda, S., Sivakumar, V., Hoyer, P., Bradshaw, A., Gavin, K., Gerkus, H., Jalilvand, S., Gilbert, R., Doherty, P., & Fanning, J. (2017). Effects of strain rates on the undrained shear strength of kaolin. *Geotechnical testing journal*. https://doi.org/https://doi.org/10.1520/GTJ20160101

Negro, V., Esteban, M. D., Alberdi, P., Imaz, M., & Serraclara, J.-m. (2017). Monopiles in offshore wind : Preliminary estimate of main dimensions. *133*(February), 253–261. https://doi.org/10.1016/j.oceaneng.2017.02.011

Nghiem, H. M., & Chang, N. Y. (2019). Efficient solution for a single pile under torsion. *Soils and Foundations*, *59*(1), 13–26. https://doi.org/10.1016/j.sandf.2018.08.015

Nielsen, B. (2022). *Feasibility study of complete removal of monopiles using vibratory pile removal*. http://resolver.tudelft.nl/uuid:a52deb33-6442-473b-9f94-ab06c8ed41a4

Novak, M., & Sachs, K. (1973). Torsional and coupled vibrations of embedded footings. *Earthquake Engineering & Structural Dynamics*, *2*(1), 11–33. https://doi.org/10.1002/eqe.4290020103

Oñate, E. (2009). *Structural analysis with finite element method. Linear statics.* (Vol. 1). International Center for Numerical Methods in Engineering (CIMNE).

Pisanò, F. (2021a). OE44030 Offshore soil behaviour: Fundamentals. *Powerpoint presentation*.

Pisanò, F. (2021b). OE44030 Offshore soil behaviour: Response to cyclic loading. *Powerpoint presentation*.

Pongiglione, M., & Calderini, C. (2014). Material savings through structural steel reuse: A case study in Genoa. *Resources, Conservation and Recycling*, *86*, 87–92. https://doi.org/10.1016/j.resconrec.2014.02.011

Poulos, H. G., & Davis, E. H. (1980). *Pile foundation analysis and design* (W. T. Lambe, Ed.). Rainbow-Bridge Book Co.

Poulos, H. (1975). Torsional response of piles. *Journal of the Geotechnical Engineering Division*.

Reissner, E., & Sagoci, H. F. (1944). Forced torsional oscillations of an elastic half-space. I. *Journal of Applied Physics*, *15*(9), 652–654. https://doi.org/10.1063/1.1707489

Sathialingam, N., & Kutter, B. L. (1989). The effects of high strain rate and high frequency loading on soil behavior in centrifuge model tests.

Schachner, J. (2004). *Power connections for offshore wind farms*.

Schreier, S. (2021). Floating structures & offshore moorings. *Lecture notes OE44100*.

Segeren, M. (2019). *Gentle Driving of Piles* (tech. rep.). GROW. https://grow-offshorewind.nl/files/downloads/gdp-grow-side-event-winddays-2019-gentle-driving-of-piles.pdf

Shafiee, M., & Adedipe, T. (2022). Offshore wind decommissioning : an assessment of the risk of operations. *International Journal of Sustainable Energy*, 1–27. https://doi.org/10.1080/14786451.2021.2024830

Sharma, N., Dasgupta, K., & Dey, A. (2020). Optimum lateral extent of soil domain for dynamic SSI analysis of RC framed buildings on pile foundations. *Frontiers of Structural and Civil Engineering*, *14*(1), 62–81. https://doi.org/10.1007/s11709-019-0570-2

Shirzadeh, R., Devriendt, C., Bidakhvidi, M., & Guillaume, P. (2013). Experimental and computational damping estimation of an offshore wind turbine on a monopile foundation. *Journal of Wind Engineering and Industrial Aerodynamics*.

Soedel, W. (2004). *Vibrations of shells and plates* (Third edition). Marcel Dekker, Inc.

Stapel, W. (2021). *Entire monopile foundation removal "A method to pull out entire monopile foundations"*. http://resolver.tudelft.nl/uuid:7ebff086-83a5-4c53-b0cc-93dae9dacf46

Terzaghi, K. (1943). *Theoretical Soil Mechanics*. John Wiley & Sons, Inc.

Timoshenko, S., & Goodier, J. N. (1951). *Theory of elasticity*. McGraw-Hill Book Company, Inc.

Timoshenko, S., & Woinowsky-Krieger, S. (1959). *Theory of plates and shells* (Second edition). McGraw-Hill Book Company, Inc.

Topham, E., Mcmillan, D., Bradley, S., & Hart, E. (2019). Recycling offshore wind farms at decommissioning stage. *Energy Policy*, *129*(March), 698–709. https://doi.org/10.1016/j.enpol.2019.01.072

Topham, E., Mcmillan, D., Topham, E., & Mcmillan, D. (2016). Sustainable Decommissioning of an Offshore Wind Farm Sustainable decommissioning of an offshore wind farm. *Renewable Energy*, *102*(December 2017), 470–480. https://doi.org/10.1016/j.renene.2016.10.066

Tsetas, A., Gomez, S. S., Tsouvalas, A., & Beek, K. V. (2020). Experimental identification of the dynamic behaviour of pile-soil system installed by means of three different pile-driving techniques. (December). https://doi.org/10.47964/1120.9245.20367

Tsetas, A., Metrikine, A., Tsouvalas, A., & Metrikine, A. V. (2022). *An alternating frequency-time harmonic balance method for fast-slow dynamical systems* (tech. rep.). https://www.researchgate.net/publication/364041505

Tsetas, A., Tsouvalas, A., Gómez, S. S., Pisanò, F., Kementzetzidis, E., Molenkamp, T., Elkadi, A. S., & Metrikine, A. V. (2023). Gentle Driving of Piles (GDP) at a sandy site combining axial and torsional vibrations: Part I - installation tests. *Ocean Engineering*, *270*. https://doi.org/10.1016/j.oceaneng.2022.113453

Tsetas, A., Tsouvalas, A., & Metrikine, A. V. (2021). Installation of Large-Diameter Monopiles: Introducing Wave Dispersion and Non-Local Soil Reaction. *Journal of Marine Science and Engineering*, *9*(3), 313. https://doi.org/10.3390/jmse9030313

Tsouvalas, A. (2015). *Underwater noise generated by offshore pile driving* (Doctoral dissertation november).

Vacareanu, V., Kementzetzidis, E., & Pisanò, F. (2019). 3D FE seismic analysis of a monopile-supported offshore wind turbine in a non-liquefiable soil deposit. *2nd International Conference on Natural Hazards & Infrastructure*.

Veletsos, A. S., & Dotson, K. W. (1987). *VERTICAL AND TORSIONAL VIBRATION OF FOUNDATIONS IN INHOMOGENEOUS MEDIA* (tech. rep.).

Vugts, J. H. (2013). *Handbook of Bottom Founded Offshore Structures Part 1. General features of offshore structures and theoretical background*. Eburon Academic Publishers.

Vugts, J. H. (2016). *Handbook of Bottom Founded Offshore Structures Part 2. Fixed steel structures*. Eburon.

Wang, G., Ge, W., Pan, X., & Wang, Z. (2008). Torsional vibrations of single piles embedded in saturated medium. *Computers and Geotechnics*, *35*(1), 11–21. https://doi.org/10.1016/j.compgeo.2007.02.001

Warrington, D. C. (1989). Theory and development of vibratory pile-driving equipment. *Proceedings of the Annual Offshore Technology Conference*, *1989-May*, 541–550. https://doi.org/10.4043/6030-ms

Wei, J., Wang, W., & Wu, J. (2022). Numerical investigation of inside peak particle velocities for predicting the vibration influence radius of vibratory pile driving. *Soil Dynamics and Earthquake Engineering*, *153*. https://doi.org/10.1016/j.soildyn.2021.107103

Wellens, P. (2021). CFD MT44020 Motions and loading of structures in waves Part 2. *Powerpoint presentation*.

Wierzbicki, T. (2022). Structural mechanics. *LibreTexts*.

Wind & water works. (2022). *Dutch Offshore Wind Guide Your guide to Dutch offshore wind policy, technologies and innovations* (tech. rep.). Wind & water works.

Wolf, J. P. (1985). *Dynamic soil-structure interaction* (W. J. Hall, Ed.). Prentice-Hall, Inc.

Wolfram Alpha. (2022a). HankelH2[1,x]. https://www.wolframalpha.com/input?i=HankelH2%5B1%2Cx%5D

WolframAlpha. (2022b). HankelH1[1,x]. https://www.wolframalpha.com/input?i=HankelH1%5B1%2Cx%5D

Wu, W., Liu, H., El Naggar, M. H., Mei, G., & Jiang, G. (2016). Torsional dynamic response of a pile embedded in layered soil based on the fictitious soil pile model. *Computers and Geotechnics*, *80*, 190–198. https://doi.org/10.1016/j.compgeo.2016.06.013